

POLITECNICO
MILANO 1863

School of Industrial and Information Engineering, Department of Chemistry, Materials and Chemical Engineering "G. Natta"

Master of Science in Materials Engineering and Nanotechnology

---

PEO treatments on CP titanium in 0.5 M sulphuric acid using hybrid duty cycles

Supervisor: Marco Ormellese
Co-Supervisor: Luca Casanova

Matteo Bisogni
ID 917876

Academic Year 2019-2020

Abstract

Thanks to its exceptional mechanical characteristics and its corrosion resistance in aggressive environments, titanium is one of the most used and studied metals. Its properties make it suitable for use in the industrial, aerospace, health, food, and chemical fields.

In chapter 1 its characteristics and the characteristics of its oxide, which guarantees its high resistance to corrosion, have been reported. The main forms of corrosion, to which titanium is subjected, are also reported.

In chapter 2 the surface treatments, which are mostly used for this metal to improve its properties (especially corrosion resistance), are exposed. The most thorough treatment, and object of study in this thesis, is anodizing. For this reason, all the ways in which the treatment is carried out, and the action of the various parameters (current, voltage, frequency, electrolyte etc ...) influencing the growth of the oxide, have been reported.

In chapter 3 the various oxide characterization tests, subsequently used in this study, have been reported.

The samples tested in this research underwent pulsed anodizing with a final potential of 160 V. Each anodization was carried out with two different frequency values: 20 Hz and 1000 Hz. During each anodization the voltage and current were measured. Subsequently, the anodized samples were subjected to an immersion test, from which the corrosion rate could be obtained. The specimens that demonstrated high resistance to corrosion were subjected to a cathodic potentiodynamic test to analyze their behavior at negative potentials, to an X-ray analysis (XRD) to study their structure, and to the electron microscope analysis (SEM) to study their morphology. From the images obtained, through ImageJ, it was possible to analyze the size of the pores and the density of surface porosity: useful characteristics to understand the action of the duty cycle on the growth and morphology of the oxide. Finally, electrochemical impedance spectroscopy (EIS) tests were performed on chosen specimens to understand the structure of their oxide and their thickness trend in acidic solution.

From the results obtained, duty cycles, that allow to obtain a good quality oxide with excellent resistance to corrosion in sulphuric acid environment, have been discovered. Future studies, aimed at understanding in depth the effect of each electrochemical parameter on the oxide, will be necessary to improve this process and the quality of the coating formed.

Sommario

Grazie alle sue eccezionali caratteristiche meccaniche e alla sua resistenza a corrosione in ambienti aggressivi, il titanio è uno dei metalli più usati e studiati. Le sue proprietà lo rendono idoneo all'utilizzo in campo industriale, aerospaziale, sanitario, alimentare, e chimico.

Nel capitolo 1 sono state riportate le sue caratteristiche e le caratteristiche del suo ossido, che garantisce la sua alta resistenza a corrosione. Vengono riportate anche le principali forme di corrosione a cui è soggetto.

Nel capitolo 2 vengono esposti i trattamenti superficiali, che sono maggiormente utilizzati per questo metallo, per migliorare le sue proprietà, specialmente quella di resistenza a corrosione. Il trattemento più approfondito, e oggetto di studio in questa tesi, è l'anodizzazione. Per questo, sono state riportate tutte le modalità con cui viene effettuato il trattamento, e l'influenza dei vari parametri (corrente, voltaggio, frequenza, elettrolita etc...) sulla crescita dell'ossido.

Nel capitolo 3 sono stati riportati i vari test di caratterizzazione dell'ossido, successivamente utilizzati in questo studio.

I campioni testati in questa ricerca hanno subito un'anodizzazione pulsata con un potenziale finale di 160 V. Ogni anodizzazione è stata eseguita con due valori differenti di frequenza, 20 Hz e 1000 Hz. Durante ogni anodizzazione sono stati misurati il voltaggio e la corrente. Successivamente i campioni anodizzati sono stati sottoposti ad un test ad immersione, dal quale si è potuta ottenere la velocità di corrosione. I provini che hanno dimostrato un'alta resistenza alla corrosione sono stati sottoposti a un test potenziodinamico catodico per analizzare il loro comportamento a potenziali negativi, ad un'analisi ai raggi X (XRD) per studiare le fasi presenti. La morfologia, invece, è stata investigata tramite microscopio elettronico a scansione (SEM). Dalle immagini ottenute, tramite ImageJ, è stato possibile analizzare la dimensione dei pori e la densità di porosità superficiale: caratteristiche utili a comprendere l'azione del duty cicle sulla crescita e sulla morfologia dell'ossido. Infine, test di spettroscopia di impedenza elettrochimica (EIS) sono stati eseguiti su provini scelti per comprendere la struttura del loro ossido e l'andamento del suo spessore in soluzione acida.

Dai risultati ottenuti sono stati scoperti duty cycle che permettono di ottenere un ossido di buona qualità con un'ottima resistenza alla corrosione in ambiente acido contenente solfuri. Studi futuri, volti a comprendere in profondità l'effetto di ogni parametro elettrochimico sull'ossido, saranno necessari per migliorare questo

processo e la qualità del coating formato.

Contents

1 Titanium **1**
- 1.1 History . . . 1
- 1.2 Chemical and Physical Characteristics . . . 1
- 1.3 Common Grades . . . 2
  - 1.3.1 Grade 1 . . . 2
  - 1.3.2 Grade 2 . . . 2
  - 1.3.3 Grade 3 . . . 3
  - 1.3.4 Grade 4 . . . 3
  - 1.3.5 Grade 5 Ti-6Al-4V . . . 3
  - 1.3.6 Grade 7 . . . 3
  - 1.3.7 Grade 12 . . . 4
  - 1.3.8 Grade 23 . . . 4
- 1.4 Corrosion . . . 4
  - 1.4.1 Uniform Corrosion . . . 5
  - 1.4.2 Pitting corrosion . . . 12
  - 1.4.3 Crevice corrosion . . . 15
  - 1.4.4 Stress corrosion cracking . . . 16
  - 1.4.5 Hydrogen-induced cracking . . . 18

2 Treatments to improve corrosion resistance **20**
- 2.1 Alloying with noble metals . . . 20
- 2.2 Thermal oxidation . . . 22
- 2.3 Anodizing . . . 24
  - 2.3.1 Process setup . . . 24
  - 2.3.2 Oxide growth . . . 26
  - 2.3.3 Process parameters . . . 27
  - 2.3.4 Standard Anodization . . . 32
  - 2.3.5 Plasma Electrolytic Oxidation . . . 34
  - 2.3.6 Nanotubes production . . . 39

3 Coating Analysis **43**
- 3.1 Immersion test . . . 43
- 3.2 Potentiodynamic scan . . . 44
  - 3.2.1 Anodic scan . . . 44
  - 3.2.2 Cathodic scan . . . 45
- 3.3 EIS . . . 46
  - 3.3.1 Graphical Representation of Impedance Spectroscopy Data . . . 49
  - 3.3.2 Circuit Elements . . . 51

3.3.3 Circuit for titanium oxide . . . 52
3.4 SEM . . . 55
3.5 XRD . . . 55

4 Experimental **56**
4.1 Samples preparation . . . 56
4.2 Anodizing . . . 56
4.2.1 Anodizing machine . . . 56
4.2.2 Solution and Set-up . . . 58
4.2.3 Duty cycle . . . 59
4.3 Immersion test . . . 60
4.4 Potenziodynamic test . . . 60
4.5 EIS . . . 60
4.6 SEM and XRD . . . 61
4.7 Analysis of porosity . . . 61

5 Results & Discussion **62**
5.1 Duty selection . . . 62
5.1.1 55A-40C-5R-5%-20 Hz . . . 63
5.1.2 55A-40C-5R-5%-1000 Hz . . . 65
5.1.3 45A-50C-5R-2%-1000 Hz . . . 68
5.1.4 45A-50C-5R-5%-1000 Hz . . . 71
5.2 Immersion test . . . 74
5.3 Cathodic Polarization . . . 75
5.4 Anodic Polarization . . . 77
5.5 SEM and XRD . . . 80
5.5.1 55A-40C-5R-5%-20 Hz . . . 81
5.5.2 55A-40C-5R-5%-1000 Hz . . . 82
5.5.3 45A-50C-5R-2%-1000 Hz . . . 83
5.5.4 45A-50C-5R-5%-1000 Hz . . . 84
5.5.5 45A-50C-5R-10%-20 Hz . . . 85
5.6 Porosity . . . 86
5.7 EIS . . . 88

6 Conclusion **96**

List of Figures

1.1 Phase diagram of titanium alloys 1
1.2 Crystal structures of a) rutile, b) anatase and c) brookite. 4
1.3 Uniform corrosion 5
1.4 Pourbaix Diagram of Titanium 6
1.5 Prosthetic and orthodontic implants of titanium 7
1.6 Corrosion of titanium as a function of pH and fluoride ion concentration 8
1.7 Open circuit recordings at 0.28 cm^2 titanium electrodes immersed in 0.9 wt % NaCl with 0.2 g/L $NaHCO_3$ and different pH and fluoride concentration. 20–22 h of exposure. Classification: P, passive; NP, non-passive; A, active. 9
1.8 Dependence of i_{corr} on HBr molar concentration 10
1.9 Typical forms of pitting attack 13
1.10 Effects of temperature, $[Cl^-]$, pH on active-passive metals 13
1.11 Schematic representation of (a) penetration, (b) adsorption and thinning, and (c) film breaking 14
1.12 Schematic depiction of crevice corrosion and the chemical processes involved. 15
1.13 Simplified representation of SCC mechanisms: a) slip dissolution; b) hydrogen embrittlement (HE). 17
1.14 Depict of the appearance of cracking propagation in SCC: **a** intergranular; **b** transgranular; **c** delta river transgranular 17
1.15 Schematic of the influence of halide ion concentration and metallurgical factors. 18
1.16 SEM micrographs of Ti-6Al-4V alloys after electrochemical hydrogenation revealing HIC in: (**a**) the fully lamellar microstructure, between the α and β lamellas; (**b**) duplex microstructure, in the boundaries and inside the equiaxied grains of primary α. 19

2.1 Anodic protection effect by cathodic alloying with Pd (or Pt) [7]. . . 21
2.2 SEM images of surface morphology of samples thermally oxidized at 650°C for various time periods; (a) 8, (b) 16, (c) 24 and (d) 48 h. . . 23
2.3 Potentiodynamic polarization curves of untreated and thermally oxidized samples. 24
2.4 Anodizing of titanium in an electrochemical cell. *Left*: cathode surrounding the whole titanium specimen, *center*: frontal cathode, *right*: hand painting with electrochemical brush 25
2.5 SEM image of sample anodized in 0.5 M H_2SO_4 with current density 1080 A/m^2 and cell potential 140 V: oxide surface [45]. 27

2.6 relation between oxide thickness and anodic forming voltage of pure titanium in 1.0 M sulphuric acid solution. Lost of linearity between 70-90 V[48]. 28
2.7 Change in film thickness during anodizing 29
2.8 Anodic current density versus anodic voltage during porous electrochemical oxidation of titanium foils in 0.1 M NH_4F solution in ethyleneglycol at different temperatures of the electrolyte. 30
2.9 SEM images and their schematic view of the etching process during anodization resulting in spaghetti like structure formation. The steps of schematic representation correspond to the porous titania formed at -5 °C (a), 0 °C (b), 20 °C (c,d). Anodic voltages: 100V (a), 90 V (b), 60 V(c,d); current density 10mA/cm^2, anodization time 35 min (a,b,c) and 660 min (d). 31
2.10 The cell diameter and porosity of the titania formed at the anodic current density of 10 mA/cm^2 for 30 min a a function of the electrolyte temperature. The cell diameters depend mainly on the anodic voltage. 31
2.11 SEM bottom views (A-D), top-views (E-H), and cross-sectional views (I-L) of ATO layers formed at 30 V for 10 min at different stirring speeds ranging from 0 to 500 rpm. 32
2.12 oxide interference 33
2.13 Schematic depiction of the sequence events during a single discharge, showing: (a) initial electrical breakdown, (b) development of the plasma channel through the coating thickness, (c) initial bubble growth and formation of oxide in the plasma, (d) bubble expansion and heating of region around discharge, (e) shrinkage and cooling as the plasma resistance rises, causing the current to fall, and (f) final quenching and expulsion of some liquefied oxide from the channel [64]. . . . 35
2.14 Surface structures of the oxide films of CP samples via PEO coating in two different electrolytes [66]. 36
2.15 Overview of anodizing signals[67]. 37
2.16 Bipolar pulse anodizing[67]. 37
2.17 Variation with frequencies of: coating thickness (left) and relative contents of anatase and rutile TiO_2 (right) of CP Ti specimens after PEO treatment [72]. 38
2.18 Variation with frequencies of: coating thickness (left) and coating microstructure (right) of CP Ti specimens after PEO treatment [76]. 39
2.19 Evolution of the self-organization (and length) of anodized TiO_2 NTs: (a) 1st generation [78], (b) 2nd generation [79], (c) 3rd generation [80], (d) 4th generation [81]. 40
2.20 Current-time transient registered for a sample anodized in: (a) a NaF/H_2O electrolyte at 20 V [82] and (b) during the anodization of titanium at different potentials in glycerol/NaF [83]. 41

3.1 Immersion test 43
3.2 Theoretical anodic polarization scan 45
3.3 Theoretical cathodic polarization scan 46
3.4 Impedance experiment: sinusoidal voltage input V at a single frequency f and current response I 47

3.5 Impedance data representation: A. Lissajous figure; B. Complex impedance plot . . . 48
3.6 A. Equivalent circuit; B. Nyquist; C. Bode plots with impedance for the R—C circuit. . . . 49
3.7 Equivalent circuit used in EIS results interpretation[90]. . . . 52
3.8 Schematical models for the oxides grown in the different electrolytes. M=metal, Li=oxide layer, Px=phosphorous containing species[93]. . . . 53
3.9 Equivalent circuit used to fit EIS experimental data for (a) non-anodised titanium and (b) anodised titanium [91]. . . . 53
3.10 Equivalent circuits: a) traditionally used for the fitting of EIS results for porous materials, b) new concept for the fitting of EIS spectra for the anodically treated groups. . . . 54
3.11 Nyquist diagram with Warburg element. . . . 54

4.1 Asterion AST 751 . . . 57
4.2 Steady state panel . . . 57
4.3 Electrochemical cell for anodization. . . . 58
4.4 Oscilloscope Tektronix TBS 1072B-EDU . . . 59
4.5 Example of duty cycle 45A-50C-5R-10%. Abrupt duty cycle (BLUE) and duty cycle with ramp (ORANGE) . . . 59
4.6 Multi Autolab/M204 - Twelve Channel Multi Potentiostat/Galvanostat 61
4.7 EIS cell . . . 61

5.1 Voltage trend during anodization . . . 63
5.2 Voltage and Current at 1 minute . . . 64
5.3 Voltage and Current at 2 minutes . . . 64
5.4 Voltage and Current at 3 minutes . . . 64
5.5 Voltage and Current at 4 minutes . . . 65
5.6 Voltage and Current at 5 minutes . . . 65
5.7 Voltage during anodization . . . 66
5.8 Sample before (A) and after (B) the soft spark. . . . 66
5.9 Voltage and Current at 1 minute . . . 67
5.10 Voltage and Current at 2 minutes . . . 67
5.11 Voltage and Current at 3 minutes . . . 67
5.12 Voltage and Current at 4 minutes . . . 68
5.13 Voltage and Current at 5 minutes . . . 68
5.14 Voltage trend during anodization . . . 68
5.15 Voltage and Current at 1 minute . . . 69
5.16 Voltage and Current at 2 minutes . . . 69
5.17 Voltage and Current at 3 minutes . . . 70
5.18 Voltage and Current at 4 minutes . . . 70
5.19 Voltage and Current at 5 minutes . . . 70
5.20 Voltage trend during anodization . . . 71
5.21 Sample before (A) and after (B) the soft spark. . . . 71
5.22 Voltage and Current at 1 minute . . . 72
5.23 Voltage and Current at 2 minutes . . . 72
5.24 Voltage and Current at 3 minutes . . . 72
5.25 Voltage and Current at 4 minutes . . . 73
5.26 Voltage and Current at 5 minutes . . . 73

5.27 Corrosion rate of samples in H_2SO_4 3% in volume at 60°C 74
5.28 Corrosion rate of 55A-40C-5R samples in H_2SO_4 10% in volume . . . 75
5.29 Corrosion rate of 45A-50C-5R samples in H_2SO_4 10% in volume . . . 75
5.30 Cathodic polarization curves 76
5.31 Anodic polarization of sample 55A-40C-5R-5%-1000 Hz. 77
5.32 Nyquist diagram of the sample 55A-40C-5R-5%-1000 Hz during anodic polarization test. 78
5.33 Bode Modulus of the sample 55A-40C-5R-5%-1000 Hz during anodic polarization test. 78
5.34 Bode Phase of the sample 55A-40C-5R-5%-1000 Hz during anodic polarization test. 79
5.35 SEM image at 5000X 81
5.36 SEM image at 25000 X 81
5.37 XRD 81
5.38 SEM image at 5000X 82
5.39 SEM image at 25000 X 82
5.40 XRD 82
5.41 SEM image at 5000X 83
5.42 SEM image at 25000 X 83
5.43 XRD 83
5.44 SEM image at 5000X 84
5.45 SEM image at 25000X 84
5.46 XRD 84
5.47 SEM image at 5000X 85
5.48 SEM image at 25000X 85
5.49 XRD 85
5.50 Average dimension of pores 86
5.51 Density of pores 87
5.52 ImageJ analysis of sample 55A-40C-5R-5%-20 Hz 87
5.53 ImageJ analysis of sample 55A-40C-5R-5%-1000 Hz 87
5.54 ImageJ analysis of sample 45A-50C-5R-2%-1000 Hz 88
5.55 ImageJ analysis of sample 45A-50C-5R-5%-1000 Hz 88
5.56 Circuit used for the titanium grade 2 non-anodized 89
5.57 OCP trend of titanium grade 2 non-anodized. 89
5.58 Nyquist diagram of titanium grade 2 non-anodized. 89
5.59 Bode Modulus of titanium grade 2 non-anodized. 90
5.60 Bode Phase of titanium grade 2 non-anodized. 90
5.61 Resistance of the barrier layer of titanium grade 2 non-anodized . . . 91
5.62 Capacitance of the barrier layer of titanium grade 2 non-anodized . . 91
5.63 Circuit used for the sample 55A-40C-5R-5%-1000 HZ. 92
5.64 OCP trend of the sample 55A-40C-5R-5%-1000 HZ. 92
5.65 Nyquist diagram of the sample 55A-40C-5R-5%-1000 HZ. 92
5.66 Bode Modulus of the sample 55A-40C-5R-5%-1000 HZ. 93
5.67 Bode Phase of the sample 55A-40C-5R-5%-1000 HZ. 93
5.68 Resistance of the barrier layer of the sample 55A-40C-5R-5%-1000 HZ. 94
5.69 Resistance of the porous layer of the sample 55A-40C-5R-5%-1000 HZ. 94
5.70 Capacitance of the barrier layer of the sample 55A-40C-5R-5%-1000 HZ. 95

5.71 Capacitance of the porous layer of the sample 55A-40C-5R-5%-1000 HZ. 95

List of Tables

1.1 Chemical specifications of titanium grade 2 2
1.2 Mechanical properties of titanium grade 2 3
1.3 Classification of Corrosion Status of Titanium Based on the Open Circuit Potential (OCP), after 20 hours. 8
1.4 Corrosion rate (mm/year) of titanium in HCl aerated solution 9
1.5 Electrochemical corrosion parameters of Ti as a function of HBr concentration at 298 K 10
1.6 Corrosion rate (mm/year) of titanium in HNO_3 aerated solution [21]. 11
1.7 Corrosion rate (mm/year) of CP titanium in H_2SO_4 aerated solution [21]. 11
1.8 Corrosion rate (mm/year) of CP titanium in H_3PO_4 aerated solution [21]. 12

2.1 Microhardness and thickness variation as a function of thermal oxidation time 23

3.1 Ideal Circuit Elements Used in the Models 52

4.1 Chemical composition and mechanical properties of samples 56

5.1 Corrosion rates of the specimens that had kept the oxide layer after the test 74
5.2 Values of OCP (V), Oxygen limiting current (A/m^2), H limiting current (A/m^2). 76
5.3 Values of Y0 and N of the $CPE_{barrierlayer}$ 90
5.4 Values of Y0 and N of the $CPE_{barrierlayer}$ and $CPE_{porouslayer}$ 93

Chapter 1

Titanium

1.1 History

Titanium is the fourth most abundant metal on Earth and it was discovered in 1791 by the Reverend William Gregor and it was named "Manaccanite". A few years later, the German chemist Heinrich Klaporth rediscovered it in form of its rutile oxide, renaming it "Titanium" after the Titans (from Greek mythology). Then, it took more than 100 years to isolate the metal. The first alloys, including the most popular Ti-6Al-4V, were developed in the late 1940s in the United States [1].

1.2 Chemical and Physical Characteristics

The Titanium is a silver-gray metal of Group 4 of the periodic table. It is a lightweight, high-strength, low corrosion structural metal with a melting point of 1650°C.
Titanium can be alloyed with Iron, Aluminium, Vanadium, and Molybdenum, Palladium among other elements in order to increase mechanical properties and corrosion resistance [2].
There are 3 structural types of titanium alloys: Alpha, Alpha-Beta, and Beta (figure 1.1).

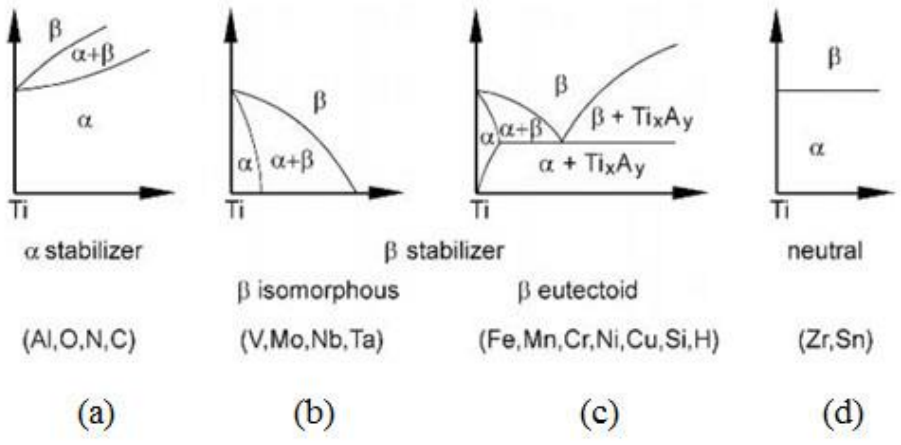

Figure 1.1: Phase diagram of titanium alloys

Alpha titanium alloys are commercially pure and non-heat treatable but they are generally very weldable. They have: low to medium strength, good notch toughness, good ductility, excellent mechanical properties at cryogenic temperatures.
Pure titanium and alpha alloys possess the highest corrosion resistance.
Alpha-Beta titanium alloys are heat treatable and weldable. Typical properties include: strength levels are medium to high, high temperature creep strength is not good as most alpha alloys, cold forming may be limited but hot forming qualities are normally good and many alloys can be superplastically formed. The most common used alpha-beta alloy is Ti-6Al-4V.
Beta titanium alloys are: fully heat treatable, generally weldable, capable of high strengths, possess good creep resistance up to intermediate temperatures, and have excellent formability.

1.3 Common Grades

1.3.1 Grade 1

Grade 1 titanium is the first of four commercially pure titanium grades. It is the softest and most ductile of these grades. It possesses the greatest formability, excellent corrosion resistance and high impact toughness.
Because of all these qualities, Grade 1 is the material of choice for any application where formability is required and is commonly available as titanium plate and tubing.

1.3.2 Grade 2

Grade 2 titanium is called the "workhorse" of the commercially pure titanium industry, thanks to its varied usability and wide availability. It shares many of the same qualities as Grade 1 titanium, but it is slightly stronger. Both are equally corrosion resistant.
This grade possesses good weldability, strength, ductility, and formability.
Chemical specifications and mechanical properties are shown in tables 1.1, 1.2.

Table 1.1: Chemical specifications of titanium grade 2

Elements	**Content**
Carbon, C	$< 0,08\%$
Iron, Fe	$< 0,3\%$
Oxygen, O	$< 0,25\%$
Hydrogen, H	$< 0,015\%$
Nitrogen, N	$< 0,03\%$
Titanium, Ti	Balance

Table 1.2: Mechanical properties of titanium grade 2

Mechanical property	**Value**
Yield Strenght	275 Mpa
Ultimate Tensile Strenght	345 Mpa
Elongation	$> 20\%$
Reduction of area	$> 30\%$

1.3.3 Grade 3

This grade is the least used of the commercially pure titanium grades, but that does not make it any less valuable. Grade 3 is stronger than Grades 1 and 2, similar in ductility and only slightly less formable, but it possesses higher mechanicals than its predecessors.
Grade 3 is used in applications requiring moderate strength and major corrosion resistance.

1.3.4 Grade 4

Grade 4 is known as the strongest of the four grades of commercially pure Titanium. It is also known for its excellent corrosion resistance, good formability, and weldability.
Though it is normally used in industrial applications, Grade 4 has recently found a niche as medical grade titanium. It is needed in applications in which high strength is required.

1.3.5 Grade 5 Ti-6Al-4V

Known as the "workhorse" of the titanium alloys, Ti 6Al-4V, or Grade 5 titanium, is the most commonly used of all titanium alloys. It accounts for 50 percent of total titanium usage the world over.
Its usability lies in its many benefits. Ti 6Al-4V may be heat-treated to increase its strength. It can be used in welded construction at service temperatures of up to 315°C. This alloy offers its high strength at lightweight, useful formability, and high corrosion resistance.
Ti-6Al-4V's usability makes it the best alloy for use in several industries, like the aerospace, medical, marine, and chemical processing industries.

1.3.6 Grade 7

Grade 7 is mechanically and physically equivalent to Grade 2, except with the addition of the interstitial element palladium, making it an alloy. Grade 7 possesses excellent weldability and fabricability and is the most corrosion resistance of all titanium alloys. It is most resistant to corrosion in reducing acids.
Grade 7 is used in chemical processes and production equipment components.

1.3.7 Grade 12

Grade 12 titanium holds an "excellent" rating for its high-quality weldability. It is a highly durable alloy that provides a lot of strength at high temperatures. Grade 12 titanium possesses characteristics similar to 300 series stainless steel.
This alloy can be hot or cold formed using press brake forming, hydro-press forming, stretch forming, or drop hammer method. Its ability to be formed in a variety of ways makes it useful in many applications. This alloy's high corrosion resistance also makes it invaluable to those manufacturing types of equipment where crevice corrosion is a concern.

1.3.8 Grade 23

Ti-6Al-4V ELI, or Grade 23, is the higher purity version of Ti-6Al-4V. It can be made into coils, strands, wires, or flat wires. It's the top choice for any sort of situation where a combination of high strength, light-weight, good corrosion resistance, and high toughness are required. It has a superior damage tolerance to other alloys.
These benefits make Grade 23 the ultimate dental and medical titanium grade. It can be used in biomedical applications such as implantable components due to its biocompatibility, good fatigue strength, and low modulus.

1.4 Corrosion

Titanium has high corrosion resistance due to the formation, on its surface, of its oxide (TiO_2) immediately after the exposure to air.
The titanium oxide layer is very adherent to the substrate, chemically stable, and when it is damaged it reforms quickly, guaranteeing protection to the underlying material. The common oxide structures in nature are anatase, rutile, and brookite (figure 1.2) [3].

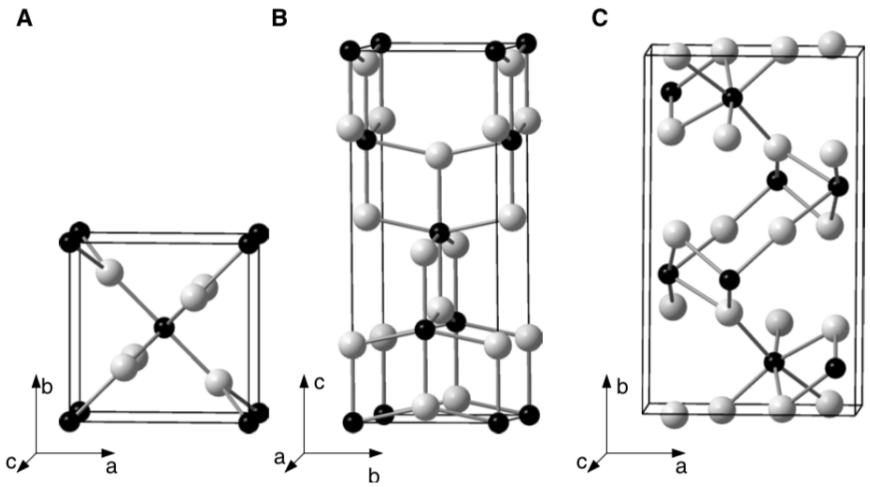

Figure 1.2: Crystal structures of a) rutile, b) anatase and c) brookite.

The rutile is the most common in nature and it has a tetragonal cell in which the titanium cations have a coordination number of 6, meaning they are surrounded by

an octahedron of 6 oxygen atoms. The oxygen anions have a coordination number of 3, resulting in trigonal planar coordination. Rutile also shows a screw axis when its octahedra are viewed sequentially [4][5].
Two growth habits of anatase crystals may be distinguished. The most common occurs as simple acute double pyramids with an indigo-blue to a black color and steely luster. Crystals of the second type have numerous pyramidal faces developed, and they are usually flatter or sometimes prismatic inhabit; the color is honey-yellow to brown.
The brookite structure is built up of distorted octahedra with a titanium ion at the center and oxygen ions at each of the six vertices. Each octahedron shares three edges with adjoining octahedra, forming an orthorhombic structure [6].
In an aggressive environment, however, TiO_2 grown by air exposure is not enough for protection and so titanium is alloyed with other elements, which promote cathodic reactions to help the system reaching a passive condition, or surface treatment is performed in order to create a more stable oxide.

1.4.1 Uniform Corrosion

This is a form of corrosion that affects the whole surface of the metallic material in contact with the corrosive environment.
If the attack is spread evenly, it is referred to as *uniform corrosion*, otherwise, corrosion is *unevenly generalized*.
Material thinning (figure 1.3), called also thickness loss, is generated at a typically predictable rate provided that the environmental conditions are known [7].

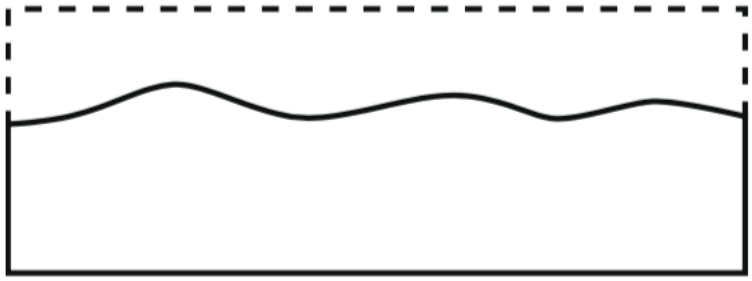

Figure 1.3: Uniform corrosion

The main cause of general corrosion problem in real plants is linked with the wrong choice of the material during the design phase. In fact, general corrosion can be often tolerated because the effect of metal loss is relatively easy to assess, and allowances can be made in the initial design [8]. A useful way to examine titanium corrosion is to use the Pourbaix diagram (potential/pH diagram) which provides information about the stability of a metal as a function of pH and potential (figure 1.4).

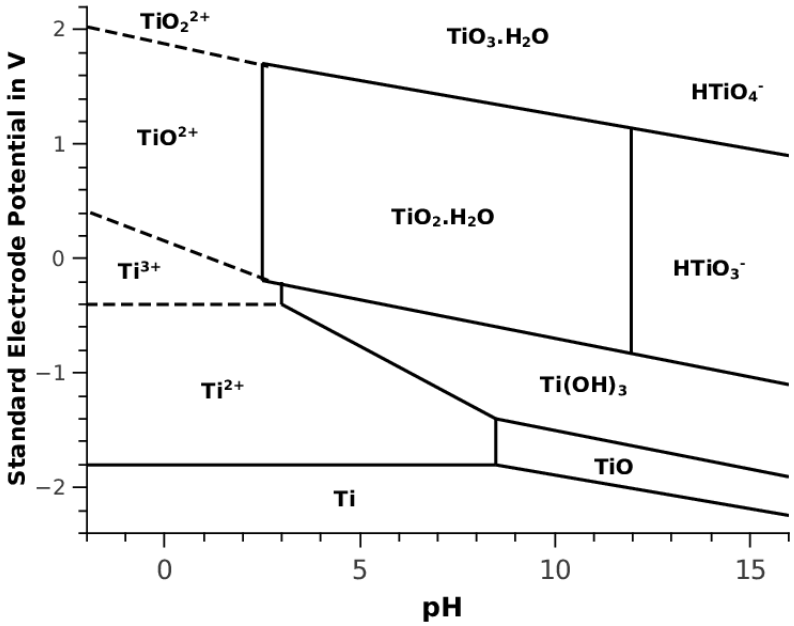

Figure 1.4: Pourbaix Diagram of Titanium

Corrosion is limited to low values of pH at low potentials where strongly anodic oxidizing conditions cause the oxide to dissolve, and at high potentials where the strongly cathodic reducing conditions promote the formation of hydrides.
Uniform corrosion occurs in reducing environments, particularly in acidic conditions at high temperature. In strong hot reducing acids, the oxide film is dissolved, and the bare metal is oxidized to soluble trivalent ions ($Ti \rightarrow Ti^{3+} + 3e^-$). In the presence of dissolved oxygen in the hot acid, the Ti^{3+} ions are oxidized to Ti^{4+} ions, and the latter subsequently hydrolyzes to form insoluble titanium dioxide. This film may reduce corrosion propagation.
In the absence of oxygen, when severe corrosion attack has occurred in a reducing hot acid solution, a matt silver-gray surface is observed, due to the formation of titanium hydrides in the film.
Titanium corrosion resistance is strongly dependent on the resistance of its protective oxide, which can vary as a function of the surrounding environment [9].

Marine

Titanium is highly resistant to uniform corrosion in the marine environment and does not suffer microbial-induced corrosion (MIC). From the studies carried out, it has been shown that titanium has a greater resistance than stainless steel, copper, and nickel alloys and also has excellent resistance to corrosion at high temperatures (up to 260°C).
These properties make titanium suitable for a variety of applications involving seawater, starting from thin-walled heat exchanger tubing, up to submarine hulls, ships, platforms, desalination plants, salt production evaporators, and water jet propulsion systems [10][11].

Human Body

Due to its biocompatibility, low toxicity, high mechanical strength, and low density, titanium is an excellent material for the production of orthodontic, prosthetic, and cardiovascular implants (figure 1.5) [12].



Figure 1.5: Prosthetic and orthodontic implants of titanium

When titanium is in the fully passive condition, corrosion rates are typically less than 0.02 mm/yr and well below the 0.13 mm/yr which is the maximum corrosion rate commonly accepted for biomaterial design and application. This minimal acceptable corrosion rate is primarily due to the finite +4 oxidation of titanium alloys owing to the formation of adherent TiO_2 film although the surface oxide is more complex than a single TiO_2 oxide over their surface.
At times general corrosion in aqueous body fluids like phosphate buffer saline (PBS), ringer's lactate (RL), normal saline (NS) may take the mottled form, severely roughened metal surface that resembles localized attack. This uneven localized attack results from variations in the corrosion rate of localized surface patches due to localized masking of metal surfaces by process scales, corrosion products, food lodgment and surrounding, and adjacent superstructures.
General corrosion becomes a concern at high temperatures in highly acidic environments owing to the consumption of hot, spicy, and sticky foods. In strong and/or hot reducing acids (plaque deposits) the oxide film of titanium can deteriorate and dissolve, and the unprotected metal is oxidized to the violet-colored soluble trivalent ion (Ti^{3+}) in acid solutions which is further converted to pale yellow Ti^{4+} ion in presence of oxidizing species which on further hydrolysis may form insoluble TiO_2 precipitates/ scales and inhibiting subsequent corrosion [13].
Titanium biocompatibility is strongly related to its corrosion resistance; in fact, lower corrosion means lower amounts of ions released into the human body, which may lead to prosthesis rejection. Moreover, it is possible to treat titanium surfaces by anodic oxidation, promoting the growth of its oxide, which, if properly tuned, can stimulate the growth of hydroxyapatite, one of the principal components of bone, thus further promoting biocompatibility [14].

Fluoride-containing environments

Fluoride ions seem to be the only ones able to destroy titanium passivity in aqueous solutions, due to the dissolution of titanium as TiF_6^{2-} and TiF_6^{3-} [15].
When passivity is lost, an abrupt increase in corrosion rate or decrease in open circuit potential (OCP) is observed. The transition for each condition is clearly

detectable. For instance, Nakagawa et al [16] investigated how the pH threshold for titanium corrosion varies with F^- concentration, and they identified a linear correlation between pH threshold and the logarithm of the fluoride concentration, as we can see in figure 1.6.

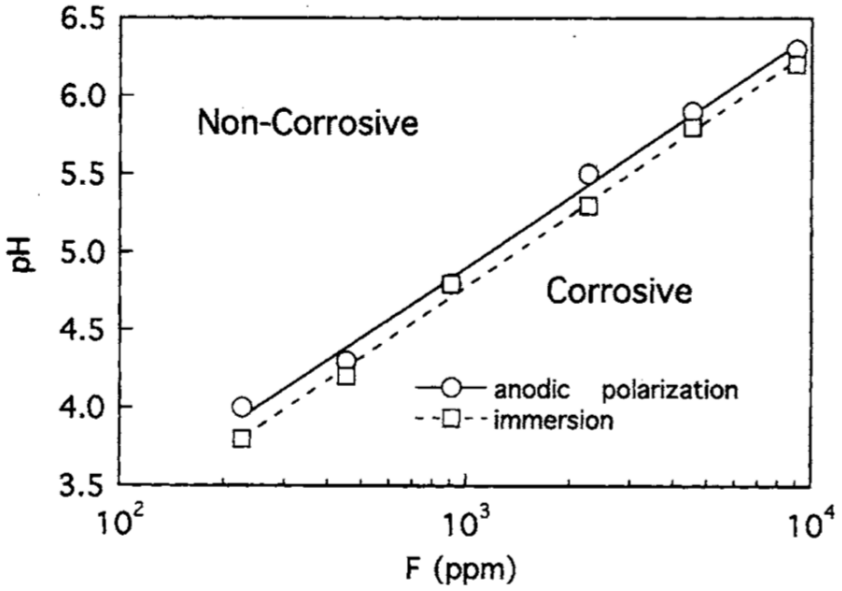

Figure 1.6: Corrosion of titanium as a function of pH and fluoride ion concentration

Further investigations from Lindholm-Sethson and Ardling [17] highlighted the existence of 3 different conditions for titanium in fluoride solutions: passive, non-passive, and active (table 1.3). These conditions where revealed by the complex impedance plane of electrochemical spectroscopy (EIS) analyses and suggest the formation of a porous surface film formed at low pH with large charge-storing ability.

Table 1.3: Classification of Corrosion Status of Titanium Based on the Open Circuit Potential (OCP), after 20 hours.

$[F^-]$ (%)	**pH**			
	7	5	4,5	4
0	Passive (P)	Non tested	Non tested	Passive (P)
0,3	Passive (P)	Non-Passive (NP)	Non-Passive (NP)	Active (A)
0,6	Passive (P)	Non-Passive (NP)	Active (A)	Non tested
1	Passive (P)	Active (A)	Non tested	Active (A)

The 3 conditions can also be distinguished by the value of final OCP obtained after long exposure to electrolytes with different fluoride content: in the passive condition OCP stabilizes at -0.1 V Ag/AgCl, in non-passive at about -0.5 V Ag/AgCl, and in the active condition at -1 V Ag/AgCl, as shown in figure 1.7.

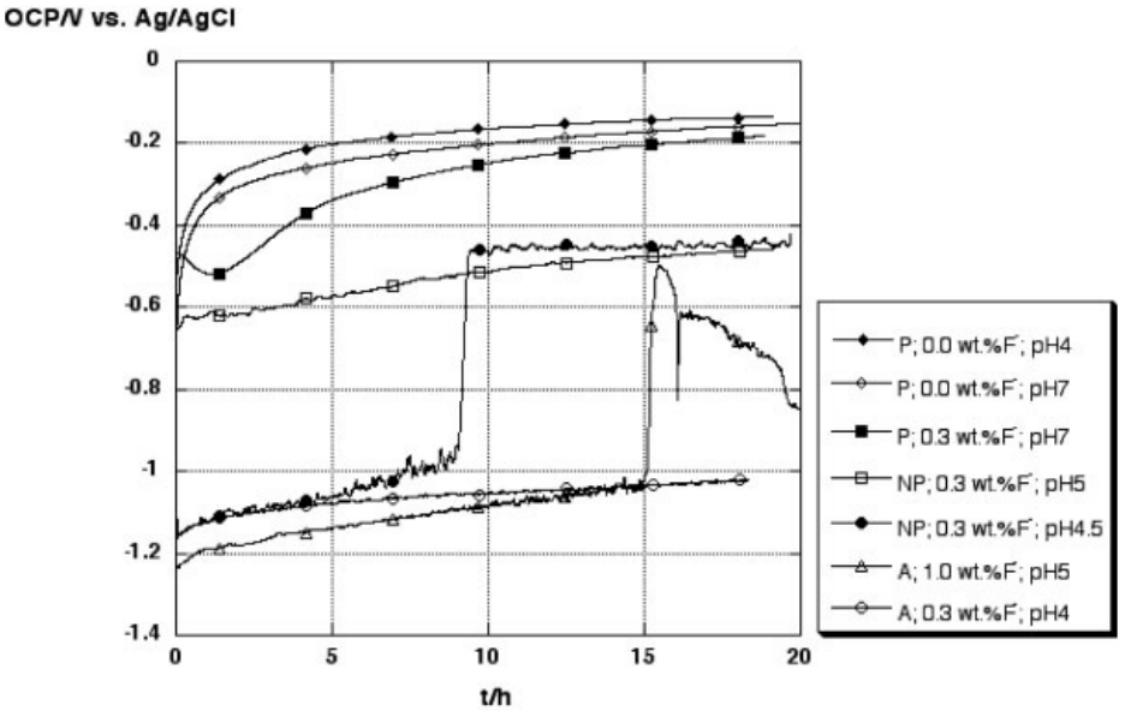

Figure 1.7: Open circuit recordings at 0.28 cm^2 titanium electrodes immersed in 0.9 wt % NaCl with 0.2 g/L $NaHCO_3$ and different pH and fluoride concentration. 20–22 h of exposure. Classification: P, passive; NP, non-passive; A, active.

Chloride-containing solutions

The most common chlorine-based acid is HCl which is a non-oxidizing acid, and therefore, titanium can't generate a passive layer. For this reason, titanium is only moderately resistant to attack in this solution. The main mechanism of corrosion in HCl is uniform corrosion.
The increase in temperature has a significant influence on increasing corrosive current density and also of corrosion rate, as we can see from the data in the table 1.4 [18].

Table 1.4: Corrosion rate (mm/year) of titanium in HCl aerated solution

HCl (%)	**35°C**	**60°C**	**100°C**	**Boiling T**
0,1				0,1
1		0,004	0,46	1,8
2		0,016		
5	0,01	1,07		
10	1,02			
20	4,45			

Other chloride-containing solutions such as NH_4Cl, become dangerous for titanium only at high temperatures [19].

Bromide-containing solutions

It was found by Heakal et al. [20] that a small amount of HBr promotes titanium passivation, while higher concentrations destroy the oxide film. The OCP of titanium varies with HBr concentration from -0.3 V Ag/AgCl in absence of HBr, to more than 0.4 V Ag/AgCl at HBy 1.0 M. This phenomenon is caused by the higher affinity of oxygen to be absorbed on the titanium surface. Accordingly, the oxide film thickness increases, and more positive free corrosion potentials are measured. In a more concentrated solution, bromide ions are adsorbed on the metal surface, displacing oxygen, and partially dissolving the passive layer, leading to an increase of corrosion rate and a reduction of the free corrosion potential.

Table 1.5: Electrochemical corrosion parameters of Ti as a function of HBr concentration at 298 K

[HBr]	$\mathbf{E}_{corr}$	$\mathbf{i}_{corr}$	η**c**	η**a**	$\mathbf{i}_{crit}$	$\mathbf{E}_{crit}$
M	mV Ag/AgCl	μA cm^{-2}	mV / decade	mV / decade	μA cm^{-2}	mV
0.01	-335	0.1	-11	190	5.15	28.88
0.1	-180	0.05	-111	125	4.42	121
0.5	480	0.03	-185	141	4.81	672
1	320	0.36	-413	211	5.7	448.7
2	290	0.9	-283	276	3.64	483
3	230	1.51	-266	239	5.02	353
4	310	1.82	-251	260	5.15	450
5	300	2.96	-206	294	7.83	451.5
6	260	3.91	-304	405	10.5	449.1
8	250	4.7	-256	318	11.2	450

As we can see in table 1.5 and in the figure 1.8, the corrosion current density (i_{corr}), which determines the corrosion rate, has a minimum when the concentration of HBr is equal to 0.5 M.

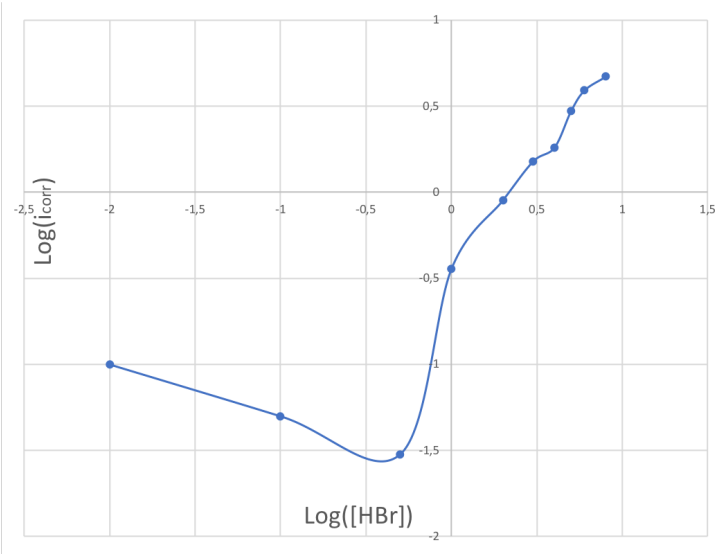

Figure 1.8: Dependence of i_{corr} on HBr molar concentration

Nitric acid

Nitric acid solutions are strongly oxidizing, so it would be expected that titanium would not suffer corrosion in them. At room temperature, titanium is immune to corrosion up to 65% HNO_3 [9].
The corrosion rate increases with the increase of temperature and HNO_3 concentration, as shown in table 1.6 [21].

Table 1.6: Corrosion rate (mm/year) of titanium in HNO_3 aerated solution [21].

HNO_3 (%)	**25°C**	**40°C**	**50°C**	**60°C**	**70°C**	**200°C**	**270°C**	**290°C**
10	0,005	0,003						
20		0,005						0,305
30	0,004		0,015					
40	0,002		0,016			0,061		
50	0,002			0,037				
60	0,001			0,04				
70	0,005			0,04	0,04		1,22	

Unlike many other metals, the higher the impurity level in the acid, the higher is titanium's corrosion resistance; the presence of Si^{4+}, Cr^{6+}, Fe^{3+}, Ti^{4+} ions in nitric acid inhibits high-temperature corrosion of titanium in it.

Sulfuric acid

Titanium exhibits resistance to corrosion by dilute solutions of pure sulfuric acid at low temperatures. Unalloyed titanium is resistant to concentrations of about 20% sulfuric acid at 0°C. This drops to around 5% acid at room temperature.
In boiling sulfuric acid, unalloyed titanium exhibits high corrosion rates in solutions with as low as 0.5% sulfuric acid. The data on titanium corrosion in H_2SO_4 are shown in table 1.7.

Table 1.7: Corrosion rate (mm/year) of CP titanium in H_2SO_4 aerated solution [21].

H_2SO_4 (%)	**25°C**	**35°C**	**60°C**	**100°C**	**Boiling**
1	0,0025		0,08	7,16	17,8
3	0,005		0,013	23,4	
5			4,83		25,4
10	0,25	1,27			
40	1,8	8,64			
75	10,8	10,7			

Grade 7 alloy is resistant to approximately 45% acid at room temperature.
Grade 12 alloy has effective resistance to about 1% boiling acid. Grade 7 alloy has effective resistance in boiling sulfuric acid to about 7% concentration. Grade 5 alloy has slightly less resistance than unalloyed titanium.
The presence of some oxidizing agents or multivalent metal ions in sulfuric acid prevents corrosion of titanium like HCl. For example, ferric and cupric ions prevent the corrosion of unalloyed titanium in 20% sulfuric acid. Oxidizing agents such as chromic acid, nitric acid, and chlorine are also effective inhibitors [22].

Phosphoric acid

Unalloyed titanium exhibits resistance to naturally aerated pure solutions of phosphoric acid up to 30% concentration at room temperature. This resistance extends to around 10% pure acid at 60°C and 2% acid at 100 °C (table 1.8).
Boiling solutions considerably speed up the attack. Grade 7 alloy provides considerably enhanced resistance. At room temperature, 60°C, and boiling temperatures, grade 7 alloy withstands concentrations of about 80%, 15%, and 6% of pure phosphoric acid, respectively.
Grade 12 provides slightly better resistance to phosphoric acid compared to unalloyed titanium, but not as good as grade 7.
The presence of multivalent metal ions, such as cupric or ferric ions, or oxidizing species can prevent titanium corrosion in phosphoric acid.

Table 1.8: Corrosion rate (mm/year) of CP titanium in H_3PO_4 aerated solution [21].

H_3PO_4 (%)	**25°C**	**35°C**	**52°C**	**60°C**	**66°C**	**80°C**	**100°C**	**200°C**	**Boiling T**
0.5									0.094
1							0.003	0.001	0.266
2									0.86
3							0.99		
5		0.0033		0.06	0.005		2.36	0.48	3.5
6					0.117				
9			0.03						
10	0.02	0.005	0.38	0.09	0.09	1.83	5		
12	0.005								
20	0.076	0.015		0.33			17.4	55.64	
30	0.051			1.5			26.4		
40		0.33							
50		0.46							
60		0.56							
70		0.66						180	
80	0.762	0.74							
85		0.76						>180	

Organic acids

Pure titanium and titanium alloys are very resistant to organic acids.
Null corrosion can be expected in weak organic acids such as adipic, hydroxy acetic, acetic, terephthalic, tannic, stearic, maleic, tartaric, benzoic, butyric and succinic acids, up to 100°C. Corrosion rates can become significant in stronger, deaerated acids as acid concentration and temperature increase.
Examples of stronger acids are lactic and formic acids (which are present in the oral cavity) [9][23].

1.4.2 Pitting corrosion

Pitting is a localized corrosion phenomenon which is typical of active-passive metals in oxidizing chloride-containing environments: the passive film breaks locally, then corrosion proceeds at the damaged spot, few millimeters wide or even less, creating

a macrocell with the surrounding intact passive metals (figure 1.9) [7].
The susceptibility to pitting corrosion is strongly dependent on temperature and halide ions concentration, the severity of which in general follows the order $F^- < Cl^- < I^- < Br^-$ [24].

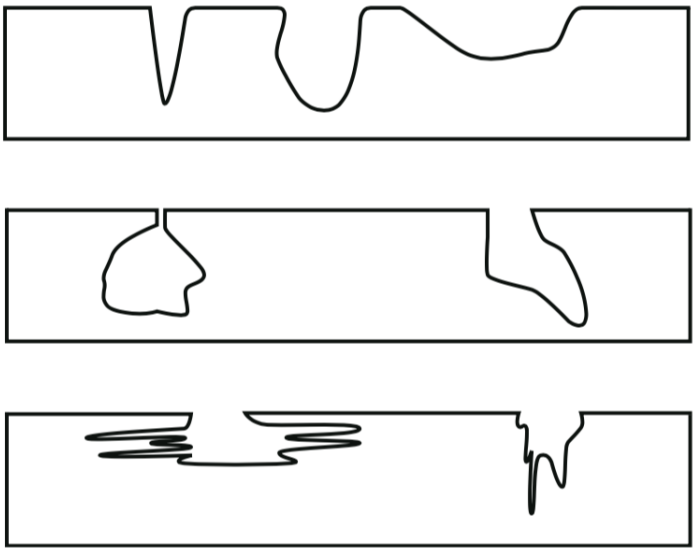

Figure 1.9: Typical forms of pitting attack

The resistance to pitting corrosion of titanium is generally very high (though less resistant in iodide or bromide solutions) because of its protective oxide film; conditions for the initiation of pitting corrosion on titanium are highly concentrated at temperature >100°C and potentials >1 Volt [25][26].

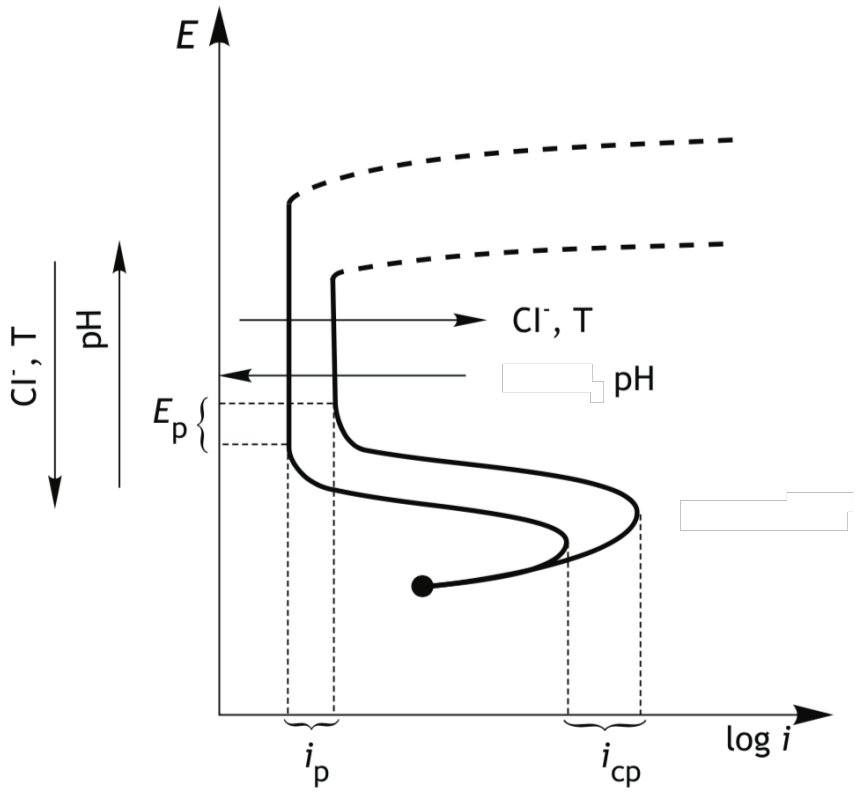

Figure 1.10: Effects of temperature, [Cl^-], pH on active-passive metals

As we can see in figure 1.10 an increase in temperature or the halide ions concentration or a decrease of pH decreases the pitting potential and increases the current density, thus increasing the corrosion rate.
Observing the breakdown phenomenon is very difficult since it is a rare occurrence that happens extremely rapidly on a very small scale. The passive film is not a uniform, compact layer as generally represented but has a different thickness, structure, composition and protectiveness, and shows dynamic behavior: some finite passive current density continuously passes through it and is evidence of film thickening, dissolution into the environment or a combination of the two [27].
Three pitting mechanisms are proposed: penetration, adsorption, and film breaking (figure 1.11).

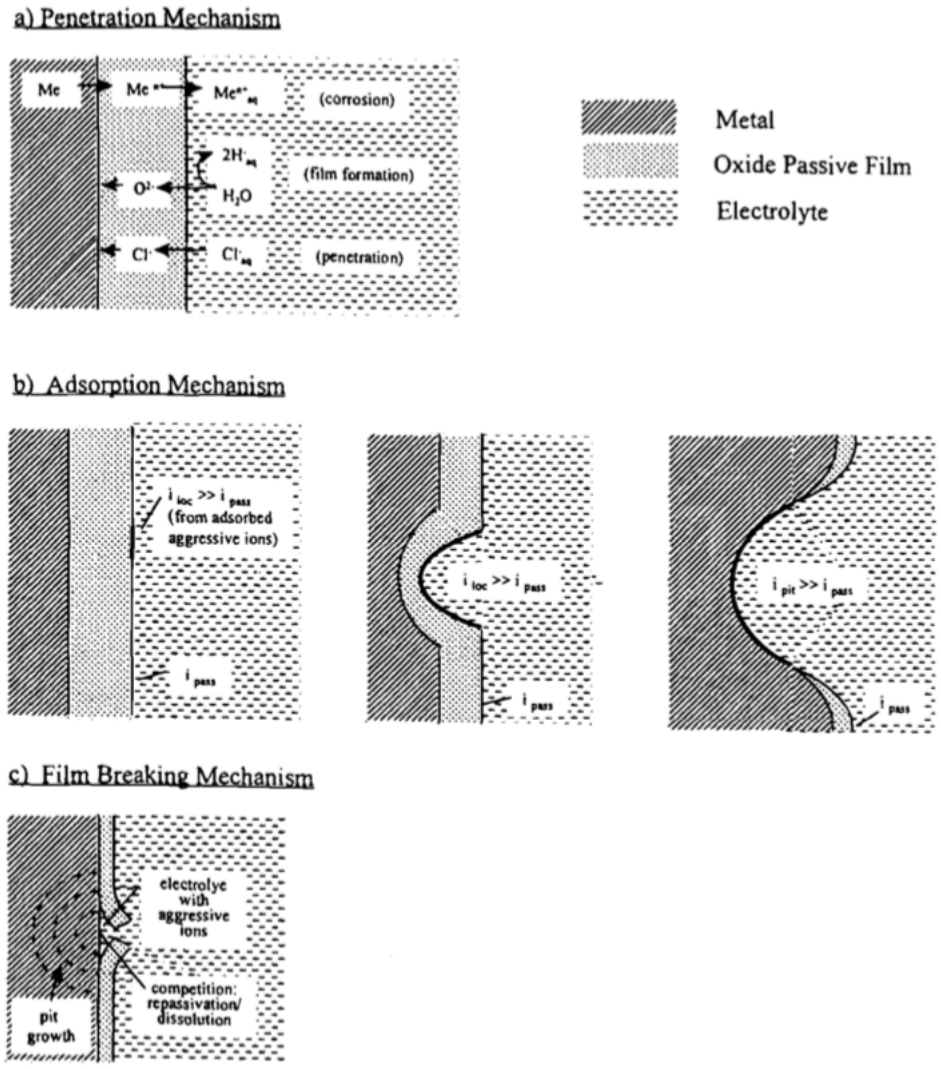

Figure 1.11: Schematic representation of (a) penetration, (b) adsorption and thinning, and (c) film breaking

Penetration involves the transport of aggressive anions through the passive film to the metal/oxide interface, where aggressive dissolution is promoted. Anion migration is assisted by the high electric field in the film.
The adsorption theory describes the incorporation of anions at the surface, providing a thinning of the passive film, thus the local electric field strength increases, leading to breakdown and formation of pits.

Pit initiation by film-breaking mechanism considers that the thin passive film is in a continuous state of breakdown and repair. Mechanical stresses at weak sites or flaws resulting from electrostriction and surface tension effects may cause local breakdown events[28].

1.4.3 Crevice corrosion

The most dangerous form of localized corrosion to which Ti and its alloys are susceptible is crevice corrosion. Crevice corrosion is an insidious form of corrosion that occurs in cracks and gaps between adjacent metal surfaces, or spaces between metals and other solid materials that hinder mass transport.
Crevice corrosion, like pitting, is a type of occluded cell corrosion, that is, corrosion occurs on an area of the metal surface that is exposed to a volume of solution that has stagnated and developed aggressive local chemical conditions due to restrictions in mass transport.
A schematic diagram of the processes involved in crevice corrosion on Ti is given in figure 1.12.

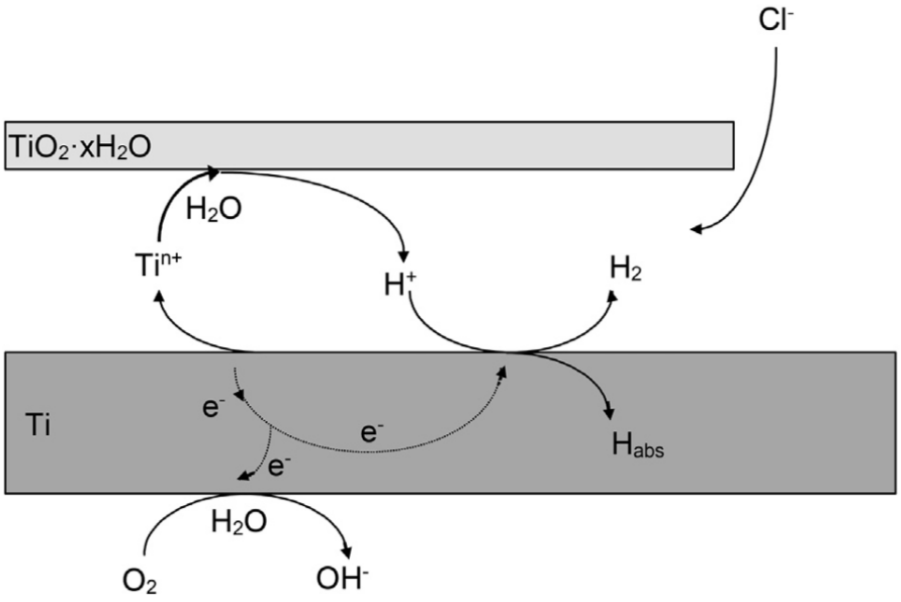

Figure 1.12: Schematic depiction of crevice corrosion and the chemical processes involved.

Metal oxidation within the crevice is driven by oxygen reduction on the crevice exterior. Metal dissolution is followed by cation hydrolysis, which results in precipitation of corrosion product deposits and acidification of the crevice interior. Once the crevice anolyte pH is low enough, metal oxidation can also couple to proton reduction within the crevice. This is a self-sustaining reaction, producing more protons by cation hydrolysis while other protons are reduced in driving corrosion. The proton reduction reaction leads to hydrogen gas evolution and hydrogen absorption by the metal. Autopassivation by Ti species is a possibility if active and passive sites coexist within the occluded area [29].
The lifetime of a corroding crevice can be divided into three phenomenological

phases: initiation, propagation, and repassivation. Initiation requires that sufficiently aggressive chemical conditions (e.g., low pH, low concentration of dissolved oxygen) develop within the crevice that the passive oxide film is penetrated and the underlying metal can achieve an active state.
Propagation, that is, the continuation and spread of crevice corrosion, requires that part of the metal be maintained in an active state (which, in turn, requires specific conditions of pH and potential) and part of it be supplied with oxidant. This oxidant can be oxygen or another oxidizing species that is reduced on the passive surfaces of the metal in areas outside of the occluded region, or it can be protons that are generated within the occluded region by hydrolysis of metal ions and reduced to hydrogen within the crevice interior.
Repassivation occurs when the chemical conditions or electrochemical potential required for active behavior can no longer be maintained within the crevice, and a passive oxide film is regrown on the corroding surfaces. This could happen as a result of (1) increased mass transport within the crevice (e.g., due to an increase in the crevice gap dimensions), which would cause an increase in the local pH, oxygen ingress within the occluded region, or a change in the potential drop at the metal/-solution interface; (2) an increase in the rate of the cathodic reaction, which could generate anodic protection (e.g., autopassivation by Ti); or (3) decreased availability of oxidant.
While this division of the crevice corrosion process into initiation, propagation, and repassivation phases is convenient for descriptive purposes (and these phases must occur in sequence for a given point within a crevice), local initiation, propagation, and repassivation can take place simultaneously at different locations within a corroding crevice throughout its lifetime [30].

1.4.4 Stress corrosion cracking

When a susceptible metal is in contact with a specific environment, in presence of tensile stress exceeding a threshold, the corrosion-enhanced formation of cracks and catastrophic failure is called stress corrosion cracking (SCC) [7].
There are two basic mechanisms: one as anodic and another one as cathodic. The growth of cracks takes place according to one of the following mechanisms:

- Crack tip dissolution (called slip-dissolution) is based on the anodic dissolution of the metal (figure 1.13 a).

- Crack tip rupture caused by atomic hydrogen, produced by the cathodic process, which enters the metal and accumulates at crack tip (called Hydrogen Embrittlement, HE)(figure 1.13 b).

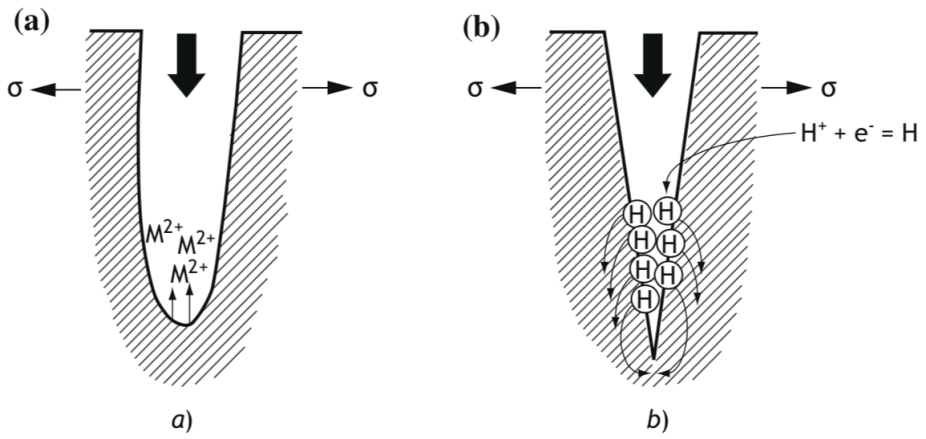

Figure 1.13: Simplified representation of SCC mechanisms: a) slip dissolution; b) hydrogen embrittlement (HE).

SCC related failures often appear without plastic deformation, then, at first sight, it could be mistaken for a fracture of brittle material; instead, metals suffering SCC are normally ductile. Cracks form and grow in a perpendicular direction to maximum tensile stress and do not show visible corrosion products.
Figure 1.14 depicts the morphology of cracks which depend on metal, environment and entity and distribution of stresses, cracks are mainly inter-crystalline (intergranular) or trans-crystalline (transgranular) and are more or less branched.

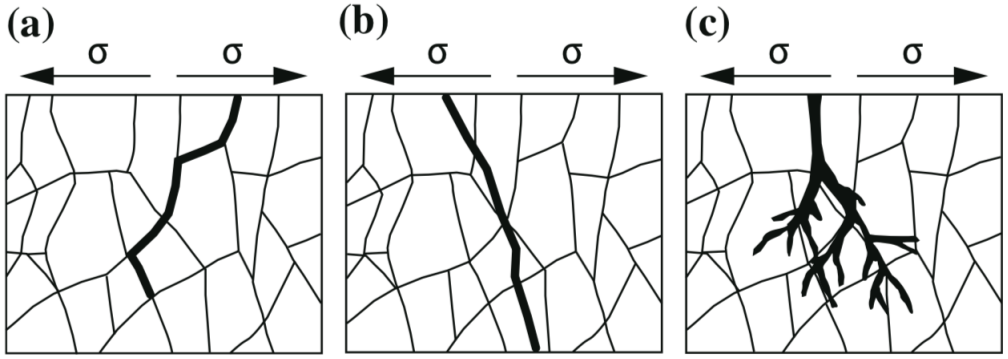

Figure 1.14: Depict of the appearance of cracking propagation in SCC: **a** intergranular; **b** transgranular; **c** delta river transgranular

The halide anions Cl^-, Br^-, and I^- are the only ions that have been shown to either (a) accelerate cracking in alloys susceptible to SCC in distilled water or (b) induce susceptibility in alloys immune to SCC in distilled water as we can see in figure 1.15. The additions of other anions produce neither of the above effects and may in some cases inhibit SCC [31][32]. Examples of such neutral or inhibiting ions are NO_3^-, SO_4^{2-}, OH^-, CrO_4^{2-}, and PO_4^{3-}. The ability of these ions to inhibit SCC depends on the alloy and its heat treatment [33].

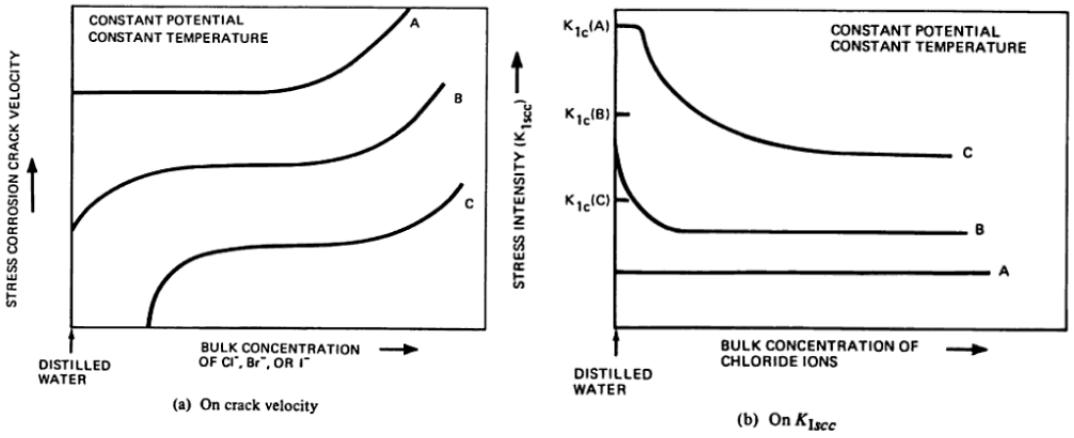

Figure 1.15: Schematic of the influence of halide ion concentration and metallurgical factors.

1.4.5 Hydrogen-induced cracking

Although SCC takes into account hydrogen adsorption to promote cracking, hydrogen-induced cracking (HIC) requires much more hydrogen to be absorbed by the metal. When hydrogen is adsorbed in the metal, it causes embrittlement, depending on the nature of the metal.
In the case of titanium, hydrogen absorption has two consequences:

- the precipitation of a new microstructural titanium hydride phase.
- the generation of methane gas bubbles due to a chemical reaction with carbon at the grains boundary (failure is due to the growth of voids) [9].

Titanium grade 2 can be very susceptible to hydrogen embrittlement, especially at high temperatures. In this situation, hydrides are formed and they cause a decrease in the elongation to failure.
When the size and volume fraction of the hydrides increases, the elongation to failure decreases and the fracture surface also changes from ductile microvoid coalescence to brittle fracture[34].
Alloying elements (such as iron) can influence hydrogen absorption into titanium alloys through the formation of intermetallics, which act both as hydrogen windows and storage sites.
Also the microstructure plays a fundamental role in this process; in the titanium, the β-phase has a higher hydrogen diffusivity than the α-phase. For this reason, HIC in titanium, having only α-phase, is much lower than in α-β titanium where the beta phase acts as channels in which hydrogen travels quickly and permeates the material faster. Then, the hydrogen precipitates in the α-phase, promoting crack formation.
When β-phase content is high enough, it can dissolve hydrogen, preventing hydride precipitation and secondary cracking [35][36].

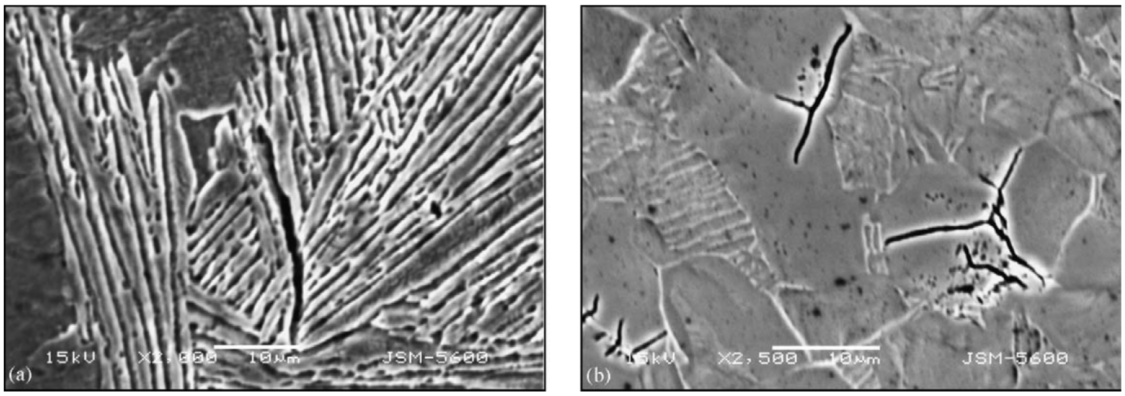

Figure 1.16: SEM micrographs of Ti-6Al-4V alloys after electrochemical hydrogenation revealing HIC in: (**a**) the fully lamellar microstructure, between the α and β lamellas; (**b**) duplex microstructure, in the boundaries and inside the equiaxied grains of primary α.

The influence of surface oxide on the absorption efficiency is remarkable, and the presence of passive oxides has been shown to almost completely suppress hydrogen absorption even in hot aggressive brine environments [37].
An example of visible HIC in the microstructure has been provided in figure 1.16.

Chapter 2

Treatments to improve corrosion resistance

To solve many of the problems that titanium shows in aggressive environments, several techniques are used. As already seen in the corrosion assessment of titanium, also this high corrosion-resistant metal exhibits problems in very aggressive environments.
However, the rate of corrosion varies greatly changing the metal and the environment, spanning from millimeters per day (galvanic coupling or impressed currents) to millimeters per millennia (negligible).
Corrosion is a surface phenomenon, so the development of a protective passive layer is required to reach a passive state, in which corrosion proceeds at very low rates. For this reason, barrier layer modification treatments are crucial to increase the corrosion resistance of metals.

2.1 Alloying with noble metals

A small addition of alloying elements can have dramatic influences on the electrochemistry of titanium. Alloying can be used to generate passivity on titanium in two ways:

- inhibiting the anodic half-reaction
- enhancing the cathodic half-reaction

Specifically, alloying with elements that could induce a decrease in the critical anodic current density or the passivation potential would make it easier for the cathodic half-reaction to drive the potential into the passive region.
Alternatively, alloying with elements that catalyze the cathodic half-reaction, either by increasing the exchange current density or decreasing the cathodic Tafel slope, would also make it easier for the cathodic half-reaction to drive the potential into the passive region. Alloying to enhance the cathodic reaction rate for this purpose has been termed "cathodic modification".
In either case, the solution must contain a redox system with a reversible potential nobler (i.e. higher) than the Flade potential. The H^+/H_2 satisfy this condition on titanium.
The cathodic route to passivity must be approached with caution; however, because

if the kinetics of the cathodic half-reactions are enhanced, but not enough to reach the passive region, the corrosion rate of the alloy will also be increased. This is the case for binary Ti-C alloys containing particles of titanium carbide (TiC), a material on which the cathodic polarization curve in 10% H_2SO_4 at 100°C is "enhanced" over that of Ti, but still intersects the anodic polarization curve of Ti in the active region.
Consequently, TiC particles cannot effect passivation of the alloy under these conditions but instead enhance corrosion.
Alloying elements that can induce passivity of Ti by cathodic modification include Pt, Pd, Ni, Ru, Re, Fe, Ir, Os, Rh, and Au. Their relative effectiveness is roughly in the same order as their hydrogen overvoltages and exchange current densities for hydrogen reaction. This relation between effectiveness and exchange current densities, along with the high corrosion resistance or immunity of most of these elements, make it possible to produce very good cathodically modified alloys on a commercial scale.

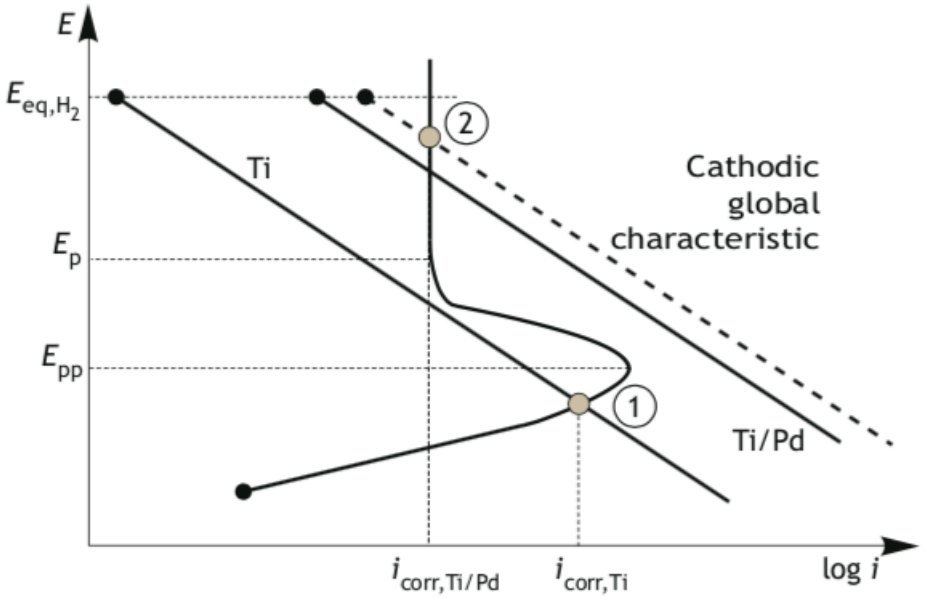

Figure 2.1: Anodic protection effect by cathodic alloying with Pd (or Pt) [7].

The most used alloying element is palladium (titanium grade 7), because, as we can see in figure 2.1, the current density of the alloyed titanium is lower (the metal is in the passive region) than the current density of pure titanium and so the corrosion rate is lower.
The low alloy required (<0.1 wt%) for maximum cathodic modification effect is also critical to the commercial viability because the cost of higher noble metal content would make these alloys uneconomical.
While cathodic modification offers greatly increased resistance to active corrosion of titanium and the alloying additions are often small enough not to significantly influence the mechanical/physical properties of the material, there are some caveats-cathodically modified alloys that sometimes suffer increased hydrogen absorption efficiencies and higher passive corrosion rates than unalloyed titanium.
The inhibition of the anodic reaction on titanium lowers the critical current density for passivation. This is a very different approach to achieving passivity on titanium

than the cathodic modification approach. The two approaches can be used in combination to enhance the ability of titanium alloys to passivate.
Alloying elements that suppress the titanium dissolution reaction tend to be those that yield adherent, insoluble oxide compounds, such as Mo, Nb, Cr, W, Zr, and Ta.
There are two ways in which alloying elements could act to inhibit anodic dissolution of active-passive alloys, namely, by improving the thermodynamic stability of the metal or that of the oxide. Two groups of alloying elements can be identified based on the comparisons of the heat of adsorption of oxygen on the pure elements versus the metal-bond energy:

- passivity promoters
- dissolution moderators (blockers)

Passivity promoters, which include Ti and Cr, are elements that have high metal-oxygen bond strength and a relatively weak metal-metal bond; the latter facilitates oxidation and the formation of a three-dimensional oxide layer, which requires the breaking of metal-metal bond, while the former increase the stability of the passive oxide formed.
Dissolution moderators including Mo, Nb, Ta, W, and Zr, have high metal-metal bond strengths, in addition to strong metal-oxygen bonds. Having strong metal-metal bonds increases the activation barrier for metal dissolution, while the strong metal-oxygen bonds promote passive film stability.
In practice, it appears that none of these elements is capable on its own of limiting titanium dissolution enough that the hydrogen reduction reaction on titanium can drive the potential into the passive region, unless, present in relatively high concentrations. However, complementary additions of cathodically modifying and anodically suppressing elements are effective in promoting the passivation of dilute alloys.
Unfortunately, the passive corrosion rates on titanium alloys that resist active dissolution can be higher than those on unalloyed titanium. The susceptibility of some of these alloy additions, such as Mo and Cr, to transpassive dissolution results in conversion of the oxide to a more "TiO_2-like" structure at high potential, which renews the passivity [29][30].

2.2 Thermal oxidation

Thermal oxidation is considered as a cost-effective method to deliberately generate a barrier oxide layer of a relatively high thickness ($\sim$20-30 μm) on titanium compared to the naturally formed oxide layer (typically of 4-6 nm).
Thermal oxidation of titanium is aimed to produce in situ ceramic coatings, mainly based on rutile, in the form of a thick, highly crystalline oxide films, which is accompanied by the dissolution of oxygen beneath them. The thermally formed oxide layer enables an increase in hardness, wear resistance, and corrosion resistance of titanium and its alloys [38].
The fundamental parameters in this type of process are time and temperature.
By increasing the time at a constant temperature, a thicker and more rough oxide is obtained; the increase in thickness is a positive factor for resistance to corrosion

and fretting as it increases the microhardness of the material and also increases the protective barrier to counteract the diffusion of oxygen in the oxide, the increase in roughness is a negative factor as regards fretting resistance due to the breakage of small oxide particles which increase wear.
By increasing the temperature at a constant time, a thicker oxide is obtained; however, an excessive increase in the oxidation temperature can generate thermal stresses in the oxide film which generate defects through which oxygen diffusion can occur, thus reducing the effectiveness of the treatment [39][40][41][42].
Kumar et al. investigated the role of time on a thermal oxidation treatment at 650°C on titanium for medical application. For this type of applicationm the material must resist fretting and corrosion very well.

Table 2.1: Microhardness and thickness variation as a function of thermal oxidation time

Treatment condition	Surface microhardness (HV)	Thickness (μm)
Untreated CP-Ti	178±6	0,02
CP-Ti thermally oxidized at 650°C for 8 h	365±9	3,9
CP-Ti thermally oxidized at 650°C for 16 h	396±15	7,5
CP-Ti thermally oxidized at 650°C for 24 h	443±20	12
CP-Ti thermally oxidized at 650°C for 48 h	679±43	19

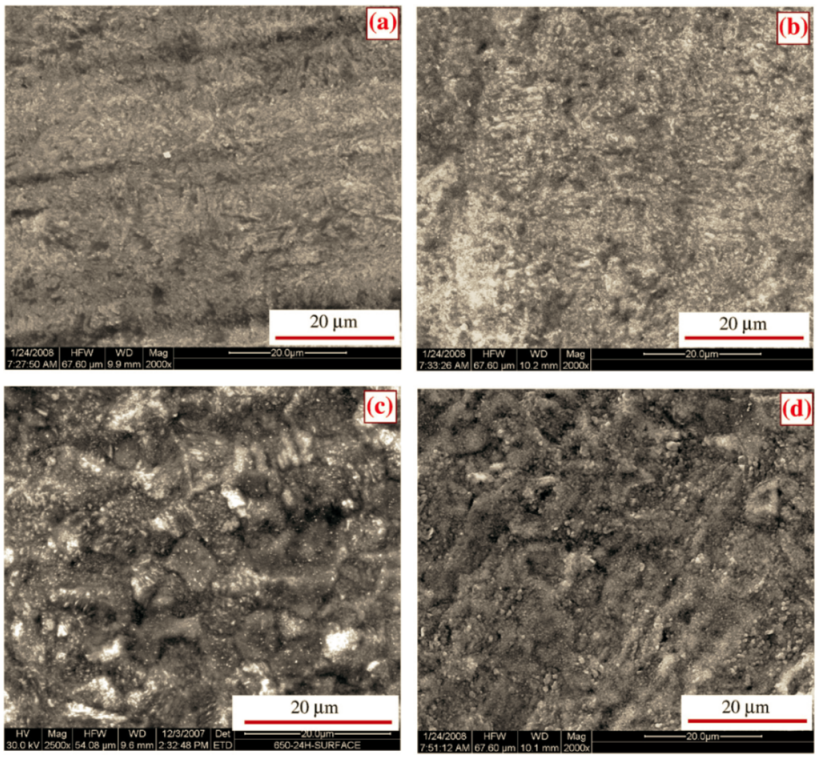

Figure 2.2: SEM images of surface morphology of samples thermally oxidized at 650°C for various time periods; (a) 8, (b) 16, (c) 24 and (d) 48 h.

The best condition is obtained at 48 hours because, although the roughness is the highest at this time as we can see in figure 2.2, the hardness and thickness of the oxide is maximum and therefore the fretting resistance will be greater as reported in table 2.1.

The corrosion resistance was studied by means of a potentiodynamic test in the Ringer's solution.

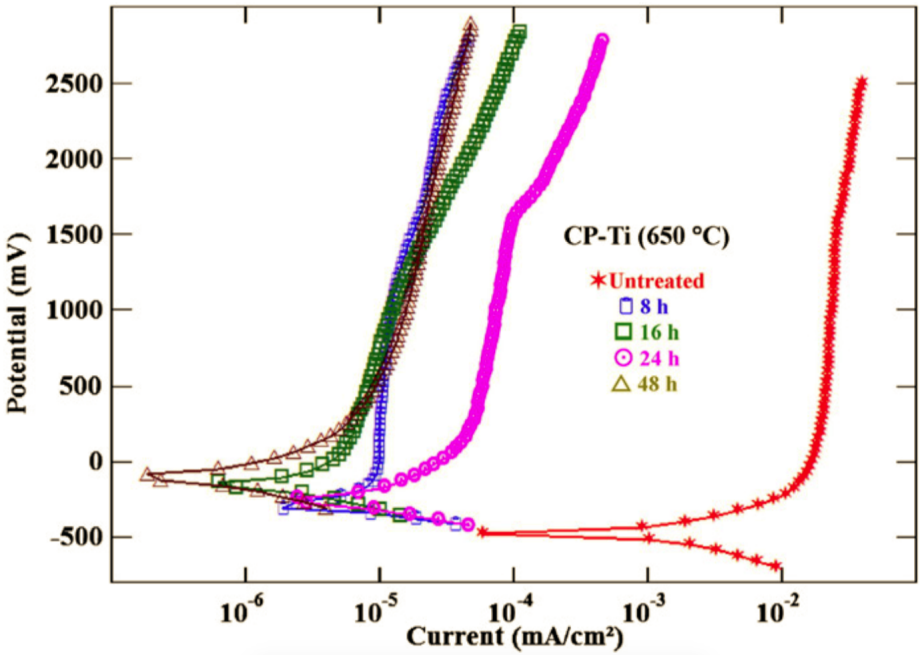

Figure 2.3: Potentiodynamic polarization curves of untreated and thermally oxidized samples.

As we can see in potentiodynamic polarization curves in figure 2.3 the effect of thermal oxidation is beneficial for corrosion resistance because the current is reduced by three orders of magnitude [43].

2.3 Anodizing

Titanium is a transition metal that belongs to the class of "valve metals" which are those metals forming a compact and adherent oxide layer, which increases the electrical resistance when anodically polarized. This allows us to have a conductive electrode in the cathodic direction, while in anodic direction it is polarized.
Thus, it is possible to grow a controlled oxide layer on the metal by anodizing, with several possible applications.

2.3.1 Process setup

Anodizing is an electrochemical process where the oxidation of a metal, working as the anode, is induced by the flow of current (generally, but not exclusively, a direct current) from an external power supply. This process has been largely used since the early 20th century for the growth of oxide layers on metals. An anode and an inert counter electrode, used as the cathode, are placed in an electrochemical cell and connected to a power supply; the application of an electrical stimulus results in the growth of an oxide layer on the metal anode.
In anodizing, the coating is produced at the "expense" of the substrate, i.e., it could be viewed as a "conversion process"; however, since the oxide coating has a greater

volume than the titanium substrate, there is an overall increase in dimensions.
The process is performed in two main regimes:

- *Galvanostatic conditions*: A constant current is applied between anode and cathode, from few A/m^2 up to hundreds A/m^2, untile the desired cell voltage is reached or a determined charge has traveled through the cell.

- *Potential sweep*: Cell voltage, that is, the potential difference between anode and cathode, is gradually increased from zero to a predefined value, with voltage ramps generally in the range 0.5 V/s to 1 V/min.

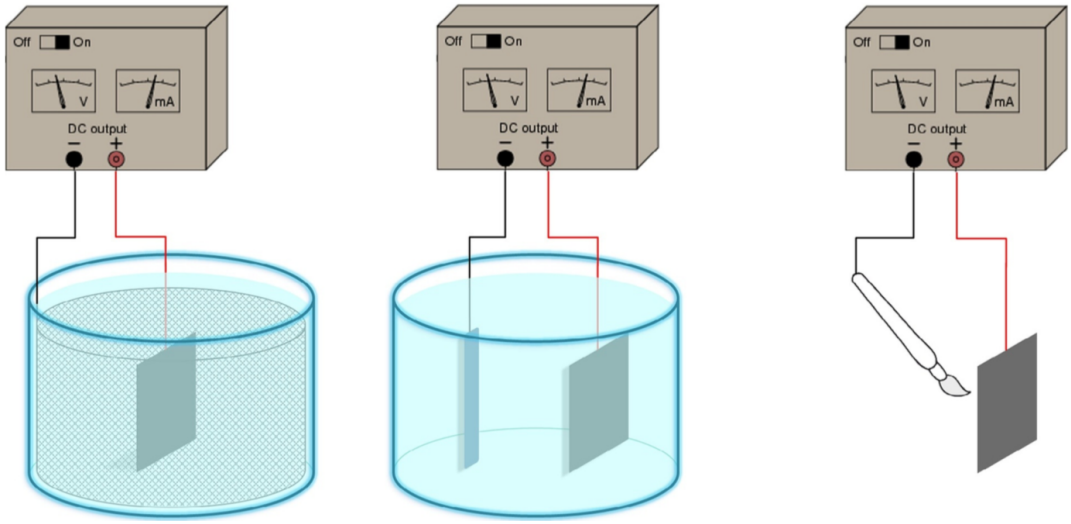

Figure 2.4: Anodizing of titanium in an electrochemical cell. *Left*: cathode surrounding the whole titanium specimen, *center*: frontal cathode, *right*: hand painting with electrochemical brush

Whichever the growth mode, process feature that most affect oxide properties pertain to both electrochemical parameters (applied voltage, current, presence or absence of a stabilization time after reaching the desired voltage) and electrolyte composition, pH, and temperature. The metal substrate composition and surface finishing also play a key role, as impurities and alloying elements change not only oxidation kinetics but also the extent of oxide crystallinity and the possibility to control the nanostructure.
Also the output can be modified from the cell setup: while the choice of counter electrode material only influences to a minor extent, the different cell geometries that can be adopted have a more important role, among which the most common are reported in figure 2.4 (left and center). If the counter electrode surrounds the whole titanium specimen, oxide growth is assumed homogeneous on both metal sides, while if it is from facing the titanium specimen growth will be different on the two sides due to an uneven current distribution. Eventually, artistic anodic oxidation can be obtained with the use of a brush as an artistic counter electrode, that is, a brush containing a copper wire connected to the power supply, which has been impregnated with suitable electrolyte (figure 2.4, right).

2.3.2 Oxide growth

Ideally, on a titanium substrate immersed in an electrolyte, forcing an electric field by applying a potential difference between titanium and a cathode induces the following redox reactions:

$$Ti \rightarrow Ti^{4+} + 4e^- \tag{2.1}$$

$$Ti^{4+} + 2H_2O \rightarrow TiO_2 + 4H^+ \tag{2.2}$$

$$4H^+ + 4e^- \rightarrow 2H_2 \quad or \quad O_2 + 2H_2O + 4e^- \rightarrow 4OH^- \tag{2.3}$$

Initially, metal cations bind with oxygen ions from the electrolyte at the metal/-electrolyte interface, but once an oxide layer is formed, further growth requires the migration of oxidizing anions in the film from the oxide/electrolyte interface to the metal/electrolyte one. Given the dielectric nature of the growing oxide and consequently the large resistance opposed to ion migration, ionic transport in TiO_2 follows an high-field-assisted ionic transport model. Ionic transport is made possible by the application of an electric field across the metal oxide, high enough to lower the energy barrier for ions to hop from one position to another in the dielectric. This transport process is the rate-determining on oxide growth kinetics and requires large electric fields to achieve ion migration and consequent oxide growth, in order of 0.1-1 V per nanometer of oxide thickness. For relevant oxide buildup, the main requirement is the oxide chemical stability in the chosen electrolyte: if it is too soluble, it dissolves faster than it is created, thus preventing the formation of the anodic film. This is particularly important for nanoporous and nanotubular oxides, but also for compact layers at higher solubility corresponds to lower thickness achievable.
Not only oxygen anions migrate towards the metal but also metal cations migrate toward the oxide/electrolyte interface, causing the film to grow in an intermediate position between metal and electrolyte: the contribution of anions and cation to migration is defined by their transport numbers, generally favoring the transport of oxygen, whose ion is small. When titanium ions reach the electrolyte, they may react with water rather than with oxygen:

$$Ti^{4+} + 4H_2O \rightarrow Ti(OH)_4 + 4H^+ \tag{2.4}$$

Moreover, hydroxyl ions may migrate through the oxide under the applied electric field and react with Ti^{4+} to give titanium hydroxide. Both effects contribute to the nonstoichiometry of anodic TiO_2 films which gradually dehydrate during progressive oxide growth as $Ti(OH)_4$ is transformed into TiO_2. On the other hand, the most relevant source of nonstoichiometry in completely formed oxides is the presence of oxygen vacancies, commonly leading to an overall composition TiO_{2-x}.
After a few nanometers of oxide have build-up, another anodic process becomes relevant in the electrochemical cell, that is, oxygen evolution:

$$2O^{2+} \rightarrow O_2 + 4e^- \tag{2.5}$$

Such phenomenon is allowed by the electronic conductivity intrinsic in anodic oxides, which are never perfectly stoichiometric, and often have a mixed amorphous/crystalline character, resulting in higher conductivity compared to the theoretical one. Electrons are then released by O^{2-} in the electrolyte and travel through the oxide, reaching the metal substrate, where they are collected and directed to the cathode.

Since the side reaction is very competitive from an energy point of view, part of the current provided by the power supply is lost in this parasitic reaction, in a larger amount with increasing oxide electronic conductivity.

2.3.3 Process parameters

Depending on the oxide layer characteristics that are needed, it is possible to perform the anodization with different parameters. It is fundamental to fully understand the anodic oxidation mechanism to predict how the anodizing parameters influence the result.
The titanium anodization, depending on the parameters set, can lead to three different surface layouts:

1. Amorphous and compact oxide layer up to hundred nanometers thick, which is the result of the standard anodization and leads to a coloured surface.

2. Crystalline and porous layer from few micrometers to a hundred of micrometers. It comes from the anodization beyond the breakdown voltage with the so called, Anodic Spark Deposition (ASD) or Plasma Electrolytic Oxidation (PEO) or MicroArc OXidation (MAO).

3. Titanium dioxide nanotubes derived from the anodization in presence of fluoride-containing electrolytes [44].

Current density and feeding voltage

The current density and the feeding voltage are the main parameters to tune and control layer thickness and its crystalline phase. While low voltages (below 130 V) allows to obtain an amorphous, smooth thin layer (up to 300 nm), medium-high voltages (100-500 V) are typical of the Plasma Electrolytic Oxidation process which leads to a mainly crystalline oxide, with crystallites size from few micrometers to a hundred of micrometers. This surface looks glossy with pores that are caused by the formation of arcs in the weak sites of the oxide, as shown in figure 2.5.
The high energy density they bring causes the local melting of the oxide which, on one hand, modifies oxide crystallinity, on the other allows the ions in the electrolyte to enter in the solid matrix, modifying the oxide composition [44].

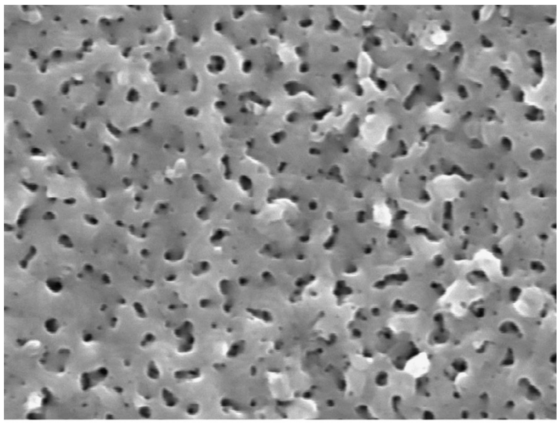

Figure 2.5: SEM image of sample anodized in 0.5 M H_2SO_4 with current density 1080 A/m^2 and cell potential 140 V: oxide surface [45].

The relationship between the anodic current and the electric field strength, across the anodic oxide film, is described by the following Eq.2.6 [46],

$$i = Ae^{(BE)} \tag{2.6}$$

where i is the ionic current, A and B are the electrolytic constants, E is the electric field strength and can be replaced by V/δ, where V is the anodizing forming voltage, and δ refers to the anodic oxide thickness.
During galvanostatic anodizing, in order to maintain the given constant current density, constant field strength, across the previously formed barrier film, is required. As a consequence, when the oxide thickness increases with time at constant current density, the voltage across the oxide film must increase in order to maintain the field strength and the current density [47].
So, during the first part of the oxide growth, the oxide layer grows linearly with the voltage applied, with a constant velocity that depends on the electrolyte, temperature, and agitation of the solution; then, at a certain voltage, which is not univocally defined, the linearity is lost because other phenomena take place (figure 2.6).

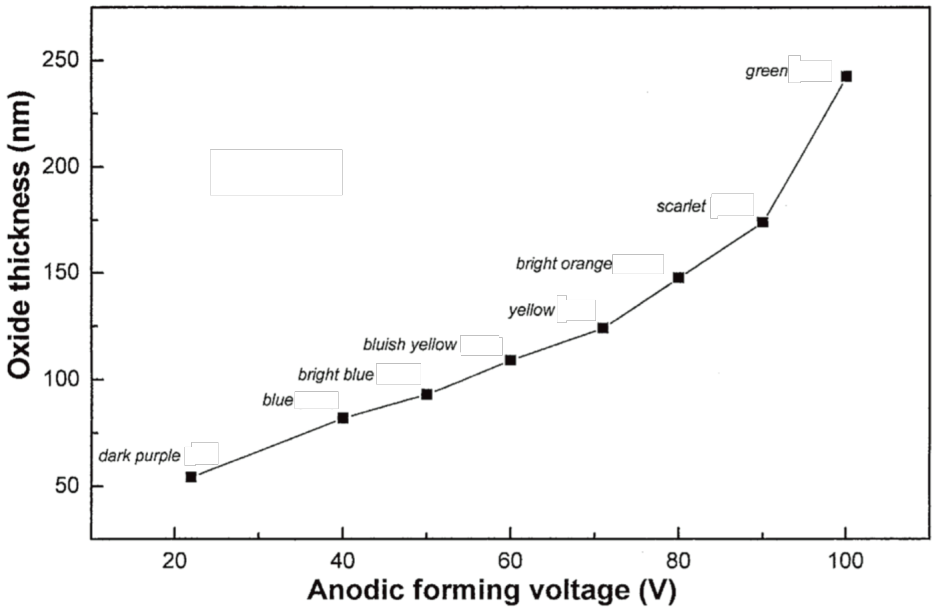

Figure 2.6: relation between oxide thickness and anodic forming voltage of pure titanium in 1.0 M sulphuric acid solution. Lost of linearity between 70-90 V[48].

The range of dielectric breakdown potentials, which is the formation of conducting paths through an insulating material in the presence of an extremely strong electric field, of TiO_2 is related to differences in the anodization electrolyte, temperature, current density, and uniformity (thickness and crystallinity) of the formed oxide.
In the dielectric breakdown conditions, the oxide is crystallized causing the loss of linearity, and the parameter that affects thickness is now the time interval of maintenance of the voltage output [49]. Another important parameter is the current density (or sweep rate); the sweep rate under the potentiostatic control is the rate of potential increase (for example 0.5 V/s). If it is high, the oxide will have less time to form, therefore presenting a more defective structure, while low current densities promote crystallization and increase film density, which improves resistance.
On the other hand, higher current densities overcome more easily the system frictions, thus allowing higher voltages, where higher crystallinities are achieved.

Electrolyte and pH

The nature of the electrolyte and its concentration play a fundamental role in the growth of the oxide, in its porosity, and its stability and adherence to the substrate. The anodic oxidation is the dynamic equilibrium result between the tendency of the electrolyte to dissolve the oxide film and its formation.
During anodizing it is necessary to use an electrolyte in which the oxide formed is stable and adherent to the metal substrate. Anodizing of titanium is never carried out in an alkaline environment since the formed oxide reaches very thin thicknesses, resulting, therefore, not protective. This is due to the fact that in such environments the growth rate of the oxide is lower than its dissolution rate. On the other hand, in an acid environment, the growth rate is much greater than the dissolution rate. This means that, in this environment, the process allows the formation of thick oxides[50].
For other metals, such as aluminum and magnesium, alkaline solutions can be used even if an acid electrolyte is more efficient, allows greater thicknesses to be obtained, and delays breakdown compared to an alkaline electrolyte containing OH^- which are promoters of the breakdown.
However, a very strong acid such as HF of $HClO_4$ has strong tendencies toward dissolving the film produced. Very weak acids, such as the usual organic acids, produce very adherent but limited thickness translucent films [51][44]. Acid compounds like sulfuric and phosphoric acids are the best for this process because, using them, the growth rate velocity exceeds the dissolution one, allowing the formation of a stable and thick oxide. Although titanium oxide is very stable in these acids, it is partially dissolved from the acidic environment. At the end of the process, there is a balance between electrically imposed growth and chemical etching (figure 2.7).

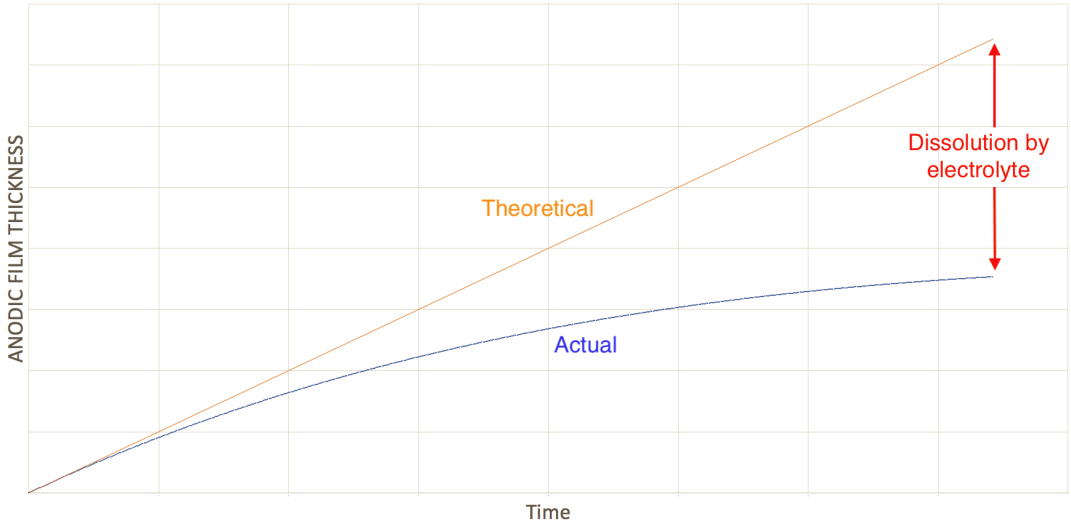

Figure 2.7: Change in film thickness during anodizing

Sulphur ions accelerate oxide breakdown and crystallization, while phosphate ions tend to be incorporated in the oxide and delay its crystallization. Instead, halides (for example fluoride and chloride ions) induce a localized oxide dissolution, creating peculiar nanostructures.
It is also possible to see that the anodic forming voltage decreases with the increase of the concentration, thus, the total amount of anodic charge and anodizing time

decreases.
Looking at the acidic components, sulphuric acid exhibits the best performances, in term of oxide growth rate, at 0.5 M of concentration.
In a study S.K. Lazarouk et al. [52] studied the effect of the electrolyte temperature during the anodizing of titanium in a solution of 0.1 M NH_4F in ethyleneglycol with 0.5 M H_2O. The anodization was performed at the electrolyte temperature ranging from -5 °C to +20 °C. The anodization voltage was linearly increased from zero to a fixed value in the range of 20-150 V with a rate of 1 V/s and then kept constant for 15 to 660 min in total.
They found that the electrolyte temperature controls maximum voltage and current density allowed to be used for anodization without breaking down the oxide: the lower the temperature, the larger the maximum voltage and current density.

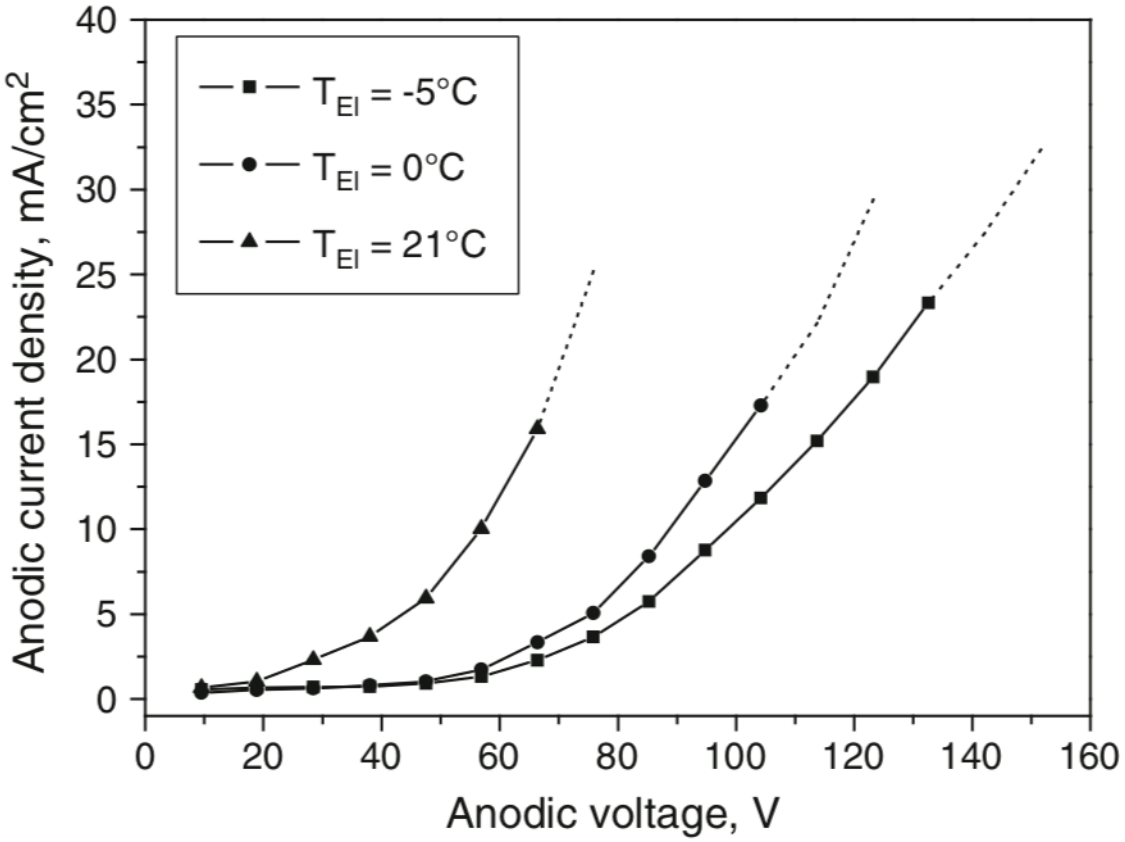

Figure 2.8: Anodic current density versus anodic voltage during porous electrochemical oxidation of titanium foils in 0.1 M NH_4F solution in ethyleneglycol at different temperatures of the electrolyte.

From figure 2.8 it is possible to see that, by increasing the temperature of the electrolyte, higher current densities are obtained at the same voltage: this is due to the fact that, by increasing the temperature, the resisitivity of the electrolyte decreases (and the conductivity increases). The temperature of the electrolyte influence also the porosity (figure 2.10) and the structure of the oxide (figure 2.9): an increase in temperature increases the kinetics of the dissolution of the oxide (etching rate), in acid environment, increasing the dimension of pores and decreasing their circularity.

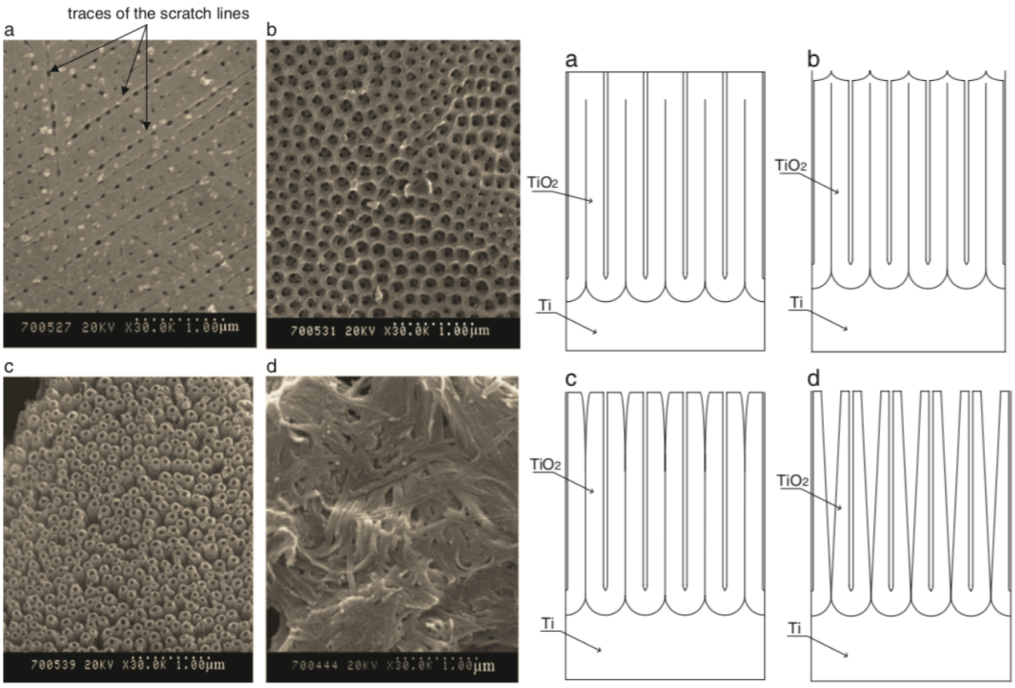

Figure 2.9: SEM images and their schematic view of the etching process during anodization resulting in spaghetti like structure formation. The steps of schematic representation correspond to the porous titania formed at -5 °C (a), 0 °C (b), 20 °C (c,d). Anodic voltages: 100V (a), 90 V (b), 60 V(c,d); current density 10mA/cm^2, anodization time 35 min (a,b,c) and 660 min (d).

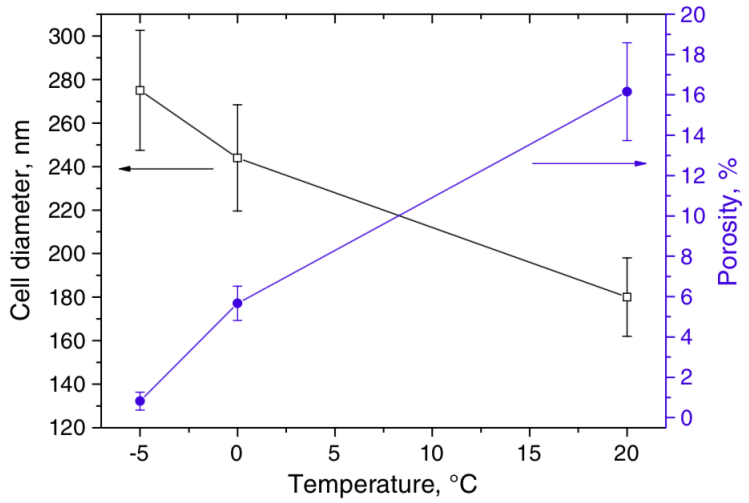

Figure 2.10: The cell diameter and porosity of the titania formed at the anodic current density of 10 mA/cm^2 for 30 min a a function of the electrolyte temperature. The cell diameters depend mainly on the anodic voltage.

The last parameter is the agitation of the electrolyte. Its main effect is the removal of the gas (hydrogen and oxygen) at the anode interphase. The gas acts as an obstacle to the ionic current by increasing the anodic forming voltage and reducing the area where the electrochemical reactions take place. So, if the agitation is enough to spread the gas bubbles far from the metal surface, the total forming voltage is decreased [44].

It has, also, an important effect in the formation of nanotubes in fluoride containing solution, as shown in figure 2.11.

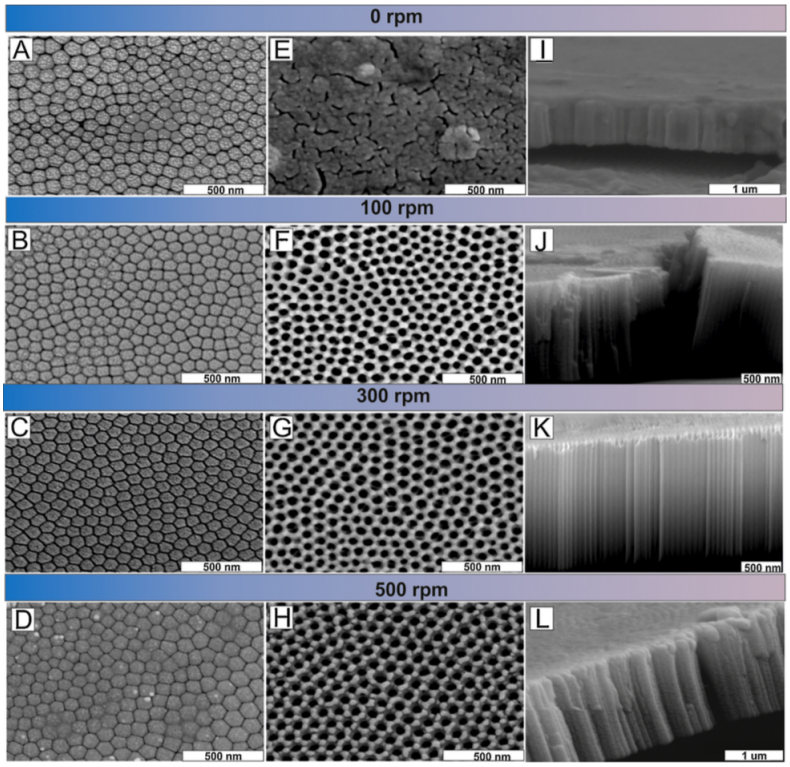

Figure 2.11: SEM bottom views (A-D), top-views (E-H), and cross-sectional views (I-L) of ATO layers formed at 30 V for 10 min at different stirring speeds ranging from 0 to 500 rpm.

An increase in the stirring speed generates an increase in the diffusion of F^- ions which increases the chemical etching rate favouring the formation of nanotubes[53].

Substrate composition

Oxides grow differently on alloys than on pure titanium, as a blend of TiO_2 and alloying elements oxides. For instance, on the most common titanium alloy (Ti6Al4V) oxidation kinetics is generally faster as a result of different electronic properties and crystallinity.
In presence of a mixed oxide short-range order decreases, thus delaying crystallization and reducing conductivity: this, in turn, reduces the extent of parasitic reactions and increases anodizing efficiency [54].

2.3.4 Standard Anodization

The main characteristic of the standard anodizing is that of having the coloring of the metal. Interference colours are generated by thin transparent films, like titanium dioxide amorphous layer, generated by standard anodizing.

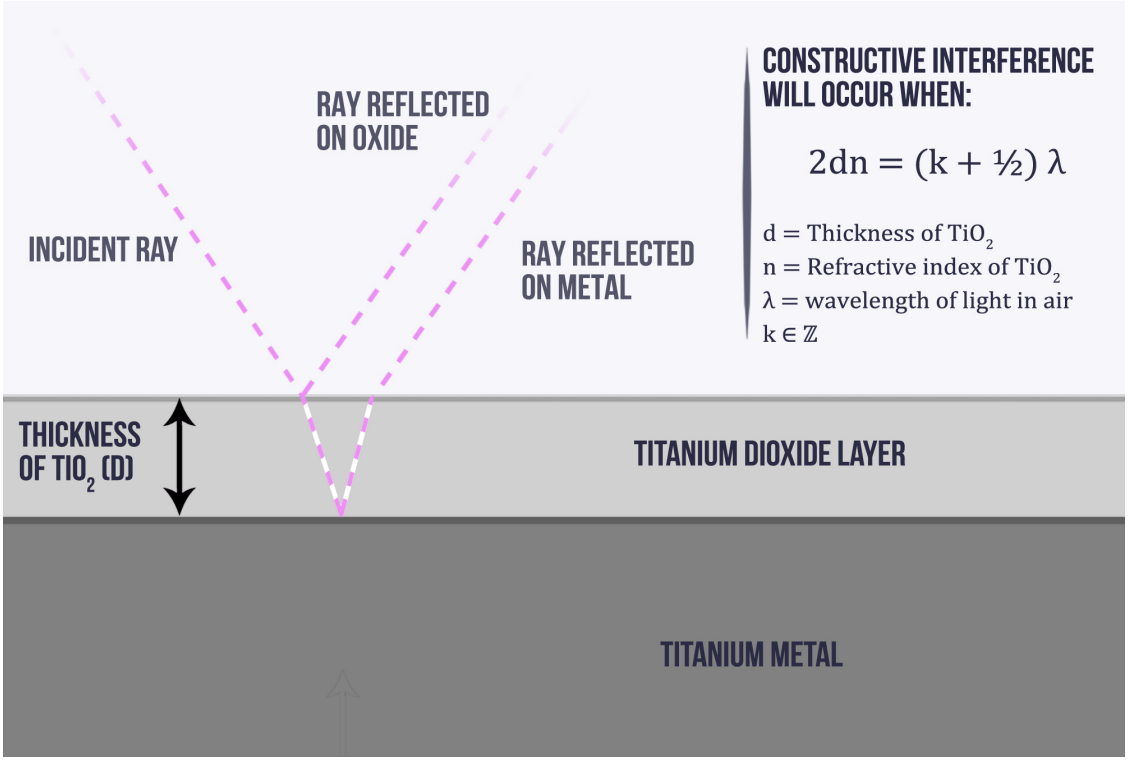

Figure 2.12: oxide interference

The light is reflected only in part by the film, while the leftover is refracted inside the film (figure 2.12).
Since radiation has a periodic nature, colors change with continuity with growing oxide thickness according to Bragg's law interference:

$$n_{TiO_2}\lambda = 2dsin\theta \tag{2.7}$$

where n_{TiO_2} is the refractive index of titanium dioxide, λ is the radiation wavelength giving constructive or destructive interference and θ the angle of incidence of light. Knowing all the parameters, it is possible to obtain the thickness d without complex surface analysis.
Oxide thickness is directly proportional to the feeding voltage; with growing voltage, the chromatic scale that can be achieved consists of the following order of colours: yellow - purple - blue - light blue - silver - yellow - pink - violet - cobalt blue - green - yellow/green - pink - green [55][54]. This process is generally performed with diluted sulfuric and phosphoric acid as electrolyte. In these conditions the growth rate of the oxide is typically close to 2 nm/V. The created film is amorphous and compact, until the voltage is sufficiently high to generate crystalline nucleus (anatase or rutile) in the amorphous matrix, due to the establishment of Plasma Electrolytic Oxidation conditions.
For a feeding voltage ranging from 70 V to 120 V, depending on the substrate, electrolyte and current density, oxides show both interference colours and semicrystalline structure, while for higher voltages Plasma Electrolytic Oxidation deeply affects the whole surface, causing a sharp increase of the oxide thickness and modification of the surface morphology, and the consequence loss of interference conditions [49][44].

2.3.5 Plasma Electrolytic Oxidation

Plasma Electrolytic Oxidation is a surface coating technology that goes beyond anodizing in metal protection. Technically, PEO and standard anodizing share the same root: both treatments oxidize the surface electrochemically to protect the valve metals and their alloys, such as Ti, Al, Mg, Be, Bi, Hf, Nb, Sb, Ta, U, W, and Zr.
PEO is operated at an electrolytic cell voltage exceeding the dielectric breakdown limit by a few hundred volts. Numerous luminescent sparks move across the surface, establish a vapor plasma envelope, and oxidize the surface. In this manner, PEO exploits the arcing phenomenon to grow and consolidate the oxide layer, consequently strengthening its adhesion to the metallic substrate.
Still, the initial period of PEO treatment has to go through standard anodizing to develop the barrier layer until it reaches the point where dielectric breakdowns begin [56].
A theoretical model of breakdown caused by an avalanche of electrons injections at the electrolyte/oxide interface has been proposed from Ikonopisov and co-workers. According to this model, the relationship of the breakdown voltage with electronic current and the electrolyte concentration/composition is represented by the following equations:

$$V_B = a_c + b_c \log c \tag{2.8}$$

$$V_B = a_B + b_B \log \rho \tag{2.9}$$

$$\log J_c = \log a_c - b_c \log \rho \tag{2.10}$$

Where a_c, b_c, a_B, b_B, a_c, and b_c are constant values. In above equations, V_B, C, ρ, and J_c are breakdown voltage, electrolyte concentration, electrolyte resistivity, and the electronic current density at the anode, respectively.
Assuming that the breakdown occurs when the avalanche current (J_0) reaches a particular fraction (Z) of the total anodizing current (J_1), Ikonopisov derived a relation between the mentioned parameters and E (the field), α (the impact ionization coefficient) that is given by:

$$V_B = \frac{v2.303E}{\alpha} \log \frac{vZJ_1}{J_0} \tag{2.11}$$

The model proposed to explain electrical breakdown involves injection of electrons (or electrons in the form of anions) into the film from the electrolyte [57][58].

The layer produced by this technique is porous, rough, corrosion resistant, biocompatible and bioactive [59][60][61].
Plasma temperatures have been estimated via optical spectroscopy to range from about 4000 to 12000 K, with some indications of a higher temperature core and a lower temperature surrounding region. Corresponding electron densities typically range from 10^{15} to 10^{18} cm^{-3}. It is also clear that PEO plasmas commonly contain many species, originating from the substrate, the existing coating and the electrolyte. Of course, detailed results concerning the species present in the plasma, and their concentrations, depend on the compositions of substrate and electrolyte, and also on electrical conditions affecting the creation and nature of the plasma [62].
The high temperatures that are reached locally in the coating allow the formation of a variety of crystalline and amorphous phases. The crystalline phases can give rise

to coatings of high hardness and wear resistance. The mechanism of coating material formation remains the subject of discussion, but it is likely to involve several process, including anodic oxidation, thermal oxidation, thermolysis, and reactions of substrate and electrolyte species within the plasmas generated by the discharges [63].
The sequence events during a single discharge is shown in figure 2.13.

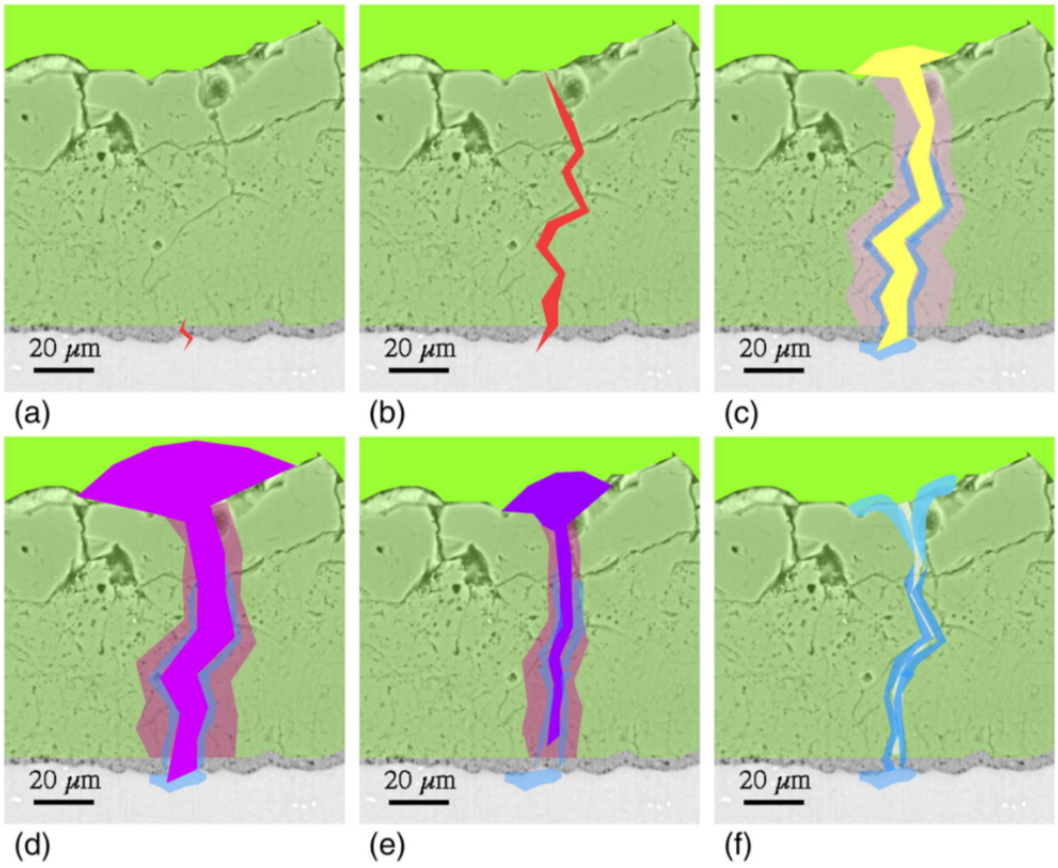

Figure 2.13: Schematic depiction of the sequence events during a single discharge, showing: (a) initial electrical breakdown, (b) development of the plasma channel through the coating thickness, (c) initial bubble growth and formation of oxide in the plasma, (d) bubble expansion and heating of region around discharge, (e) shrinkage and cooling as the plasma resistance rises, causing the current to fall, and (f) final quenching and expulsion of some liquefied oxide from the channel [64].

Micro-discharge characteristics

Typical discharges are now known to occur in prolonged sequences (cascades) at particular locations, and to have lifetimes of the order of a few tens to a few hundreds of microseconds, with "incubation" periods between them of around a few hundred μs to a ms or two. The lifetime of a cascade can apparently be very long (perhaps of the order of a second or more [65]), although in practice during AC processing the discharges normally form only during the anodic part of the cycle, when the voltage is above a certain level, which limits the duration of a continuous sequence to something less than the half-cycle period.
Discharge currents are typically several tens of mA, discharge energies a few mJ and diameters of core discharge channels a few tens of μm [62].

Coating microstructure

Most of the new oxide created during each discharge is formed within the plasma as it cools and collapses. This condenses as liquid, which is then injected into surrounding cavities under high local pressures, with some reaching the free surface, where it tends to erupt into "volcanic craters", before solidification finally occurs, as shown in figure 2.14.

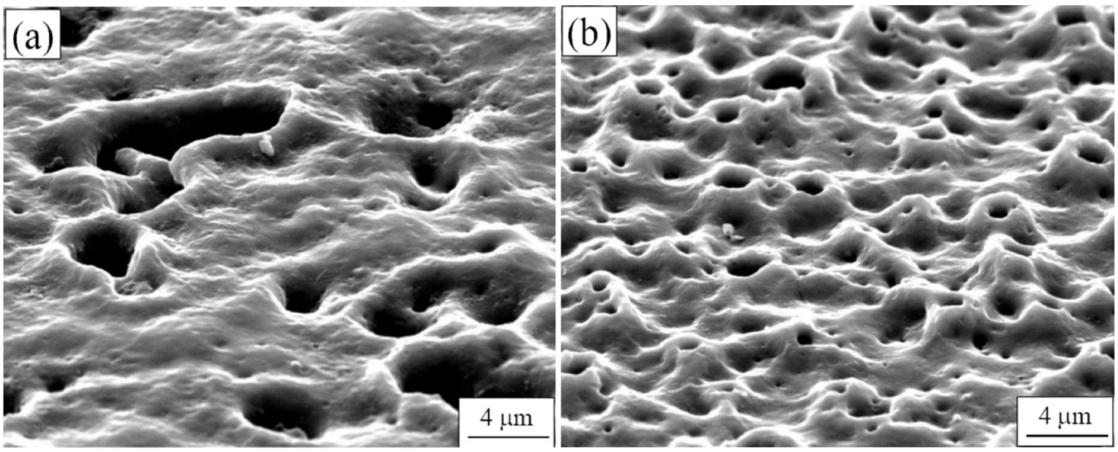

Figure 2.14: Surface structures of the oxide films of CP samples via PEO coating in two different electrolytes [66].

The microstructure of PEO coatings tends to be relatively complex. Local region will have undergone very rapid solidification (quenched by the electrolyte after the most recent discharges), although regions in the immediate vicinity of those discharges may have effectively been heat treated.
In general, however, several features are observed that are characteristic of rapid solidification. These include a very fine grain structure (possibly close to, or actually, amorphous) and the presence of metastable phases.
Most PEO coatings are quite highly porous, with typical overall level usually 10-20% for all substrates, having a complex architecture and covering a wide range of scales. Almost all of the porosity is normally surface-connected.
The high level of porosity is deleterious because it decreases the corrosion resistance and the mechanical properties of the coating. However, it should be appreciated that, on balance, the presence of the porosity is beneficial in many cases like biomedical and photo-catalytic usage of Ti-based PEO coatings [62].

Electrical conditions

Anodizing can be performed with four typical electrical conditions (figure 2.15):

1. **DC Anodizing**: Anodizing has traditionally been performed with a conventional Direct Current (DC) power source due to its simplicity and ease of use. Pure DC can produce anodic film with good optical properties and wear resistance.

2. **AC Anodizing**: A sinusoidal AC wave can also act as power signal for titanium anodizing. The AC current is typically taken directly from the mains (110/230 V, 50/60 Hz) and transformed to the required voltage for anodizing.

3. **AC superimposed DC anodizing**: the signal is basically creating a ripple current on top of the DC current.

4. **Pulse Anodizing**: during pulsed anodizing, in contrast with DC anodizing, current is not supplied continuously. Pulsed anodizing defines all the anodic oxidation carried out with current waveform instersecting the zero. The easiest pulsed waveform is monopolar pulsed current, which alternates on-periods and off-periods. This anodizing regime is described by two parameters: duty cycle and frequency. The first, expressed as percentage, defines the ratio between on-time and total time, while the second defines the pulses frequency.
A positive duty cycle is the working time of positive pulse divided by the total time of the cycle and, to allow this, the istantaneous current density varies in time, with spikes, in correspondence of istantaneous rises and decreases of the potential [44][67].

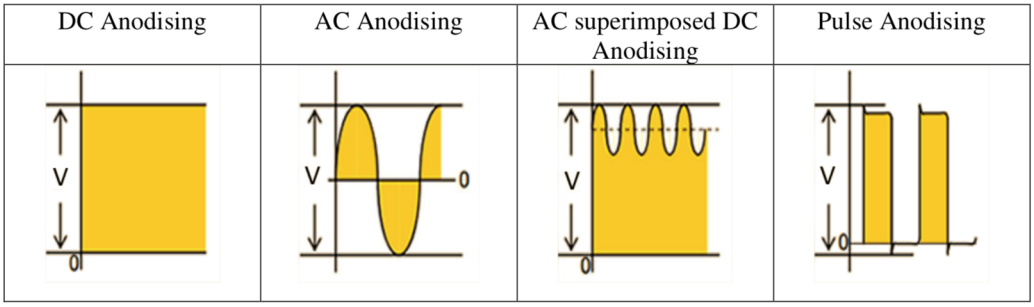

Figure 2.15: Overview of anodizing signals[67].

The current can, not only vary between the positive spike and the zero, but also go negative. This is the case of bipolar pulsed regime.
The bipolar mode has the advantage of two DC power supplies separately controlling positive and negative pulses. In this way it is easy to vary the duty cycle and time off period between the pulses (figure 2.16). From the industrial point of view, this mode of control permits achievement of higher power and frequencies up to several thousand of Hz [44][68].

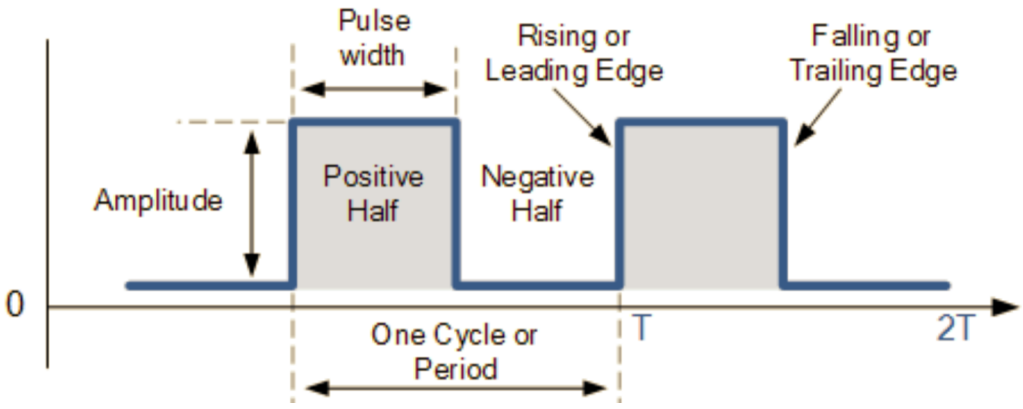

Figure 2.16: Bipolar pulse anodizing[67].

Cathodic discharges and the effect of supply frequency

The cathodic part of the cycle has been increasingly studied recently. It has been clear for some time that PEO coatings produced using AC are in general of superior quality (harder and denser, for example) than those produced under corresponding (anodic) DC conditions. It has also been shown that coating quality is improved if the cathodic voltage is raised [69] or if the ratio of cathodic current to anodic current is raised [70].
What actually happens during the cathodic half-cycle is less clear. It is certainly the case that, at least under most conditions, discharges predominantly occur during the anodic half-cycle, although current does flow in both half-cycles.
In practice, PEO processing is conventionally carried out using AC, with most coatings, both in research work and in technological usage, often being produced at 50 or 60 Hz (although higher frequencies are becoming more popular). The cycle period is thus commonly about 20 ms, which is sufficiently long to allow extended cascades during each (anodic) half-cycle.
There is a considerable interest in how the process changes as the supply frequency is increased, such that the cycle period is no longer large compared with the inter-discharge period, or the discharge period itself. There are several reports [71][72][73] showing that an increase in the supply frequency (with maximum values usually around 1-1.5 kHz) leads to a reduction in coating growth rates as shown in figure 2.17

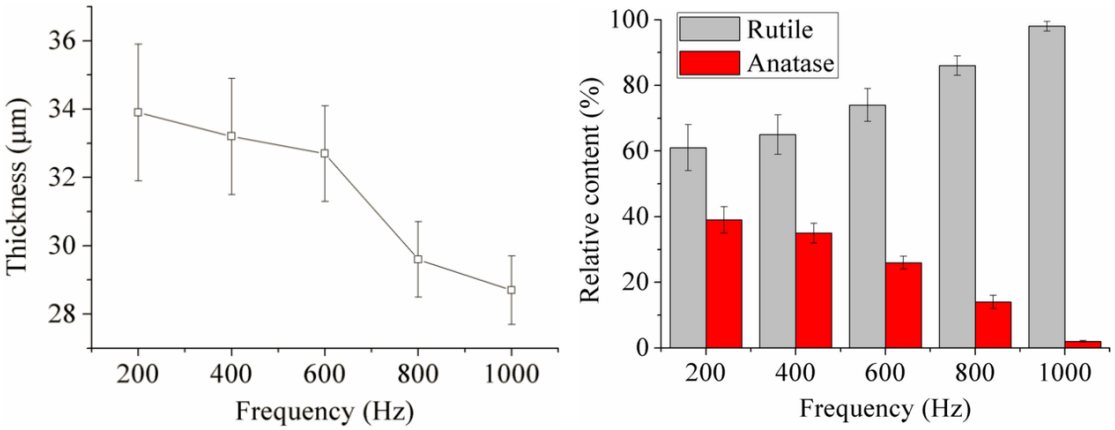

Figure 2.17: Variation with frequencies of: coating thickness (left) and relative contents of anatase and rutile TiO_2 (right) of CP Ti specimens after PEO treatment [72].

Other reports [74][75][76] show, however, different effects on the thickness and composition of layer (figure 2.18).

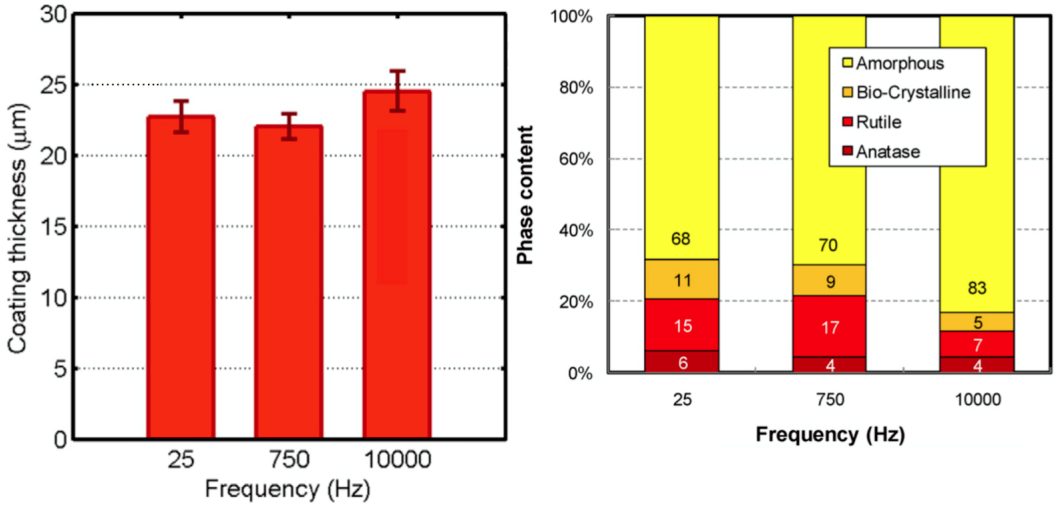

Figure 2.18: Variation with frequencies of: coating thickness (left) and coating microstructure (right) of CP Ti specimens after PEO treatment [76].

As with many aspect of PEO, there is a considerable complexity and scope for extraneous factors (electrolyte, temperature, pH, voltage etc...) to exert an influence.

"Soft Plasma" PEO conditions

Over recent years, increasing attention has been paid to the so-called soft-sparking or soft regime during PEO. Normally, as the thickness of a PEO coating increases, the through-thickness electrical discharges become more intense and longer-lived. This often places an upper limit on the thickness of PEO coatings, since intense discharges start to destroy the coating. However, under certain conditions, termed the soft regime, it appears that this can be avoided and coating microstructures can be improved.
In such cases, the process starts conventionally, but, once a certain coating thickness or processing time has been reached, a reduction is observed in the applied potential (under constant current conditions) and the discharges become almost invisible (altough coating growth continues).
This "soft" regime was first studied by Jaspard-Mécuson et al. [77], who asserted that the ratio of anodic to cathodic charge (termed the charge ratio, R) must be less than unity for the transition to occur for Al. Additionally, the transition to the soft regime apparently occurs sooner for higher current densities and higher AC supply frequencies [74].
Soft regimes of Mg and Ti do not seem to follow the same criteria specified for aluminum; they depend on the coating constituents as well. Even if the phenomenological criteria are met satisfactorily, the operation may not produce the desired microstructure [56].

2.3.6 Nanotubes production

Titanium oxide is a useful catalytic and gas-sensing material. Titanium oxide thin films with nanoporous structures are desirable for these applications due to their large surface areas and high reactivities.
The anodizing approach is able to build a porous titanium oxide film of controllable

pore size, good uniformity, and conformability over large areas at low cost [78]. Nanoporous and tubular titania layers are formed by applying an anodizing current using fluoride containing electrolytes. The titania layers develop perperndicular to the metal substrate which can be self-organized under controlled conditions. Titanium and titanium dioxide are readily dissolved in fluoride based electrolytes, particularly those containing hydrofluoric acid. There is a constant dissolution rate of the anodic layer at the base of each pore. In a fluoride containing electrolyte the oxide dissolves leading to the formation of a titanium hexafluoride complex (TiF_6^{2-}), which is stable in water. The applied electric field may also weaken the bond between Ti and O in the oxide, effectively facilitating chemical dissolution of TiO_2. There has been significant progress made regarding their synthesis, which has led to:

1. a 1st generation of NTs (figure 2.19 [a]) prepared in hydrofluoric acid which were only 0.5 μm long,
2. a 2nd generation of NTs (figure 2.19 [b]) up to 5 μm long grown in water based electrolytes containing fluorine salts,
3. a 3rd generation of smooth NTs (figure 2.19 [c]) (i.e. no ribs on the tube sides, unlike the 1st and the 2nd generations) and longer NTs up to 100-1000 μm grown in organic electrolytes containing fluoride ions,
4. a 4th generation (figure 2.19 [d]) which is similar to the 3rd one but the NTs are highly self-organized

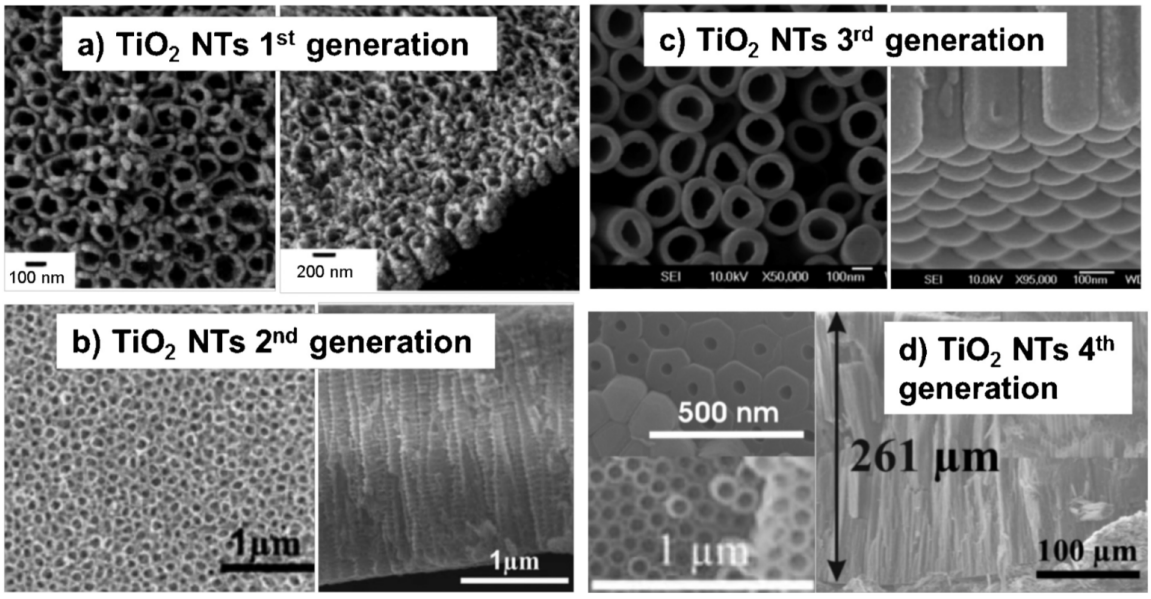

Figure 2.19: Evolution of the self-organization (and length) of anodized TiO_2 NTs: (a) 1st generation [78], (b) 2nd generation [79], (c) 3rd generation [80], (d) 4th generation [81].

Growth mechanism

The current-time transient allows the different stages of anodic film growth to be monitored. For barrier layer type oxides the current density simply decays as the

anodic layer thickens, however, for a porous oxide layer three different stages can be identified as described in figure 2.20 which illustrate the transient observed for TiO_2 NTs grown in aqueous and organic based electrolytes, respectively.

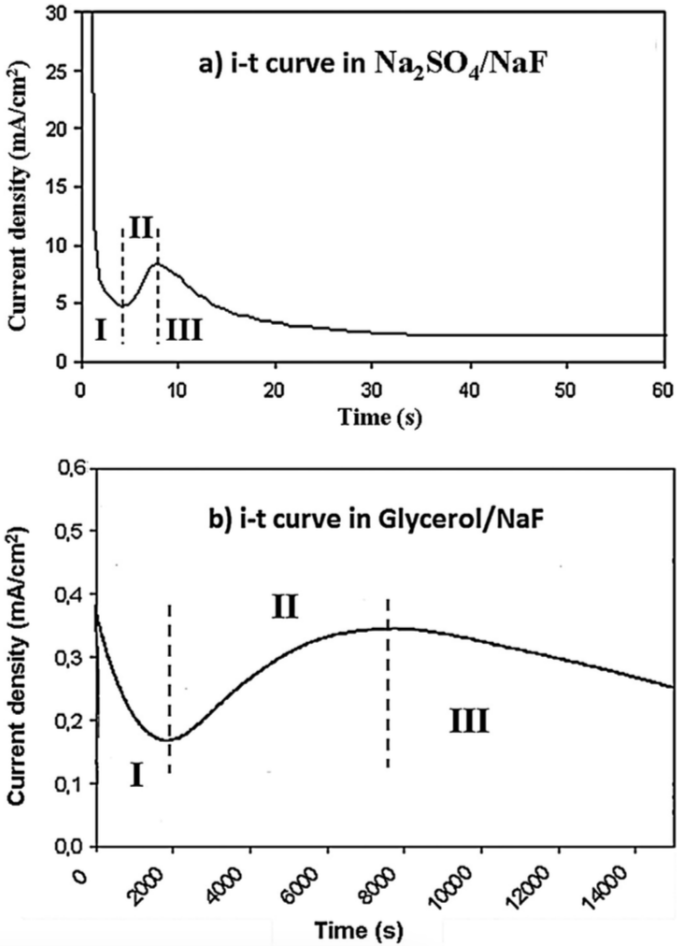

Figure 2.20: Current-time transient registered for a sample anodized in: (a) a NaF/H_2O electrolyte at 20 V [82] and (b) during the anodization of titanium at different potentials in glycerol/NaF [83].

At *stage 1* the anodizing process begins and the current quickly decreases to a minimum value due to the formation of a high resistance oxide barrier layer, which grows up to 50 nm thick at 20-25 V. In order to maintain the oxidation process, ions (O^{2-}, OH^-, Ti^{4+}, F^-) must move through the high resistance barrier layer and at this stage porosity is induced by the presence of F^-.
The current subsequently rises to a maximum (*stage 2*) as pore nucleation progresses. this is due to a decrease in the resistance of the anodic film as more paths are available for ionic species in the electrolyte. From a flow model perspective, this stage represents the transition from a relatively thin anodic film where upward displacement of the oxide does not occur to the beginning of the formation of a porous/tubular structure were the visco-plastic oxide is continually being pushed upwards to minimize stress at the metal/metal oxide interface.
Finally the current attains a constant value or drops (*stage 3*) when a steady state is reached during the formation of TiO_2 NTs. The classical interpretation of stage 3, based on the field-assisted oxidation and dissolution model would be that the steady state is reached because the rate of oxide formation at the metal/oxide interface and

the rate of dissolution at the oxide/electrolyte interface are equal [84].

Chapter 3

Coating Analysis

3.1 Immersion test

Immersion tests measure the progress of corrosion damage obtained from the immersion length within a corrosive environment, as well as other factors that can accelerate the corrosion process.
These tests can involve alternative drying or immersions, such as in cases of cyclical tests. Moreover, test instrumentations may be included throughout immersion like electrochemical instrumentation connections in order to facilitate the measurements (figure 3.1).

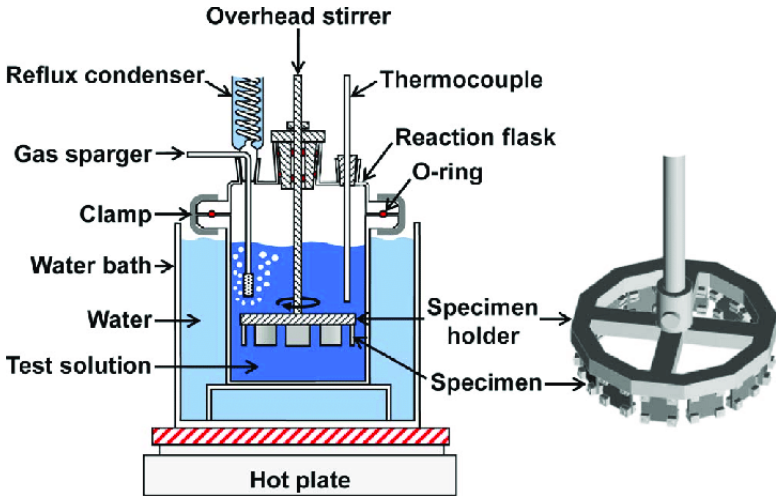

Figure 3.1: Immersion test

Immersion tests are capable of generating uniform data for alloy corrosion and are utilized in industries subjected to immersion conditions.
Environmental conditions that should be created and the acceleration degree needed usually identify which laboratory tests should be used. Proper acceleration is obtained by the following:

- Prolonging the exposure to vital conditions which are believed to lead to corrosion damage. For instance, if a certain vessel is to undergo batch processing with a chemical for 24 hours, the corrosion exposure in the laboratory should be 240 hours.

- Making the conditions more intense in order to boost corrosion rates. This can be achieved by increasing one or more of the following: pressure, salt concentration, temperature or solution acidity.

When the conditions for the environment have been identified and the test has been created, this should be conducted again several times to verify whether this test meets the acceptable reproducibility standard.
Generally, immersion tests can be separated into these categories:

- Alternate immersion test - This immersion test involves a cyclic procedure that involves a specimen being immersed for a certain period of time. Then, the specimen is removed and undergoes drying prior to re-submerging to the cycle. Typically, about a hundred cycles are completed throughout the test.

- Simple immersion test - In this test, small batches of the material are subjected to the medium under testing, while loss of weight is being gaged for a particular period.

The immersion test remains the most reliable method in terms of screening. It also serves as the most simple and economical way to determine the most suitable material to protect against corrosion in certain environments [85].

3.2 Potentiodynamic scan

Potentiodynamic polarization is often used for laboratory corrosion testing. It can provide significant useful information regarding corrosion mechanisms, corrosion rate and susceptibility of specific materials to corrosion in designated environments [86]. In a potentiodynamic experiment, the driving force (i.e., the potential) for anodic or cathodic reactions (depending on the nature of the scan) is controlled, and the net change in the reaction rate (i.e., current) is observed. The potentiostat measures the current which must be applied to the system in order to achieve the desired increase in voltage, known as the applied current. Corrosion is a process consisting of two different half-reactions: oxidation and reduction. At the equilibrium potential (also called open circuit potential) the oxidation rate is equal to the reduction rate, so the total anodic current is equal to the total cathodic current (i_a=i_c) and the measured or applied current will be zero (i=0).

3.2.1 Anodic scan

A schematic anodic polarization curve is illustrated in figure 3.2. As can be seen in the figure, the scan starts from point 1 and progresses in the positive (potential) direction until termination at point 2. There are a number of notable features on the curve. The open circuit or rest potential is located at point A. At this potential the sum of the anodic and cathodic reaction rates on the electrode surface is zero. As a result, the measured current will be close to zero. This is due to the fact that the potentiostat only measures the current which it must apply to achieve the desired level of polarization. As the potential increases, we move into region B, which is the active region. In this region, metal oxidation is the dominant reaction taking place. Point C is known as the passivation potential, and as the applied potential increases

above this value the current density is seen to decrease with increasing potential (region D) until a low, passive current density is achieved (Passive region - Region E). Once the potential reached a sufficiently positive value (Point F, sometimes termed the breakaway potential) the applied current rapidly increases (region G). This increase may be due to a number of phenomena, depending on the alloy/environment combination. For some systems (e.g., aluminum alloys in salt water) this sudden increase in current may be pitting (localized breakdown of passivity), while for others it may be transpassive dissolution. For some alloys, typically those with a very protective oxide, such as cobalt, the sudden increase in current is due to oxygen evolution.

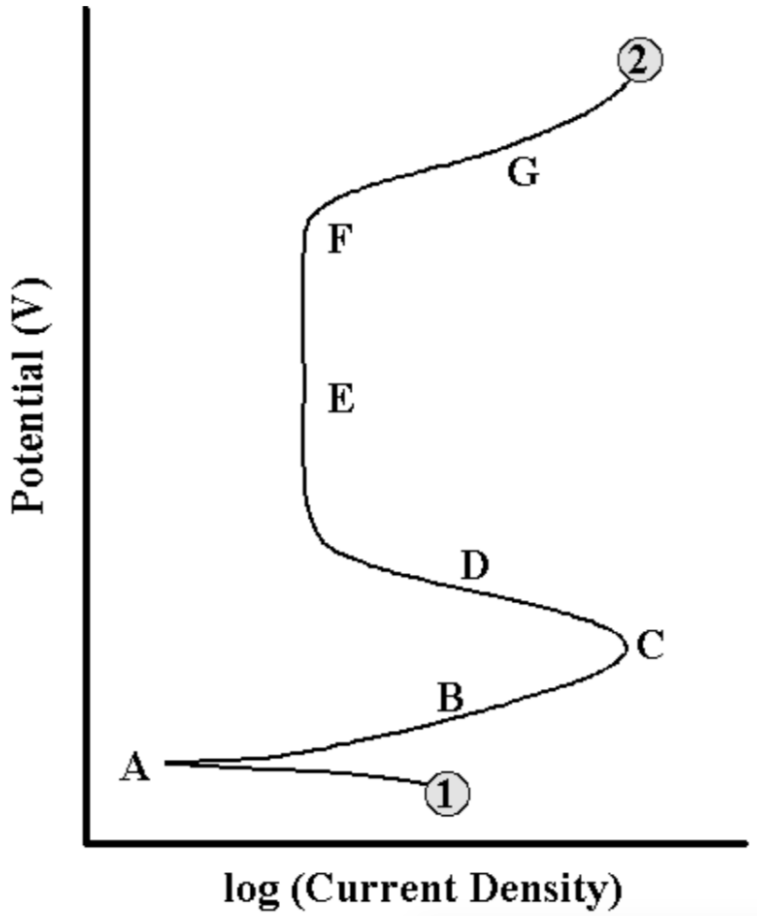

Figure 3.2: Theoretical anodic polarization scan

Depending on the nature of a particular system, some or all of these features may be present [87].

3.2.2 Cathodic scan

A schematic cathodic polarization scan is illustrated in figure 3.3. In a cathodic potentiodynamic scan, the potential is varied from point 1 in the negative direction to point 2. The open circuit potential is located at point A. As with the anodic scan, the open circuit potential represents the potential at which the sum of the anodic and cathodic reactions occurring on the electrode surface is zero. Depending on the pH and dissolved oxygen concentration in the solution, region B may

represent the oxygen reduction reaction. As the potential decreases, the current is initially limited by the frictions (overvoltage) that the charges undergo in the metal-electrode/electrolyte passage. Since the oxygen reduction reaction is limited by how fast oxygen may diffuse in solution (mass transport controlled) there will be an upper limit on the rate of this reaction, known as the limiting current density. Further decreases in the applied potential result in no change in the reaction rate, and hence the measured current (Region C). Eventually, the applied potential becomes sufficiently negative for another cathodic reaction to become operative (i.e., there is a sufficient thermodynamic driving force for an additional cathodic reaction to begin taking place), such as illustrated at Point D. As the potential, and hence driving force, becomes increasingly large, this reaction may become dominant, as illustrated in Region E. This additional reaction is typically the reduction of other species in the environment (such as the hydrogen evolution reaction, also known as the water reduction reaction). An increase in current may also be observed if sufficient driving force exists to reduce the oxide present on the electrode surface [87].

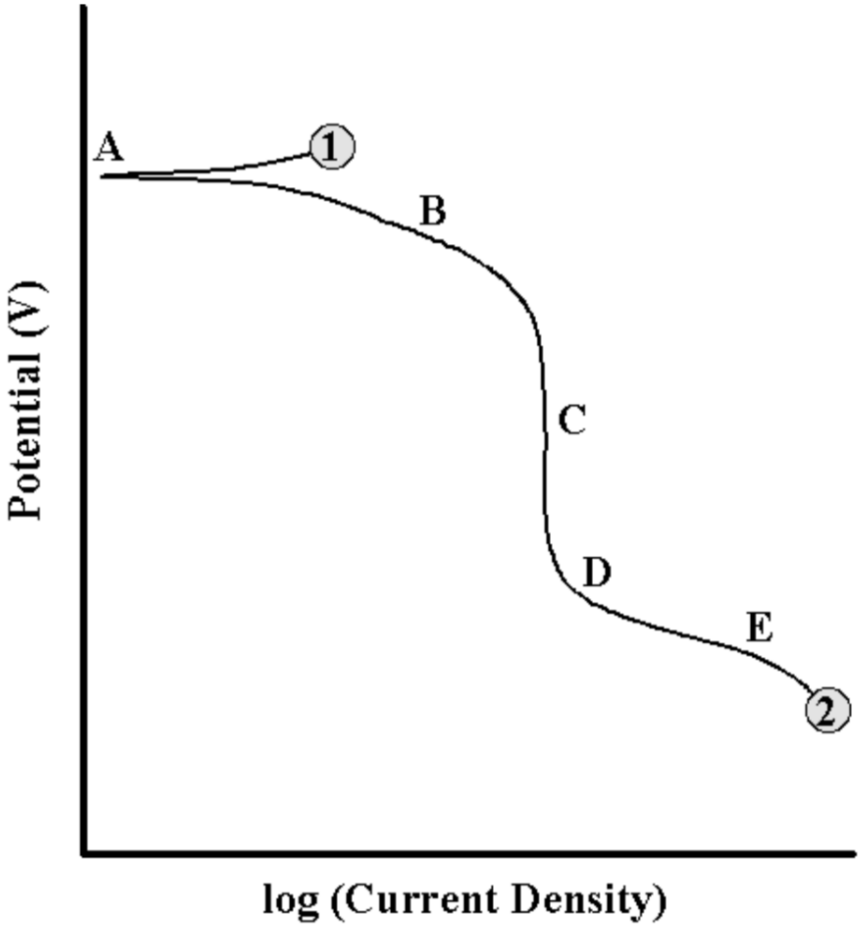

Figure 3.3: Theoretical cathodic polarization scan

3.3 EIS

Electrochemical Impedance Spectroscopy (EIS) is a frequency domain measurement made by applying a sinusoidal perturbation, often a voltage, to a system. The impedance at a given frequency is related to processes occurring at timescales of the

inverse frequency.
Although many other electrochemical measurements focus on driving a system far from equilibrium with potential sweeps or steps, such as cyclic voltammetry or chronoamperometry, EIS uses small perturbations. These small departures from equilibrium are assumed to have a linear response, thus greatly simplifying the frequency analysis.
Practically speaking, EIS is performed by sweeping through a wide range of frequencies at a single perturbation amplitude. As instrumentation has improved over the last several decades, frequencies ranging from 10^{-4} to 10^{8} Hz are attainable, thus allowing for the study of both fast kinetic and slow transport process.
In experimental situations the eletrochemical impedance is normally measured using excitation AC voltage signal V with small amplitude V_A (expressed in volts) applied at frequency f (expressed in Hz). The voltage signal V (t), expressed as a function of time t, has the form:

$$V(t) = V_A sin(2\pi ft) = V_A sin(\omega t) \tag{3.1}$$

In this notation a "radial frequency" ω of the applied voltage signal parameter is introduced.
In a linear or pseudolinear system, the current response to a sinusoidal voltage input will be a sinusoid at the same frequency but "shifted in phase" that is determined by the ratio of capacitive and resistive components of the output current (figure 3.4).

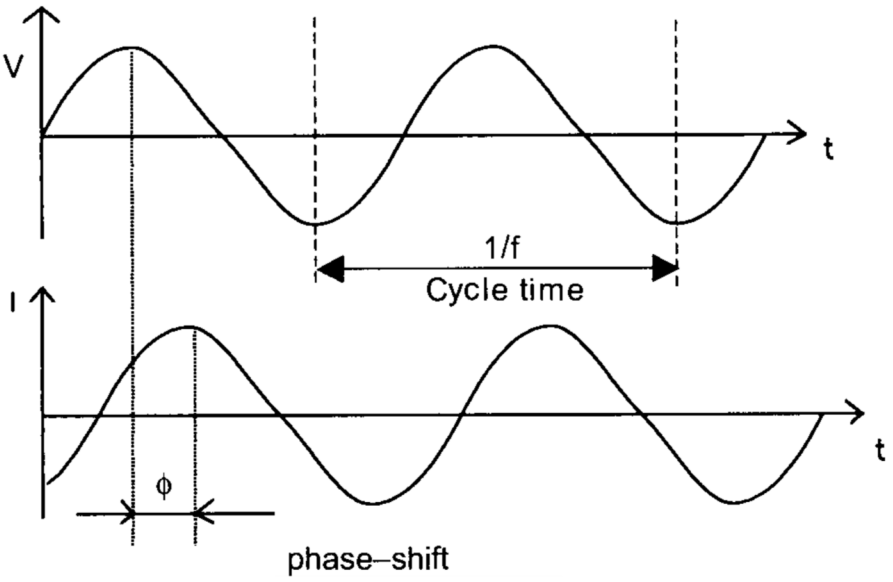

Figure 3.4: Impedance experiment: sinusoidal voltage input V at a single frequency f and current response I

In a linear system, the response current signal I(t) is shifted in phase (Φ) and has a different amplitude, I_A:

$$I(t) = I_A sin(\omega t + \Phi) \tag{3.2}$$

An expression analogous to Ohm's Law allows to calculate the complex impedance of the system as the ratio of input voltage V(t) and output measured current I(t):

$$Z* = \frac{V(t)}{I(t)} = \frac{V_A sin(\omega t)}{I_A sin(wt + \Phi)} = Z_A \frac{sin(\omega t)}{sin(\omega t + \Phi)} \tag{3.3}$$

The impedance is therefore expressed in terms of a magnitude (absolute value), Z_A=—Z—. and a phase shift, Φ. If we plot the applied sinusoidal voltage signal on the x-axis of a graph and the sinusoidal response signal I(t) on the y-axis, an oval known as a "Lissajous figure" will appear (figure 3.5-A).

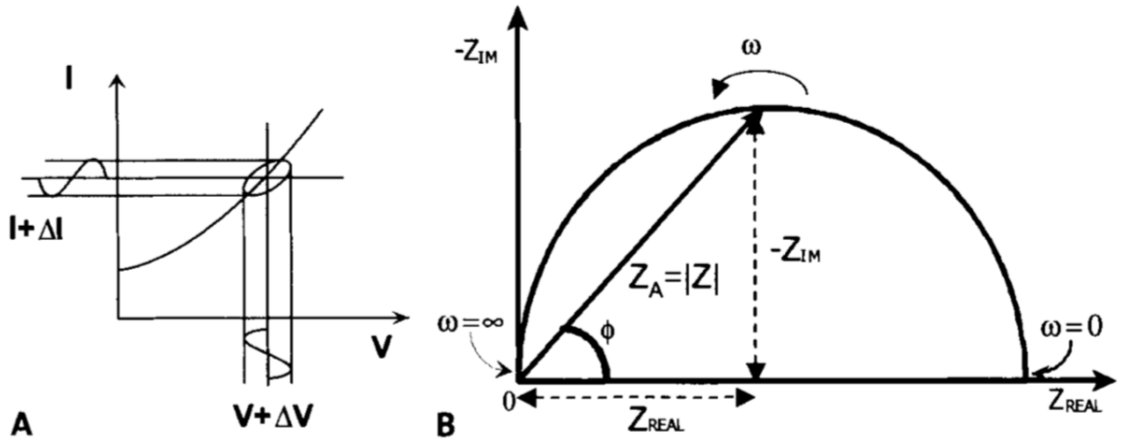

Figure 3.5: Impedance data representation: A. Lissajous figure; B. Complex impedance plot

Analysis of Lissajous figures on oscilloscope screens was the accepted method of impedance measurement prior to the availability of lock-in amplifiers and frequency response analyzers. Modern equipment allows automation in applying the voltage input with variable frequencies and collecting the output impedance (and current) response as the frequency is scanned from very high (MHz-GHz) values where timescale of the signal is in micro- and nano-seconds to very low frequencies (μHz) with timescales of the order of hours.
Using Euler's relathionship:

$$exp(j\Phi) = cos(\Phi) + jsin(\Phi) \tag{3.4}$$

It is possible to express the impedance as a complex function. The potential V(t) is described as:

$$V(t) = V_A \exp j\omega t \tag{3.5}$$

and the current response as:

$$I(t) = I_A \exp j\omega t - j\Phi \tag{3.6}$$

The impedance is then represented as a complex number that can also be expressed in complex mathematics as a combination of "real", or in-phase (Z_{REAL}), and "imaginary", or out-of-phase (Z_{IM}), parts (figure 3.5-B):

$$Z* = \frac{V}{I} = Z_A \exp j\Phi = Z_A(cos\Phi + jsin\Phi) = Z_{REAL} + jZ_{IM} \tag{3.7}$$

and the phase angle Φ at a chosen radial frequency ω is a ratio of the imaginary and real impedance components:

$$tan\Phi = \frac{Z_{IM}}{Z_{REAL}} \tag{3.8}$$

3.3.1 Graphical Representation of Impedance Spectroscopy Data

If a sinusoidal voltage is applied to a pure resistor of value R, then the measured complex impedance is entirely resistive at all frequencies as $Z^* = R$ and the impedance magnitude $|Z| = R$. If a sinusoidal voltage is applied across a pure capacitor, the measured impedance can be calculated according to the relationship $Z^* = -j(\omega C)^{-1}$ where C is the capacitance. The magnitude of the impedance for a pure capacitor is $|Z| = (\omega C)^{-1}$. This impedance depends on the frequency and is entirely capacitive. Many real-life systems cannot be represented by an ideal resistor or capacitor but rather by a circuit that combines resisitve and capacitive elements.
One typical circuit is the R—C circuit, represented by a parallel combination of an ideal resistor R=10000 ohm and an ideal capacitor C=1 μF (figure 3.6-A).

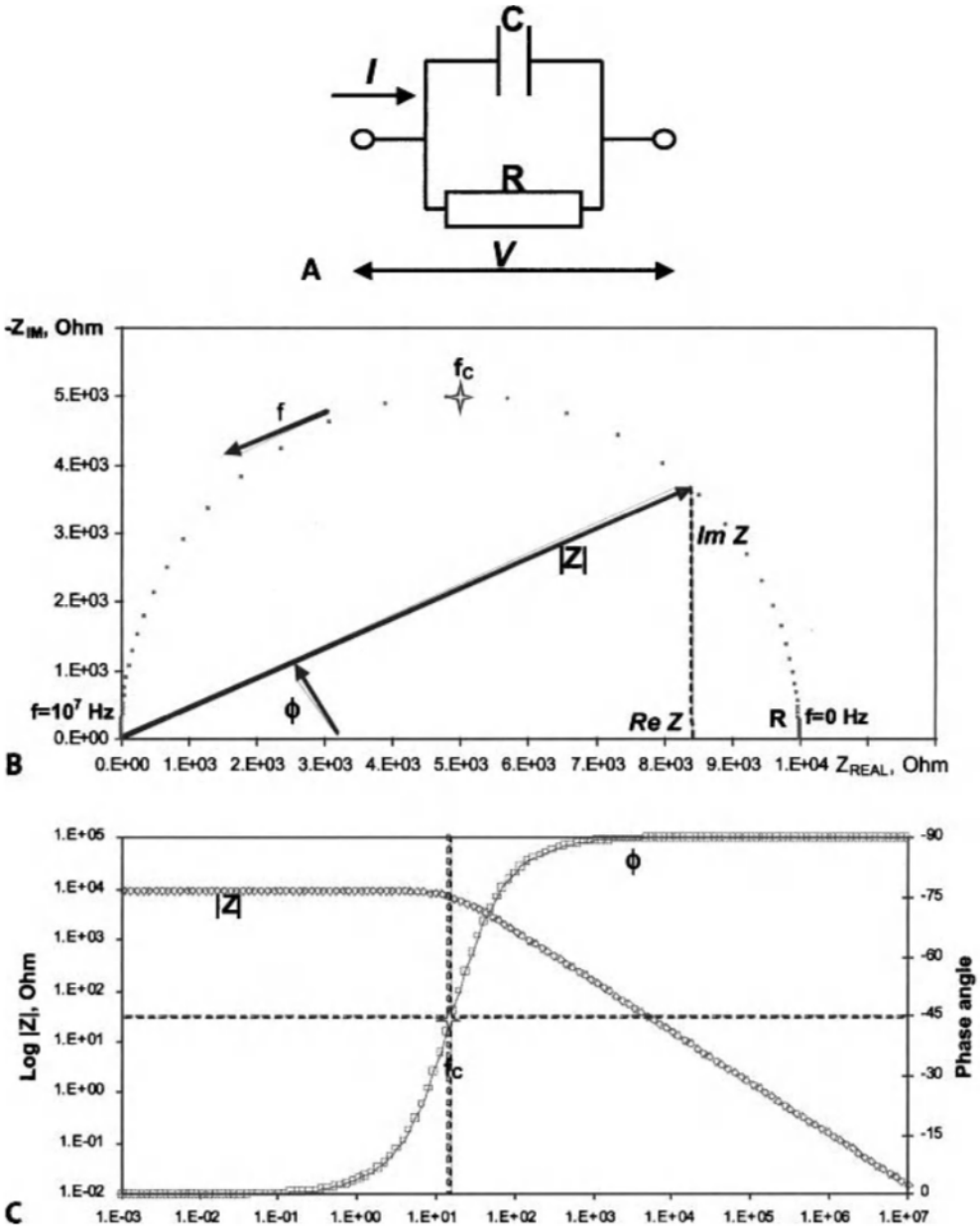

Figure 3.6: A. Equivalent circuit; B. Nyquist; C. Bode plots with impedance for the R—C circuit.

The impedance of the two parallel branches of this circuit are equal to a constant resistance R and $-j(\omega C)^{-1}$, respectively. According to Kirchoff's Law for a parrallel circuit, the potentials across both circuit elements are equal, while the total current can be calculated from the sum of the currents flowing through the resistor and capacitor branches:

$$I(t) = \frac{V(t)}{Z^*} = \frac{V(t)}{R} - \frac{\omega C V(t)}{j} = V(t)[\frac{1}{R} - \frac{\omega C}{j}] = V(t)\frac{1 + (\omega RC)^2}{R - j\omega R^2 C} \tag{3.9}$$

The expression for the resulting impedance $Z^* = \frac{R}{1+(\omega RC)^2} - j\frac{\omega R^2 C}{1+(\omega RC)^2}$ is composed of "real" and "imaginary" parts. If the real part Z_{REAL} is plotted on the x-axis and the imaginary part Z_{IM} on the y-axis of a chart, a so called "Nyquist plot", or complex plane impedance diagram, is revealed. As shown in figure 3.6-B, this plot has the shape of a semicircle. On the Nyquist plot the impedance can be represented as a vector of length —Z—. The angle between this vector and the x-axis is Φ, or "phase-angle" which also has a negative notation, as (from eq. 3.8):

$$\Phi = \arctan(\frac{Z_{IM}}{Z_{REAL}}) \tag{3.10}$$

There is a parameter $\tau = RC$ called "time constant", which is associated with this circuit, and a corresponding "characteristic circular" frequency $\omega_C = \frac{1}{\tau}$ and "characteristic" or "critical relaxation" frequency $f_C = \frac{1}{2\phi\tau} = \frac{1}{2\phi RC} = 15.9$ Hz. At very high frequencies the impedance is completely resistive and approaches the value of R_s, which is the system resistance. The phase angle Φ tends towards -90° at high frequency and towards 0° at low frequency, and critical frequancy f_C corresponds to a midpoint transition where the phase angle is -45° and $Z_{IM} = Z_{REAL} = \frac{R}{2}$.
For current passing through a circuit composed of a parallel combination of capacitance and resistance, the impedance magnitude of the capacitive segment of the circuit is dependent on the inverse of the AC frequency ω, while the impedance of the resistor is frequency-independent. Therefore, if within the frequency range of the analysis the contribution of the impedances in the resistive and capacitive segments of the circuit are comparable, than at frequencies higher than f_C the capacitive portion of the circuit, with an impedance that is inversely proportional to the large AC frequency value, presents a "path of least impedance" to the current. The measured impedance becomes increasingly capacitive with absolute values greater than the phase angle. At AC frequencies lower than f_C the reverse becomes true: the capacitive portion of the circuit will have high impedance values as they become inversely proportional to low values of the AC frequency. Through the constant resistor the current starts flowing predominantly, and the measured total impedance becomes resistive with the phase angle approaches 0°.
From this simple example it is possible to understand an important feature of this technique. However, if within the analyzed frequency range either the capacitive or resistive impedance component is consistently significantly smaller that the other (in the ratio of 1:100), then the other (larger) impedance component of the circuit consistently presents a relatively very high impedance to the passing current. Therefore, as the current always bypasses the high impedance component, its contribution to the total measured impedance of the system is not measured, and the high impedance component becomes undetectable by the impedance analysis.
Nyquist plots have proven to be very useful in estimating impedance parameters.

The impedance spectra often appear as single or multiple arcs in the complex plane. Thanks to the fact that the shape of the plot yields insight into possible conduction mechanisms or kinetic governing phenomena, Nyquist plots are very used. For example, if the plot displays a perfect semicircle (figure 3.6-B), the impedance response corresponds to a single activation-energy-controlled (or charge-transfer) process. A depressed semicircle indicates that a more detailed model is required, and multiple loops indicate that more than one time constant is required to describe a process. Often, within the frequency range of analysis, only a portion of one or more semicircles is seen.
However, the information the Nyquist plot presents is not complete, since there is typically no detailed indication of the frequency at which the impedance is measured for every point.
For a detailed presentation of the experimental data, the points in the Nyquist plot must be labeled with the corresponding frequency values. The Nyquist plot also makes determination of low impedance values (typically observed at very high frequencies) very difficult.
Another form of data presentation method is the "Bode" plot. It shows a plot of the phase angle and the logarithm of the impedance magnitude as a function of the logarithm of frequency. The Bode plot for the electric circuit of figure 3.6-A is shown in figure 3.6-C. The Bode plot explicitly shows frequency information and reveals an important low impedance behavior seen at high frequencies, unlike the Nyquist plot. The slope of transition between low-frequency and high-frequency asymptotes can provide useful information concerning the nature of the impedance response if characteristic time constants are well separated. The popularity of the Bode plot representation is based on its utility in circuit analysis. Phase-angle plots are sensitive to system parameters and therefore provide a good means of comparing the model to the experimental results.
However, for more complicated electrochemical systems exhibiting additional impedance components, the Bode plot often makes it difficult to estimate characteristic frequencies [88][89].

3.3.2 Circuit Elements

Equivalent circuits (EC) should always be selected on the basis of an intuitive understanding of the electrochemical system, as long as they are based on the chemical and physical properties of the system and do not contain arbitrarily chosen circuit elements. When creating a circuit, it is necessary to understand what type of structure is going to be analyzed and imagine a circuit that can represent it as best as possible. If the data are not fitted, a change, which have a physical sense, in the circuit can be made. It does not make any sense to do the opposite: create a circuit that perfectly fits the data but without any physical meaning. One needs to apply knowledge of the physical processes involved, compare models with experimental data, and attempt to simplify the representation as much as possible.
Most of the circuit elements in the model are common electrical elements such as resistor, capacitors, and inductors. As an example, many models contain a resistor that models the cell's solution resistance R_{SOL}. A list of ideal circuit elements used in the models is provided in table 3.1 [89].

Table 3.1: Ideal Circuit Elements Used in the Models

Component	Equivalent Element	Current vs. Voltage	Impedance
Resistor	R [ohm]	$V = IR$	R
Capacitor	C [F, or ohm^{-1} s]	$I = C\,dV/dt$	$1/j\omega C$
Inductor	L [H, or ohm s]	$V = L\,di/dt$	$j\omega L$
Infinite diffusion	Z_w [ohm]		$R_w/\sqrt{j\omega}$
Finite diffusion	Z_o [ohm]		$R_D \tanh(\sqrt{(j\omega L_D^2)/D})/\sqrt{(j\omega L_D^2/D)}$ $R_D \coth(\sqrt{(j\omega L_D^2)/D})/\sqrt{(j\omega L_D^2/D)}$
Constant phase element - CPE	Q [ohm^{-1} s$^{\alpha}$]		$\frac{1}{Q(j\omega)^{\alpha}}$

3.3.3 Circuit for titanium oxide

Past studies [90], [91], [92], [93], [94], [95], [96], [97], [98], [99], [100], [101] have revealed two electrical circuits used in EIS results interpretation. The first one proposed is shown in figure 3.7.

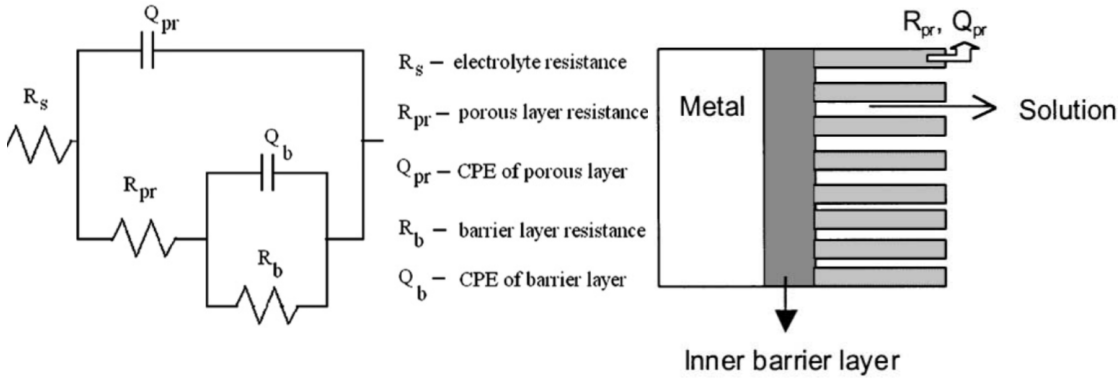

Figure 3.7: Equivalent circuit used in EIS results interpretation[90].

The structure of the inner barrier layer is similar for most anodizing conditions while the external porous layer varies according to various factors, such as, the voltage and the solution used during anodizing (figure 3.8).

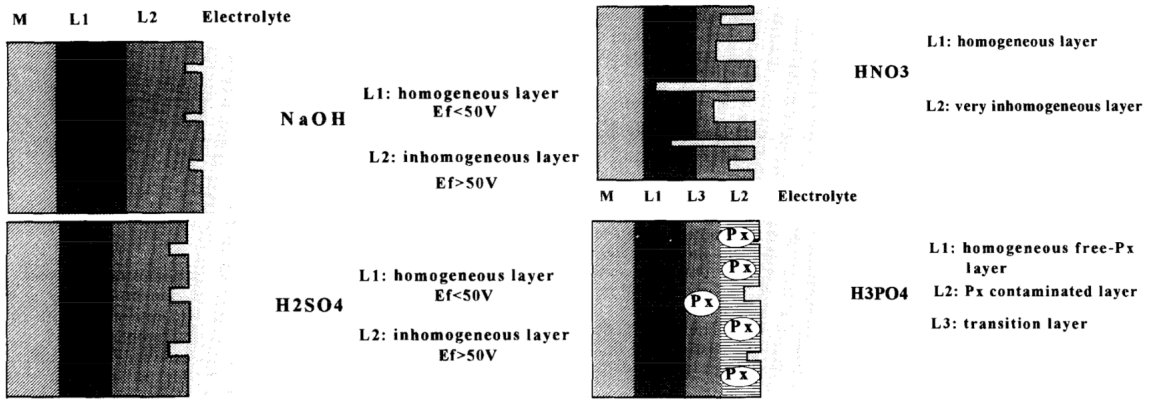

Figure 3.8: Schematical models for the oxides grown in the different electrolytes. M=metal, Li=oxide layer, Px=phosphorous containing species[93].

The second equivalent circuit is shown in figure 3.9 in which R_f and Q_f correspond to the film resistance and capacitance, respectively, R_{ct} and Q_{dl} correspond to the charge transfer resistance and the double layer capacitance. In both circuit, constant phase element (CPE) were employed to represent capacitance elements instead of pure capacitors to take into account any deviation from ideality that could be observed in the capacitive response of the systems [91].

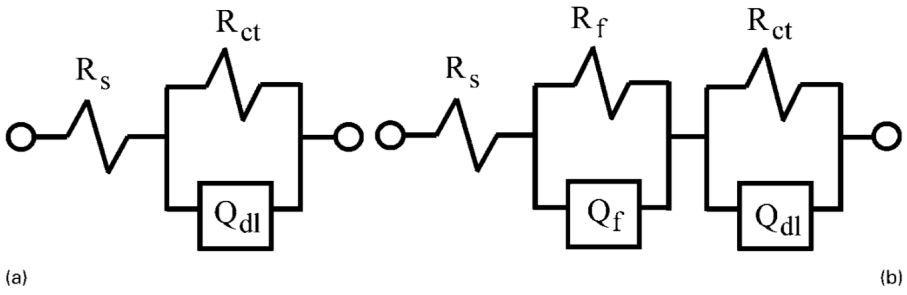

Figure 3.9: Equivalent circuit used to fit EIS experimental data for (a) non-anodised titanium and (b) anodised titanium [91].

Alves et al. [97] proposed another type of circuit for anodized titanium in addition to the classic,commonly used, circuit (figure 3.10). It describe a coating made by a barrier layer and a porous layer with a double porosity: the first is the "classical porosity" typical of anodized titanium while the second is a surface porosity. For this reason a parallel with a RC is added and contain a resistance of the solution in the surface pores and a CPE for the capacitance of the porous structure under it.

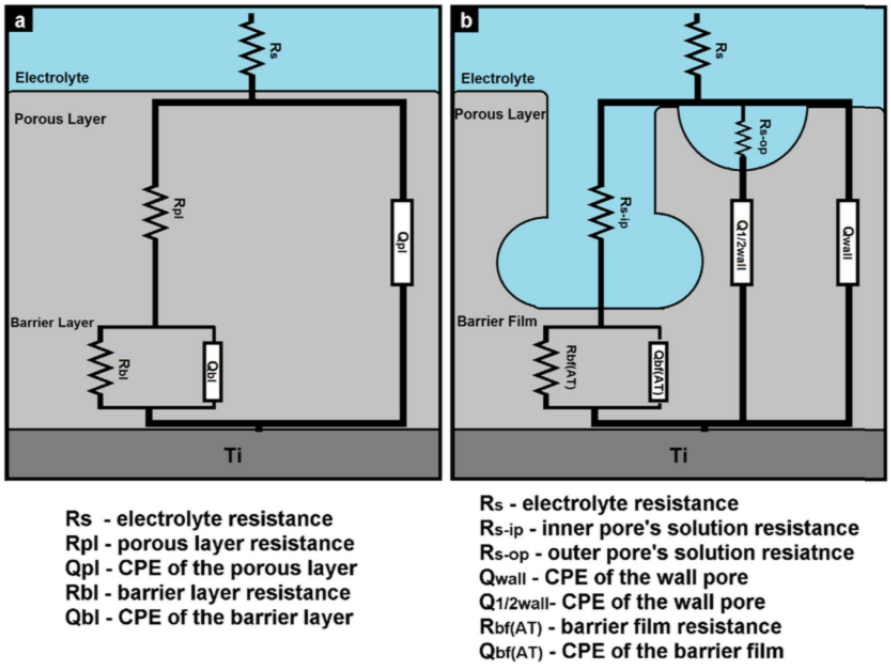

Figure 3.10: Equivalent circuits: a) traditionally used for the fitting of EIS results for porous materials, b) new concept for the fitting of EIS spectra for the anodically treated groups.

Another widely used element is the Warburg element, which is related to diffusion phenomena and is represented with a straight line in the Nyquist diagram (figure 3.11).

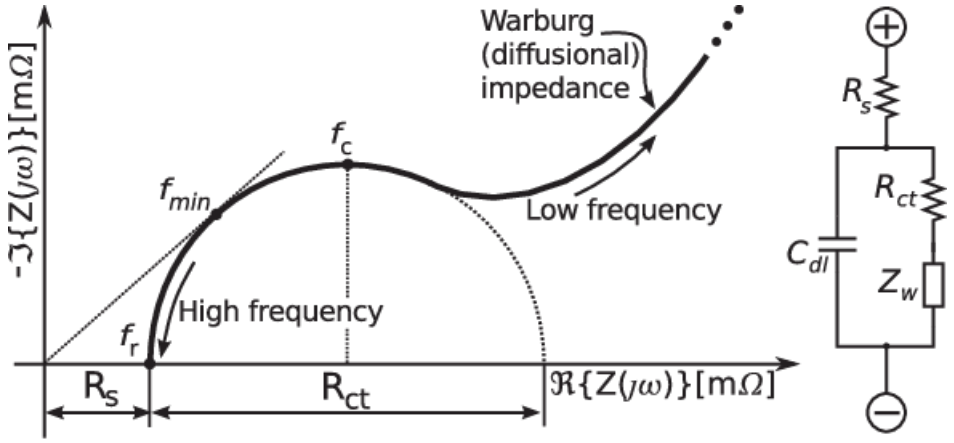

Figure 3.11: Nyquist diagram with Warburg element.

In this circuit the f_c point is the frequency located at the top of the semicircle in the Nyquist impedance diagram. At this frequency, R_{ct} is equal to $1/2\pi f_c C_{dl}$. Over this point, Warburg impedance become important and it deviates the circumference plot.

An important impedance frequency point is $f_{min} = \frac{1}{2\pi C_{dl} R_{ct}} \sqrt{1 + \frac{R_{ct}}{R_s}}$, defines as the tangent point related to the origin of the Nyquist diagram, i.e. the minimum impedance angle.

3.4 SEM

A scanning electron microscope (SEM) is a type of electron microscope that produces images of a sample by scanning the surface with a focused beam of electrons.
The electron beam interact with atoms in the sample, producing various signals that contain information about the surface topography and composition of the sample; it is scanned in a raster scan pattern, and the position of the beam is combined with the intensity of the detected signal to produce an image. The action of the electron beam stimulates emission of high-energy backscattered electrons and low-energy secondary electrons from the surface of the specimen. The number of secondary electrons that can be detected, and thus the signal intensity, depends, among other things, on specimen topography.
SEM can achieve resolution better than 1 nanometer.

3.5 XRD

X-ray diffraction (XRD) is a non-destructive technique for analyzing the structure of materials, primarily at the atomic or molecular level. It works best for materials that are crystalline or partially crystalline (i.e., that have periodic structural order) but is also used to study non-crystalline materials.
XRD relies on the fact that X-rays are a form of light, with wavelengths on the order of angstrom.
X-rays are generated in a cathode ray tube by heating a filament to produce electrons, accelerating the electrons toward a target by applying a voltage, and bombarding the target material with electrons. When electrons have sufficient energy to dislodge inner shell electrons of the target material, characteristic X-ray spectra are produced. The specific wavelengths are characteristic of the target material (Cu, Fe, Mo, Cr). Filtering, by foils or crystal monochrometers, is required to produce monochromatic X-rays needed for diffraction. When X-rays scatter from a substance with structure at that length scale, interference can take place, resulting in a pattern of higher and lower intensities.
A beam of X-rays is directed towards a sample, and the scattered intensity is measured as a function of outgoing direction. By convention, the angle between the incoming and outgoing beam directions is called 2θ. For the simplest possible sample, consisting of sheets of charge separated by a distance d, constructive interference (greater scattered intensity) is observed when Bragg's Law is satisfied. This technique does not allow the measurement of absolute crystalline fraction, but it is able to determine if anatase or rutile crystalline phases are present in more than 2% fraction and, through Spurr-Meyer equation, the relative amount of each crystalline phase [44].

Chapter 4

Experimental

4.1 Samples preparation

The experiments have been performed on titanium grade 2, whose chemical composition and mechanical properties are listed in table 4.1.

Table 4.1: Chemical composition and mechanical properties of samples

Chemical composition	Mechanical properties at room T
C<0,08 %	Yield Strenght: 275 MPa
Fe<0,3 %	Ultimate Tensile Strenght: 345 MPa
H<0,015 %	Elongation>20 %
O<0,25 %	Tensile modulus: 103 GPa
N<0,03 %	Hardness (Vickers): 145
Ti balance	Poisson's ratio: 0,34-0,10

Square samples of 10x10x1.6 mm^3 have been cold-cut from a titanium grade 2 plate. Then, the specimens were all polished with 100, 320, 600 grit SiC papers to obtain a flat surface.
To remove dirt and any solid debris, an ultrasonic washing in alcohol was carried out for 5 minutes, and then a washing in distilled water was performed for another 5 minutes.

4.2 Anodizing

4.2.1 Anodizing machine

The anodization was performed with the Asterion AST 751 (figure 4.1).



Figure 4.1: Asterion AST 751

The maximum applicable power is 750 W and it is possible to work in different regimes: DC, AC and AC+DC. Two DC output ranges are provided, 0-250 V/0-500 V and two AC/AC+DC output ranges, 0-200 v/0-400 V with frequency range of 16-1000 Hz. A wide range of AC and DC loads can be powered, inculding reactive loads (inductive and capacitive) running at full rated apparent power, and non-linear loads drawing current with high crest factor, up to 5:1.
Although the machine can work in a potentiostatic and galvanostatic regime, the potentiostatic was used for my anodizations



Figure 4.2: Steady state panel

In the steady state panel (figure 4.2) is possible to select the output mode, among AC, DC and AC+DC and then the voltage range. Depending on the voltage ragne

selected we can reach different current intensity according to Ohm's Law. For this thesis work only AC regime under 200 V was used.

4.2.2 Solution and Set-up

The anodizing cell is shown in figure 4.3.

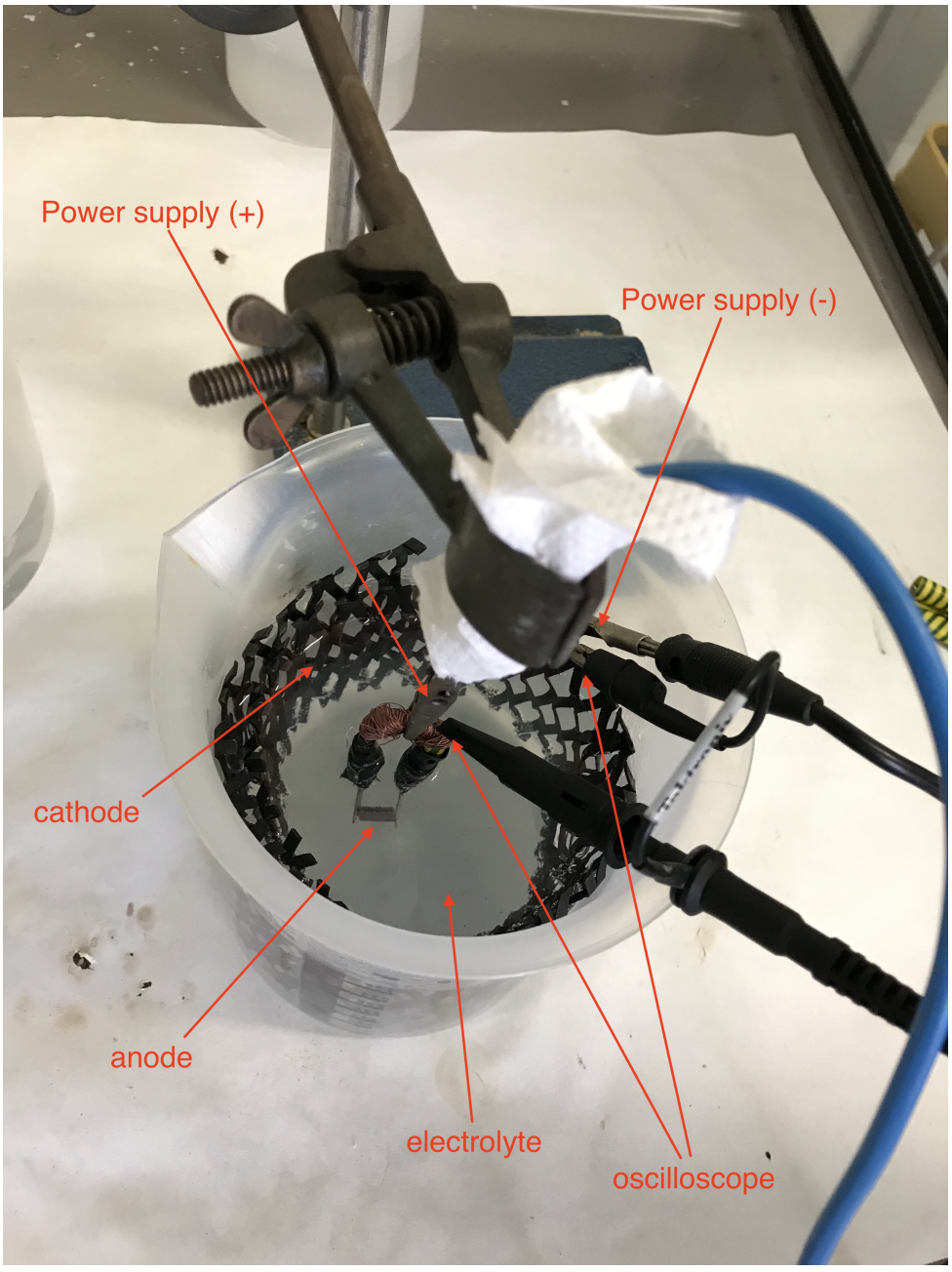

Figure 4.3: Electrochemical cell for anodization.

The cathode is activateted titanium with an Iridium and Ruthenium Enriched Mixed Metal Oxide net and the electrolyte is H_2SO_4 0.5 M (1 liter). The Tektronix TBS 1072B-EDU oscilloscope (figure 4.4) was used to constantly measure the current and voltage.



Figure 4.4: Oscilloscope Tektronix TBS 1072B-EDU

4.2.3 Duty cycle

The shape of the wavefunction has been created with Excel. An example is provided in figure 4.5.

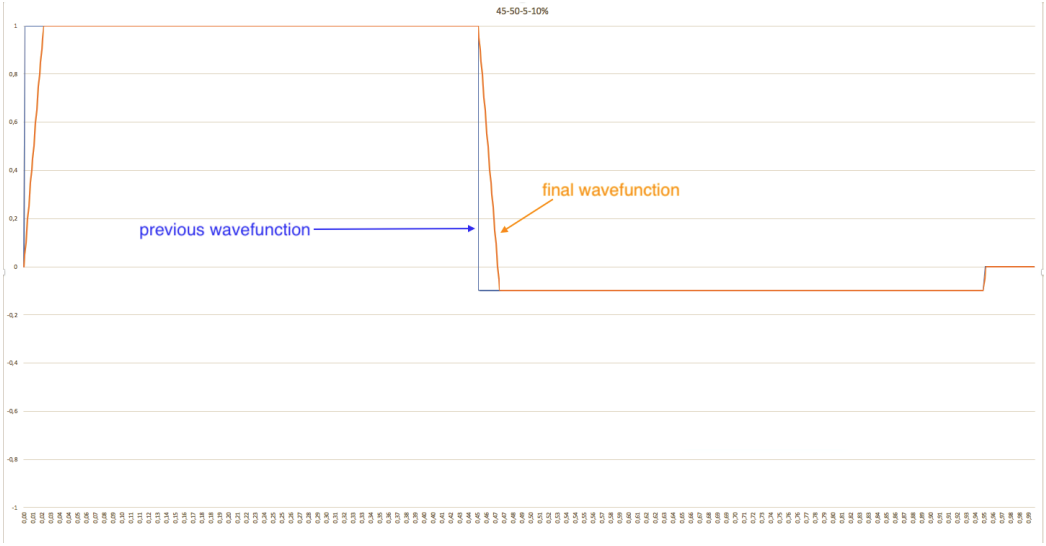

Figure 4.5: Example of duty cycle 45A-50C-5R-10%. Abrupt duty cycle (BLUE) and duty cycle with ramp (ORANGE)

Considering that the main problem was the spike of current when starting a cycle, a new shape of the wavefunction has been created. To reach the potential set, a ramp has been included, instead of an abrupt step.
The nomenclature 45A-50C-5R-10% means: 45% of time with anodic current, 50% of time with cathodic current, 5% of time with no current and 10% is the cathodic peak, i.e. the applied amount of cathodic polarization with respect to the anodic one.

4.3 Immersion test

Immersion corrosion testing is used to determine the resistance of a material to an aggressive, aqueous environment. The test was performed in an aqueous solution containing sulfuric acid 3% and 10% in volume at 60 °C for 24 hours.
9 samples were tested during a single immersion test (8 anodized and 1 only polished and cleaned). The samples were weighed before and after the test in order to obtain the mass difference and their size was calculated to determine their volume. Using the formula: $CR(\frac{mm}{year}) = \frac{K*(Weight_b - Weight_a)}{Area*thickness*desnity}$ where CR($\frac{mm}{year}$) is the corrosion rate expressed in mm per year, K is a constant which is equal to 87600, Weight$_b$ is the weight of the sample before test, Weight$_a$ is the weight after test, area is the area of the sample exposed to the aggressive environment, thickness is the thickness of the sample, and density is the density of the samples which is equal to 4,506 $\frac{g}{cm^3}$.

4.4 Potenziodynamic test

Cathodic polarization has been performed in H_2SO_4 0.5 M solution with MetroOhm Autolab Potentiostat M204.
Open circuit potential (OCP) has been recorded after 20 minutes of sample exposition to the testing solution with a SSC reference electrode.
Then the potential has been scanned from 200 mV above OCP down to 3 V SSC at 20 mV/min.
Cathodic current and potential difference between metal and reference electrode have been registered with Nova software.
Tests have been performed in 1 L cell filled with sulfuric acid solution.
Anodic polarization has been performed in NaBr 0.5 M solution with MetroOHm Autolab Potentiostat M204.
Open circuit potential (OCP) has been recorder after 20 minutes of sample exposition to the testing solution with a SSC reference electrode.
Then the potential has been scanned from 100 mV below the OCP up to 8 V SSC at 20 mV/min.
Anodic current and potential difference between metal and reference electrode have been registered with Nova software.

4.5 EIS

Electrochemical impedance spectroscopy was performed in NaBr 0.5 M solution and in H_2SO_4 0.5 M solution with MetroOhm Autolab Potentiostat M204 (figure 4.6).
Open circuit potential (OCP) has been recorder after 20 minutes of sample exposition to the testing solution with SSC reference electrode (figure 4.7).
The potential applied was a sinusoidal function with an amplitude of 10 mV around OCP with frequencies from 10^{-2} to 10^5 Hz.



Figure 4.6: Multi Autolab/M204 - Twelve Channel Multi Potentiostat/Galvanostat

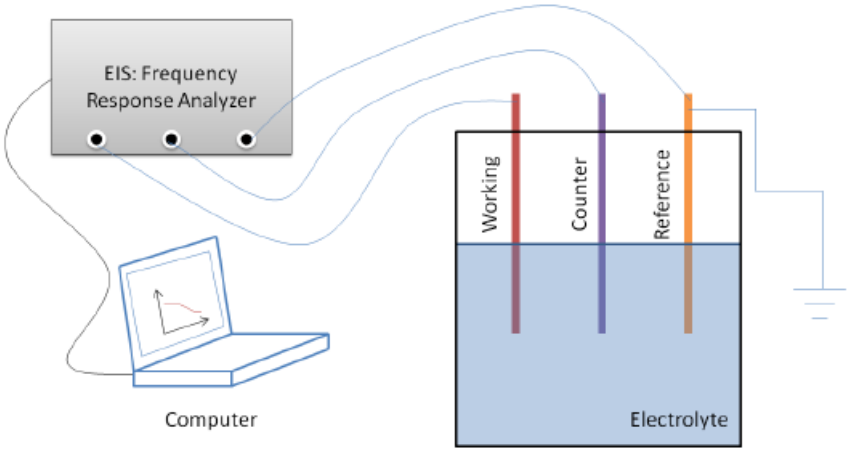

Figure 4.7: EIS cell

4.6 SEM and XRD

A scanning electron microscope Carl Zeiss EVO 50VP has been used to capture a magnified image of the samples in order to investigate their morphology.
To analyse the crystallinity of the oxide layers, it has been used an XRD technique, with a diffractometer model Phillips PW 1830, able to generate a Cu-Kα radiation with a wavelength of 0.154 nm.

4.7 Analysis of porosity

To measure the porosity of the oxide coating ImageJ has been used. ImageJ is a Java-based image processing program developed at the National Institutes of Health and the Laboratory for Optical and Computational Instrumentation (LOCI, University of Wisconsin).
A binary image has been created, after setting the brightness and the contrast, to analyze the black particles (pores).
Using the minimum and maximum dimension of the pores the undesired particles originated from the process have been excluded.

Chapter 5

Results & Discussion

5.1 Duty selection

Firstly, 10 duty were performed:

- 90A-5C-5R
- 80A-10C-10R
- 70A-25C-5R
- 60A-35C-5R
- 55A-40C-5R
- 50A-40C-10R
- 45A-50C-5R
- 30A-60C-10R
- 25A-70C-5R
- 10A-80C-10R

Each duty was performed with 4 different cathodic peaks: 2, 5, 7, and 10 % and at 3 different frequencies: 20, 500, and 1000 Hz.
So, a total of 120 samples were anodized.
Between them, only 2 duties (55A-40C-5R and 45A-50C-5R) with the four cathodic peak and two frequencies (20 and 1000 Hz) have been selected to be tested.
The 4 duties were selected based on the color of the oxide formed: they showed a gray, light and opaque color. For the cycles showing the best resistance to corrosion in sulphuric acid environment, the trend of current and voltage was recorded at 1, 2, 3, 4, and 5 minutes.
From the images shown in the following sections, that describe the voltage and current waveforms, it is possible to see the presence of anodic and cathodic peaks. These peaks are present in the current trend, and consequently also in the voltage one. These current peaks are determined by capacitive effects, such as charge and discharge of the double layer at the interface between oxide and electrolyte. After the passage of this peak the plateau of current (and therefore also of voltage) is

reached, which is the value necessary to support the growth of the oxide.
Another important effect worth to be analyzed, occurring for example in the sample 55A-40C-5R-5%-1000 Hz, is the presence of voltage drop which can be caused by a phenomenon called "soft spark". During the soft spark, the sparks decrease in number and intensity and a different noise is heard during the anodizing process. From the experiment conducted the soft spark regime (55A-40C-5R-5%-1000 Hz and 45A-50C-5R-5%-1000 Hz) becomes more visible (figures 5.7 and 5.20) when we increase the cathodic peak and the frequency. However, once the anodic contribution was lower than the cathodic polarization imposed to the sample, no soft spark was observed and the corrosion rate verified through immersion test was high. This evidence highlights that the benefit gained when using high cathodic current contributions can sometimes be hindered by other deleterious phenomena decreasing the corrosion resistance of the coating.

5.1.1 55A-40C-5R-5%-20 Hz

The first sample was the 55A-40C-5R-5%-20 Hz which doesn't show a significant reduction in voltage during the anodization process; in fact, the voltage increase of 0.5 V/s is respected, as can be seen in figure 5.1.

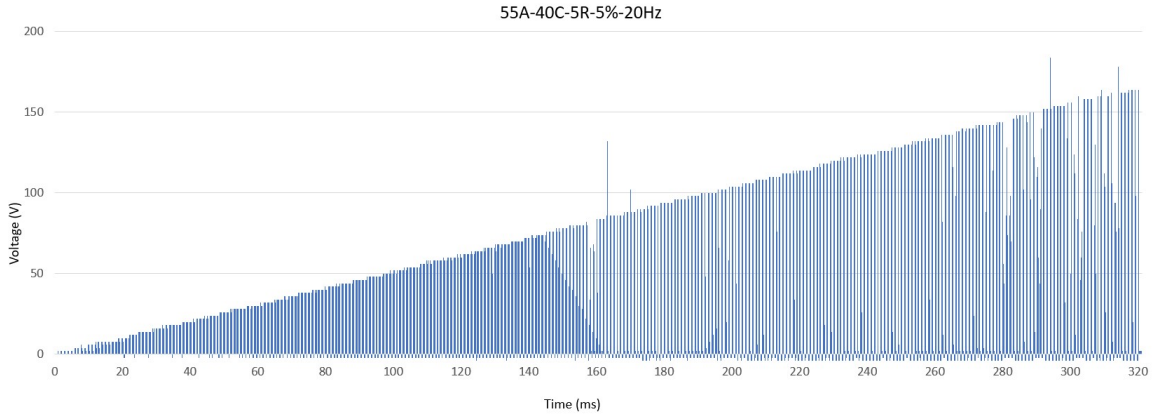

Figure 5.1: Voltage trend during anodization

From figures 5.2 and 5.3 it is possible to see that the voltage (and the current) follow exactly the input waveform.
Instead, after 3 minutes, at about 85/90 V (figures 5.4, 5.5, and 5.6), the voltage waveform is disturbed and not equal to that initially given, sparks begin to form and many gas bubbles are observed. As a consequence, the trend of the current is also variable.
Even if the waveforms do not reflect those given as an input, among all the analyzed samples, the sample 55A-40C-5R-5%-20 Hz is the one that shows the minor variation. This is probably due to the low frequency (20 Hz), with respect to the others (1000 Hz), which favors the development of all the faradaic processes involved during anodizing.

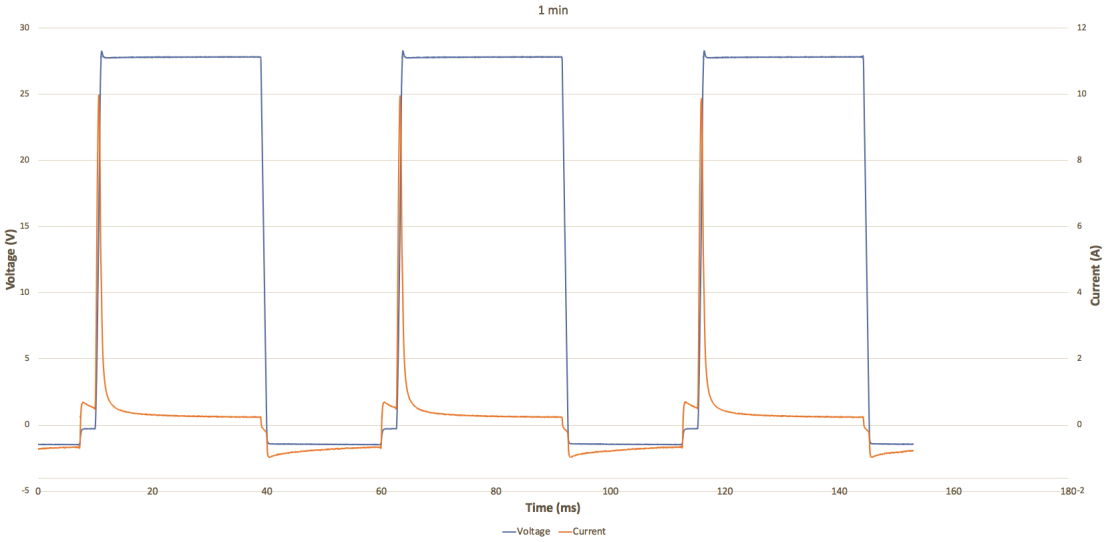

Figure 5.2: Voltage and Current at 1 minute

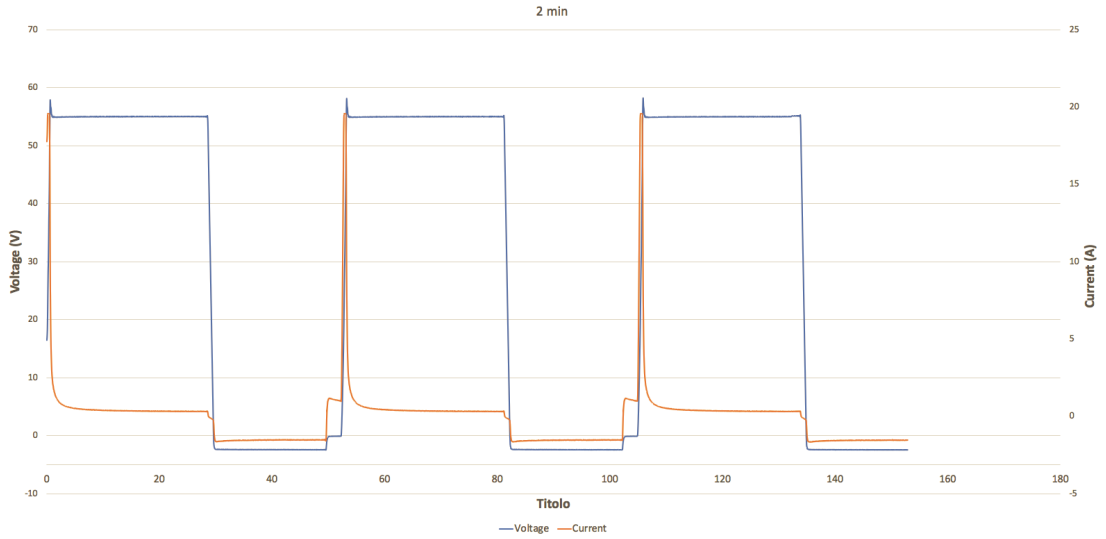

Figure 5.3: Voltage and Current at 2 minutes

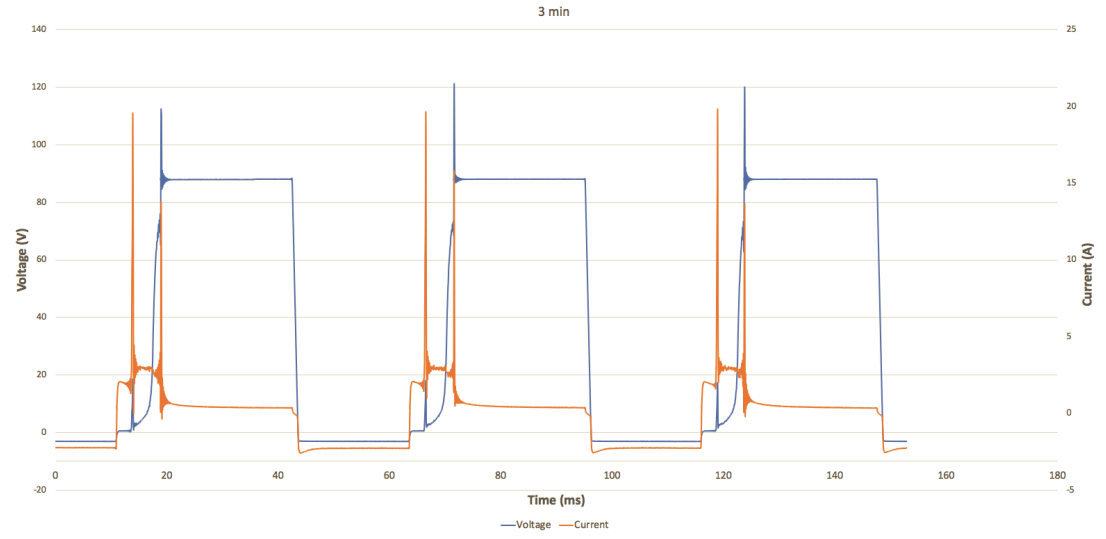

Figure 5.4: Voltage and Current at 3 minutes

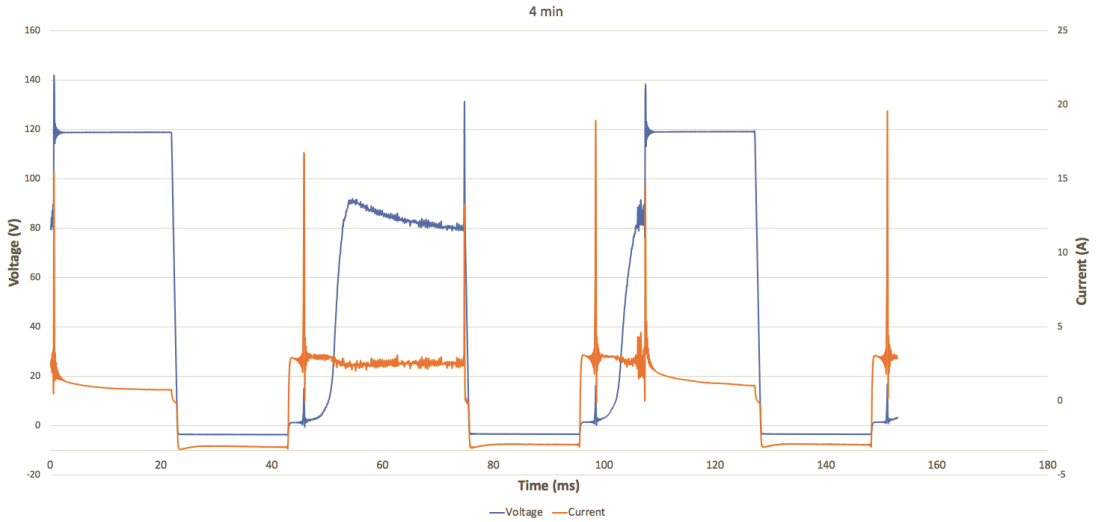

Figure 5.5: Voltage and Current at 4 minutes

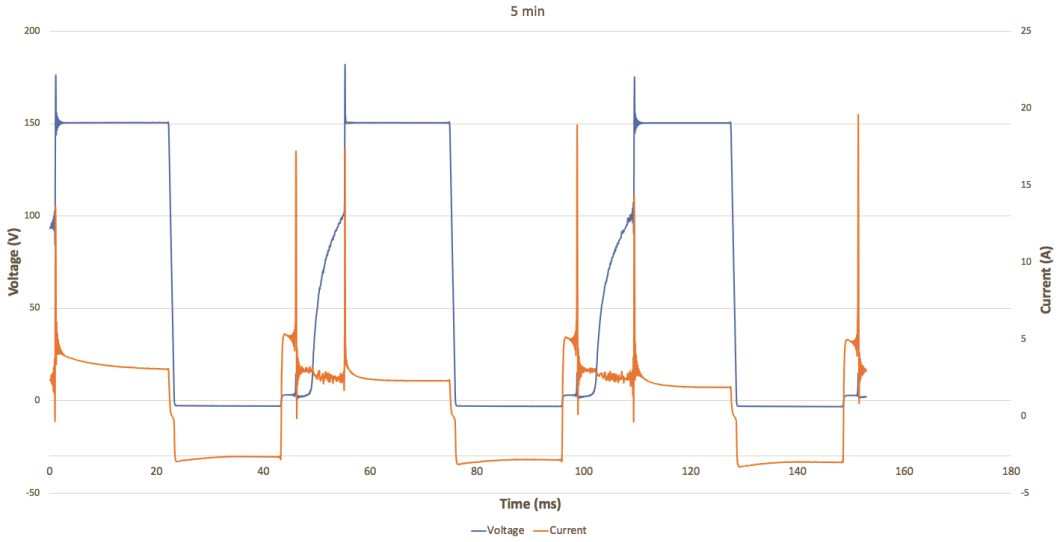

Figure 5.6: Voltage and Current at 5 minutes

5.1.2 55A-40C-5R-5%-1000 Hz

The second sample was the 55A-40C-5R-5%-1000 Hz which shows a reduction in voltage during the anodization process, starting from 220 seconds, as can be seen in figure 5.7.

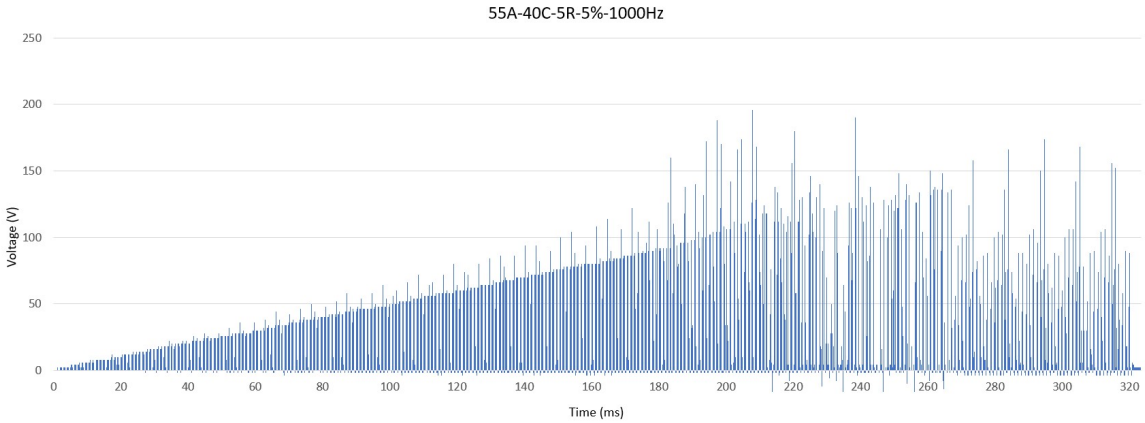

Figure 5.7: Voltage during anodization

From figures 5.9 and 5.10 it is possible to see that the voltage (and the current) follow exactly the input waveform.
Instead, after 3 minutes, at about 85/90 V (figures 5.11, 5.12, and 5.13), the voltage waveform is disturbed and not equal to that initially given, sparks begin to form and many gas bubbles are observed. As a consequence, the trend of the current is also very variable with cathodic peaks that reach the maximum current value (20 A). At 5 minutes the current has almost only peaks. In figure 5.8 the photos of the sample before (A) and after (B) the soft spark are shown: it is possible to notice how the specimen has become more opaque after the soft spark due to the increase of the oxide thickness and the sparks have completely disappeared.

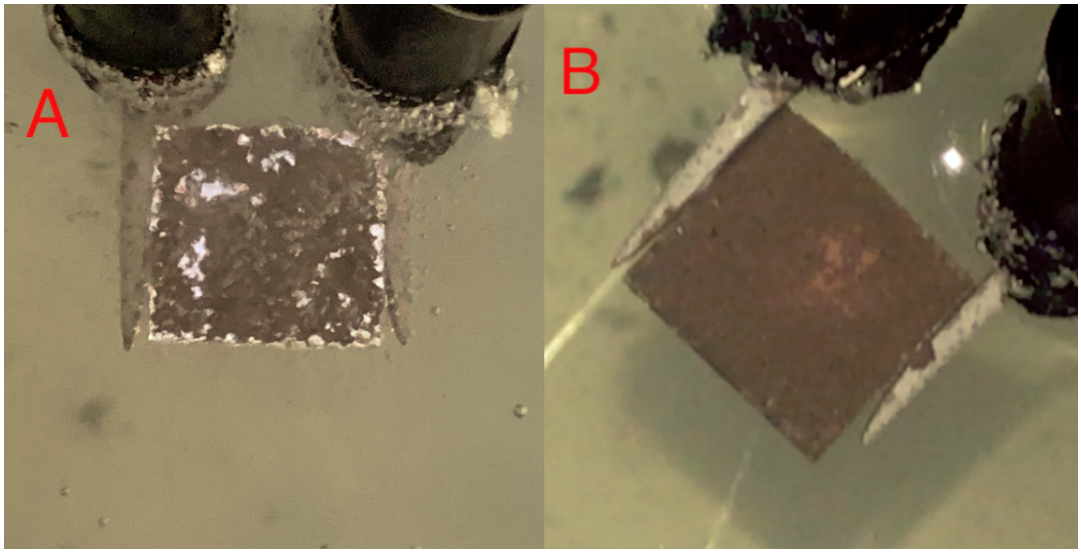

Figure 5.8: Sample before (A) and after (B) the soft spark.

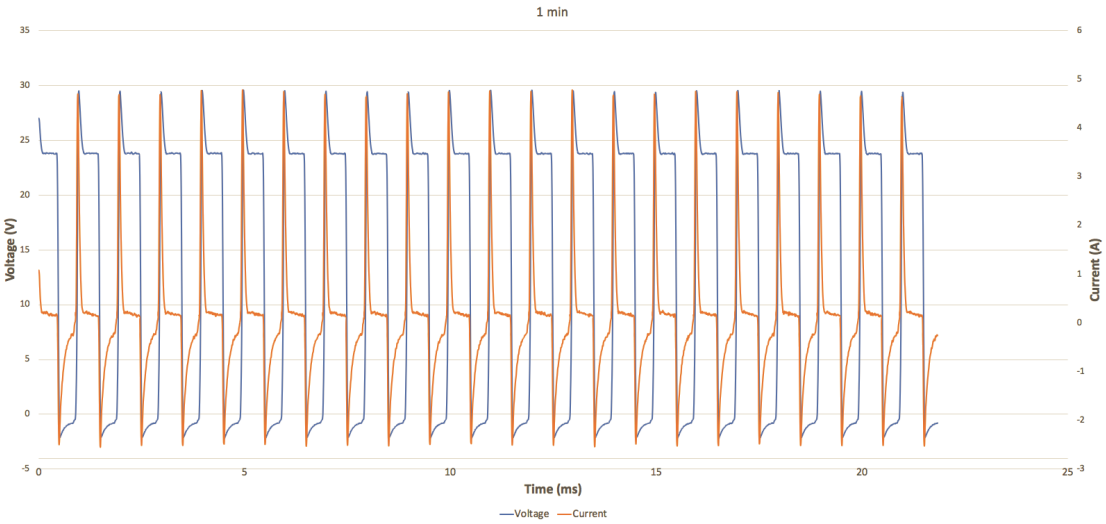

Figure 5.9: Voltage and Current at 1 minute

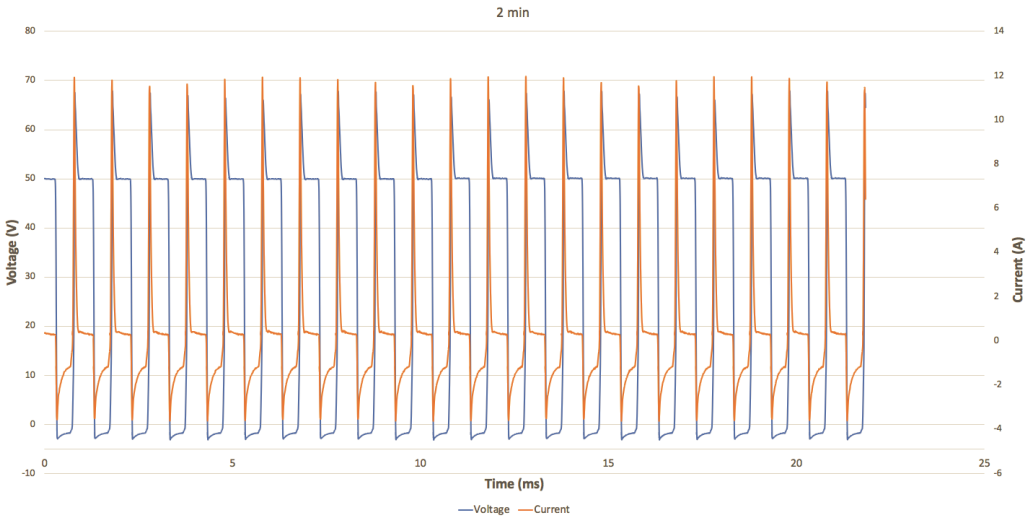

Figure 5.10: Voltage and Current at 2 minutes

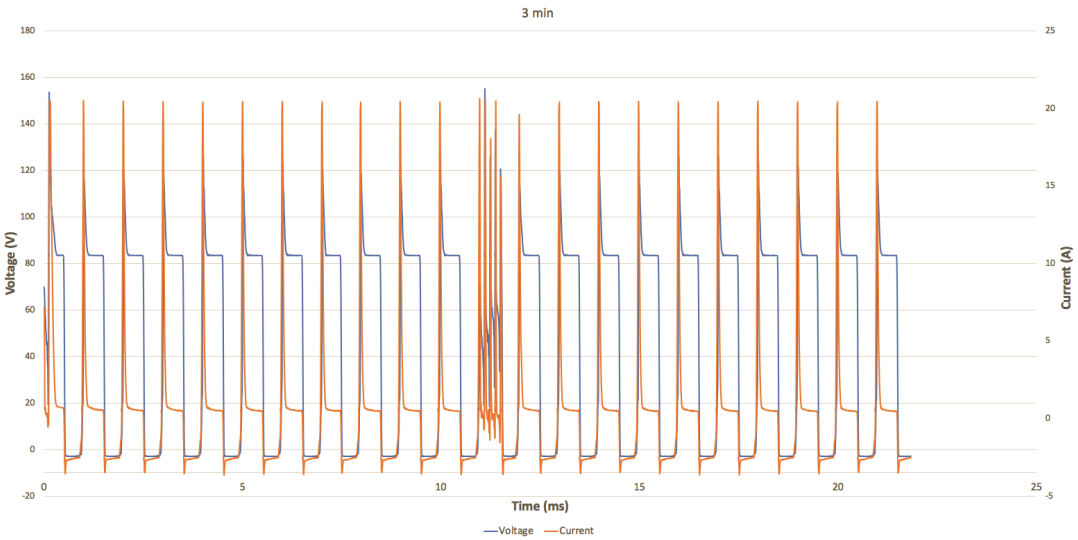

Figure 5.11: Voltage and Current at 3 minutes

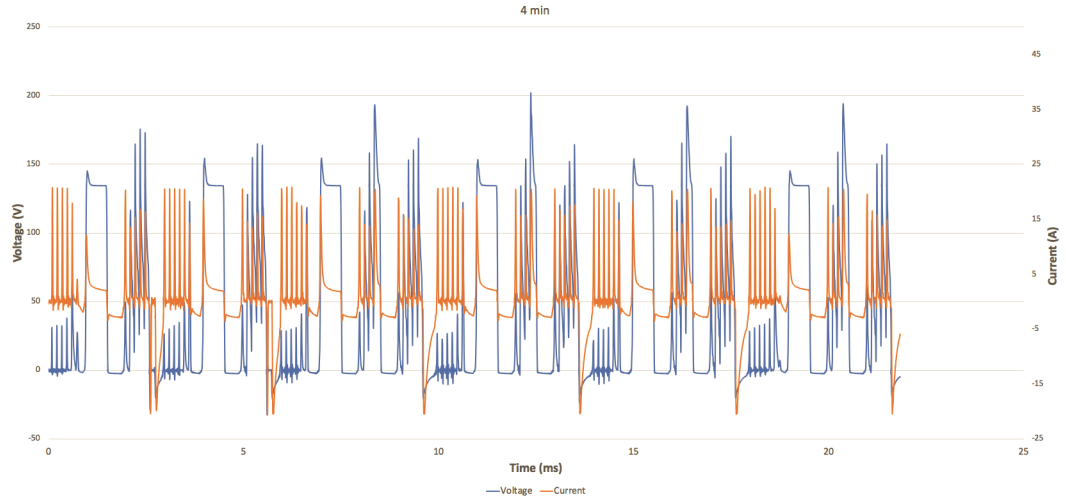

Figure 5.12: Voltage and Current at 4 minutes

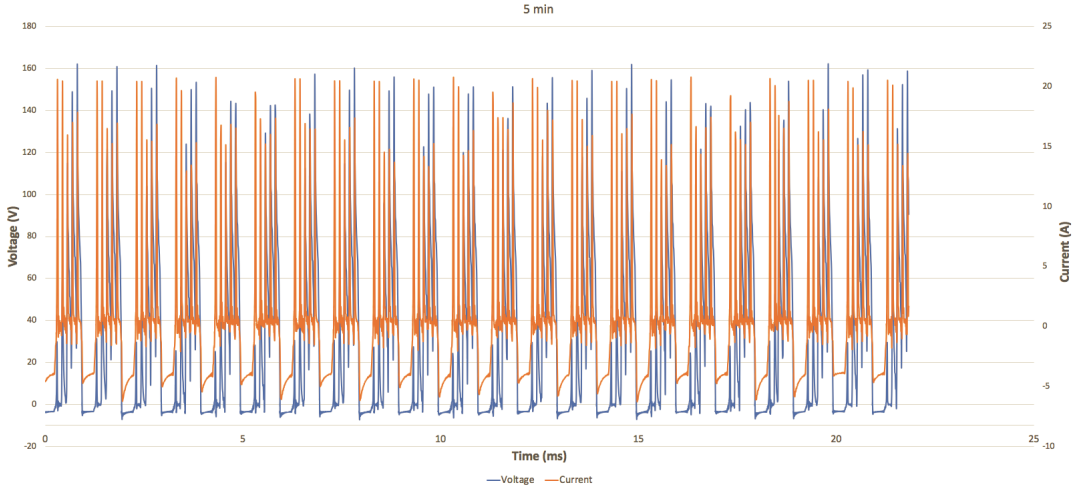

Figure 5.13: Voltage and Current at 5 minutes

5.1.3 45A-50C-5R-2%-1000 Hz

The third sample was the 45A-50C-5R-2%-1000 Hz which doesn't show a significant reduction in voltage during the anodization process, as we can see from figure 5.14.

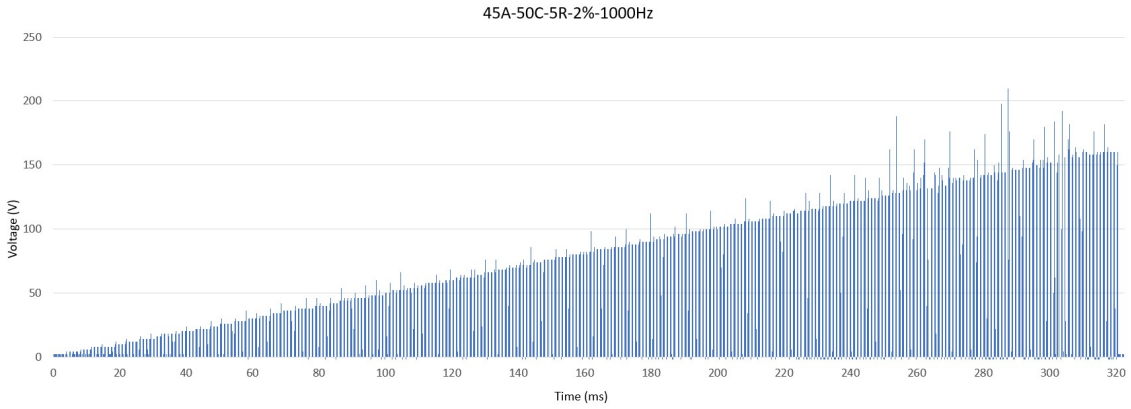

Figure 5.14: Voltage trend during anodization

From figures 5.15, 5.16, and 5.17 it is possible to see that the voltage (and the current) follow exactly the input waveform.
Instead, after 4 minutes (figures 5.18 and 5.19), the voltage waveform is disturbed and not equal to that initially given. As a consequence, the trend of the current is also very variable with cathodic peaks that reach the maximum current value (20 A) at 4 minutes. In figure 5.15 it is possible to notice that the downward current trend takes a longer time to reach the plateau value so it is possible to speculate a larger time constant attributed to the electrochemical process. However, this only happens for the first minute: subsequently, the current quickly reaches the plateau value as in the previous specimens. Furthermore, as it is possible to see in figures 5.18 and 5.19, current and voltage peaks are still present as for the case of the previous sample. Based on that it is reasonable to correlate their origin not only on surface sparks but also on other phenomena requiring a more in depth analysis.

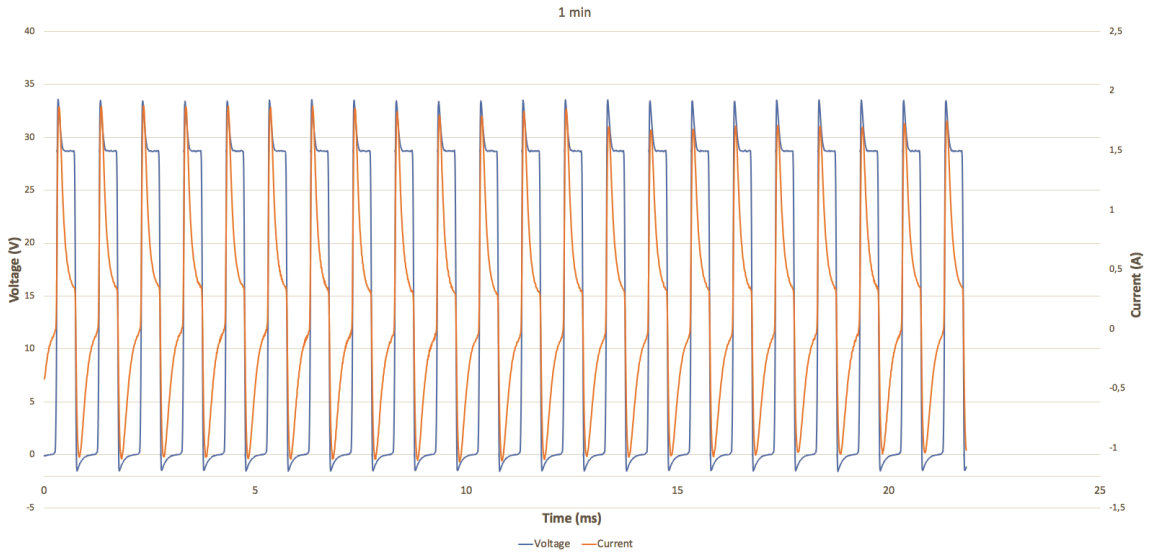

Figure 5.15: Voltage and Current at 1 minute

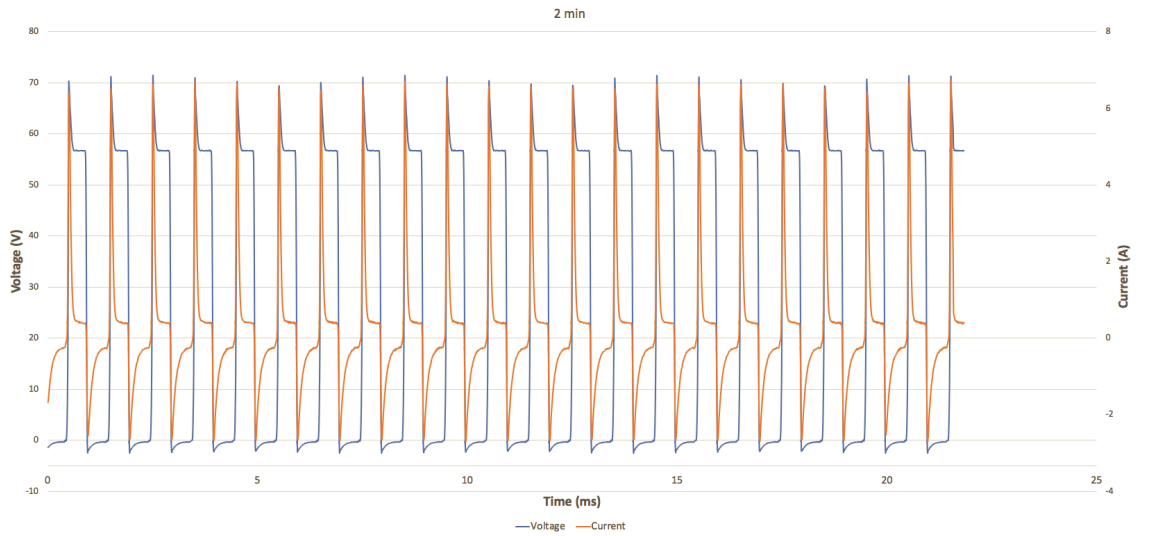

Figure 5.16: Voltage and Current at 2 minutes

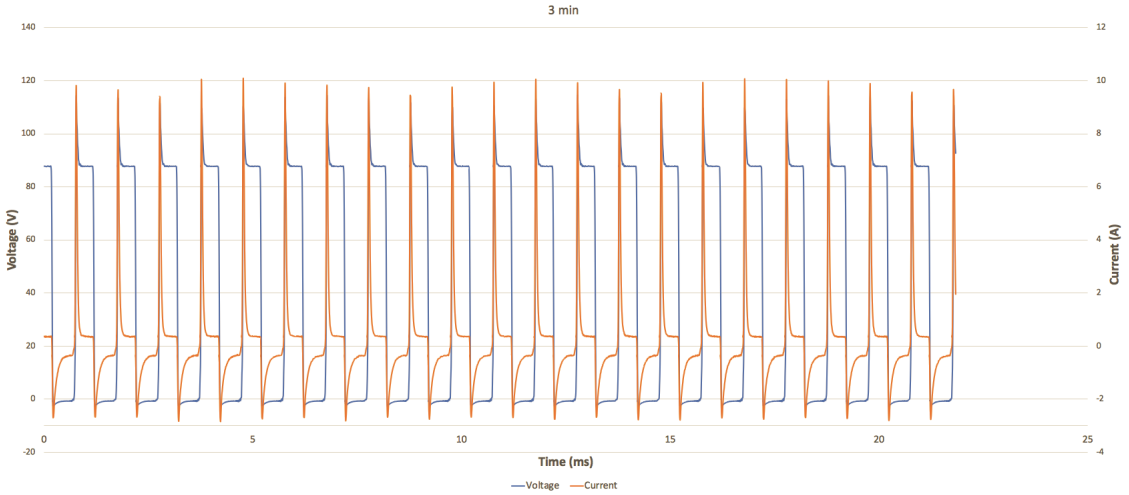

Figure 5.17: Voltage and Current at 3 minutes

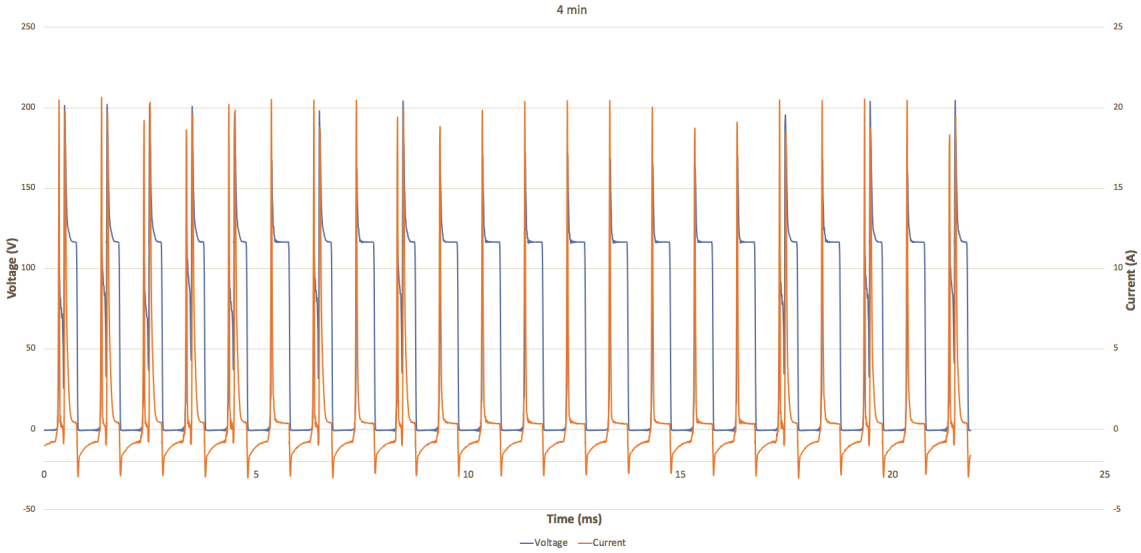

Figure 5.18: Voltage and Current at 4 minutes

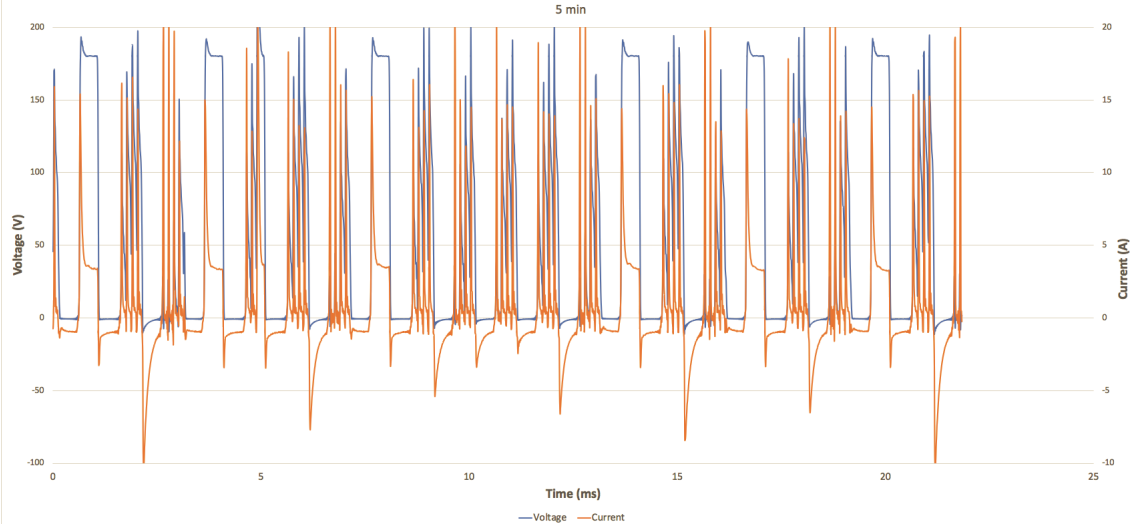

Figure 5.19: Voltage and Current at 5 minutes

5.1.4 45A-50C-5R-5%-1000 Hz

The fourth sample was the 45A-50C-5R-5%-1000 Hz which shows a reduction in voltage during the anodization process,starting around 200 seconds, as we can see from figure 5.20.

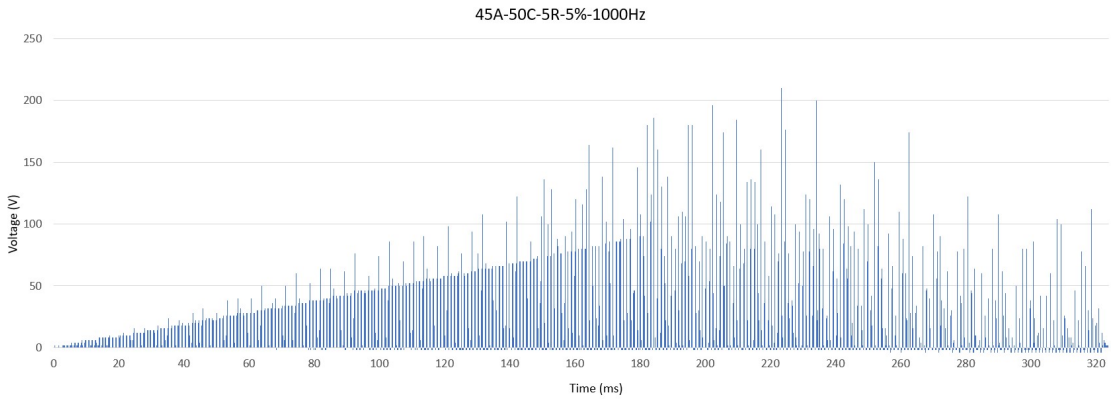

Figure 5.20: Voltage trend during anodization

From figures 5.22 and 5.23 it is possible to see that the voltage (and the current) follow exactly the input waveform.
Instead, after 3 minutes (figures 5.24, 5.25, and 5.26), the voltage waveform is disturbed and not equal to that initially given. As a consequence, the trend of the current is also very variable with cathodic peaks that reach the maximum current value (20 A) at 4 minutes. In figure 5.21 the photos of the sample before (A) and after (B) the soft spark are shown: it is possible to notice how the specimen has become more opaque after the soft spark due to the increase of the oxide thickness and the sparks have completely disappeared.

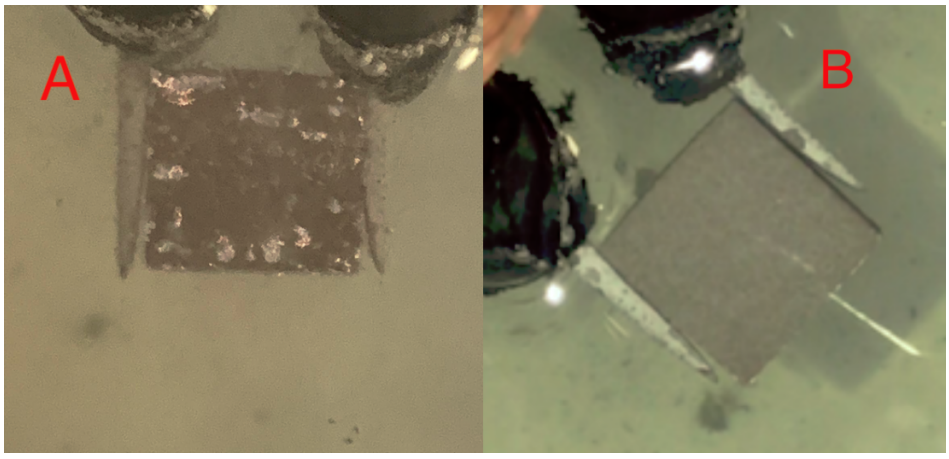

Figure 5.21: Sample before (A) and after (B) the soft spark.

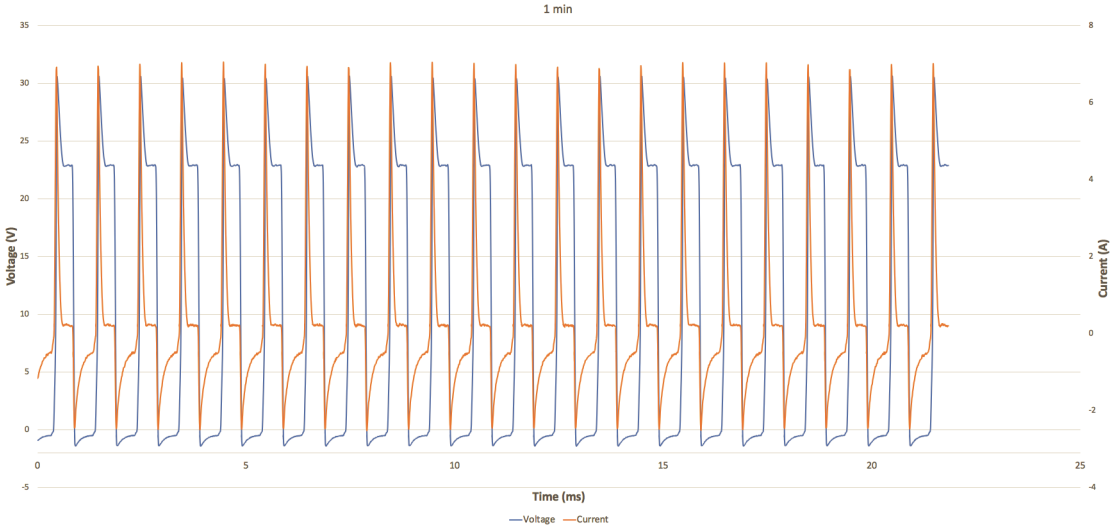

Figure 5.22: Voltage and Current at 1 minute

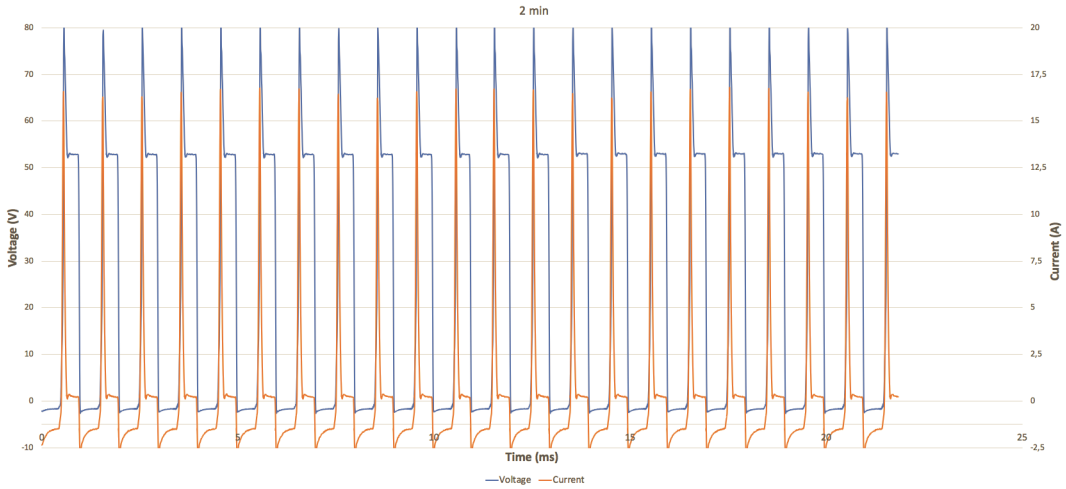

Figure 5.23: Voltage and Current at 2 minutes

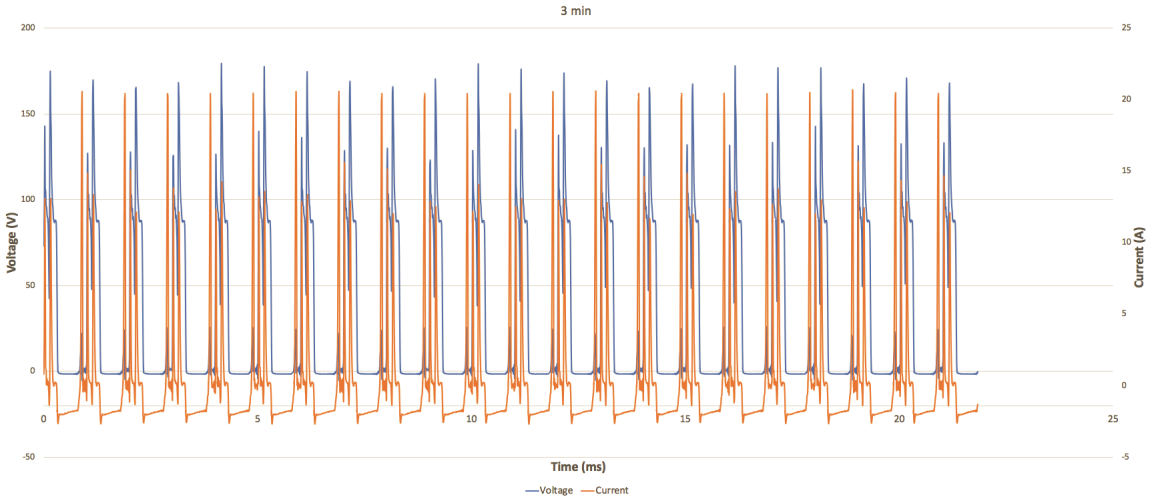

Figure 5.24: Voltage and Current at 3 minutes

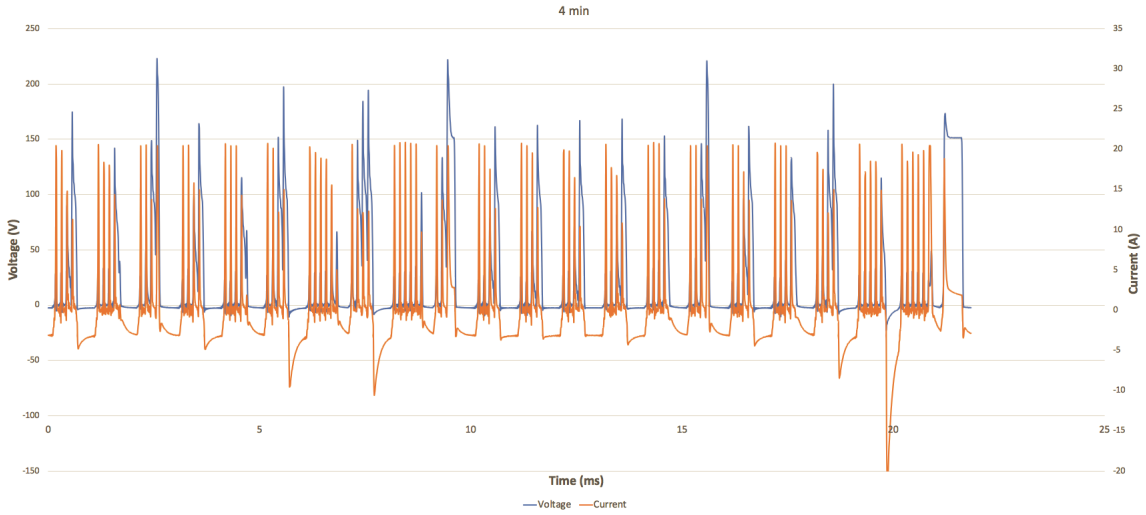

Figure 5.25: Voltage and Current at 4 minutes

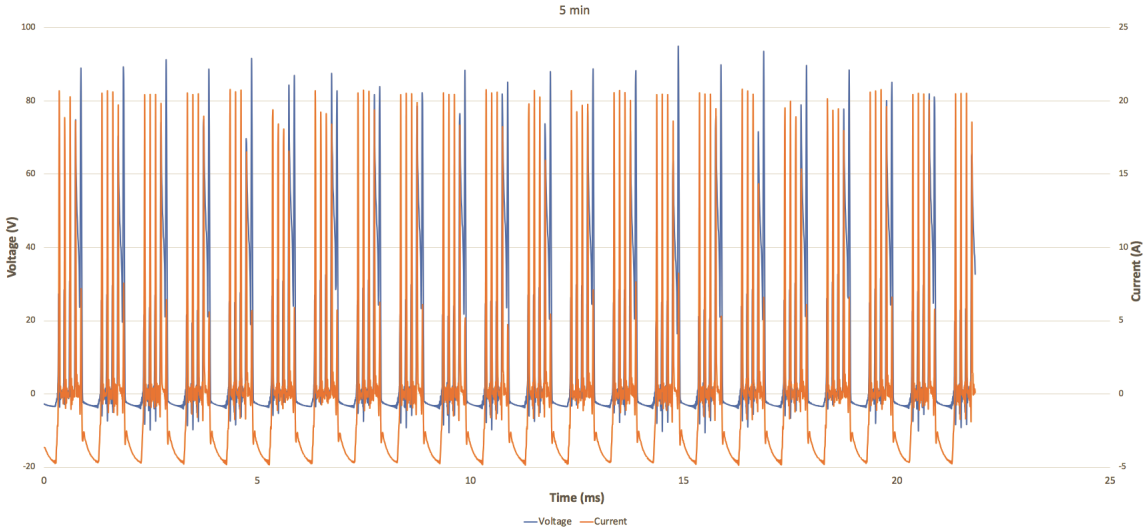

Figure 5.26: Voltage and Current at 5 minutes

5.2 Immersion test

The first immersion test was performed in H_2SO_4 3% in volume at 60°C for 24 hours obtaining quite low corrosion rate values, always below 0.5 mm/year (figure 5.27).

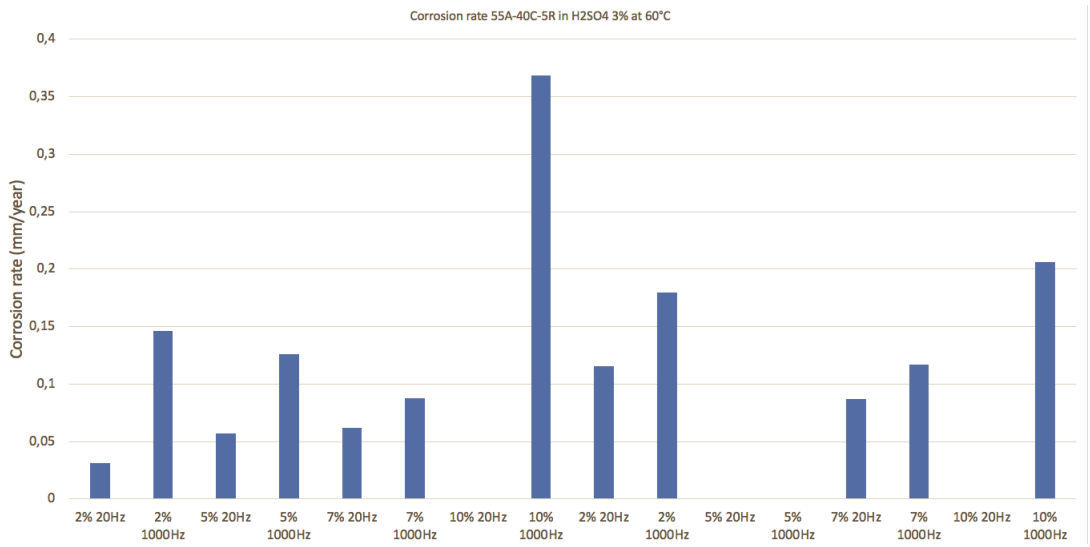

Figure 5.27: Corrosion rate of samples in H_2SO_4 3% in volume at 60°C

Then, it was decided to increase the amount of H_2SO_4 up to 10% in volume in order to increase the magnitude of the corrosion rate and so to avoid the influence of random errors in modifying the final trend.
The corrosion rates of the 16 tested samples are reported in figures 5.28 and 5.29. As can be seen, 4 samples (table 5.1) have a very low corrosion rate while the others show corrosion rate in the range 3 to 7 mm/year, approaching the value of pristine grade 2 titanium (8.1 mm/year). After the test, only on these samples the oxide layer was found; on the others the anodically grown oxide was completely removed. There are two main reasons for the weight loss: the corrosion of the coating due to the acidic solution and the detachment of the coating. It would be necessary to evaluate these two effects separately to understand how to improve the resistance of the coating in the acidic environment and to improve the adhesion of the coating to the substrate. It is possible to see that the best results in terms of corrosion resistance are obtained using intermediate values of cathodic polarization, balancing the helpful increase of crystal phase limiting as much as possible losses in compactness.

Table 5.1: Corrosion rates of the specimens that had kept the oxide layer after the test

Samples	**Corrosion rates (mm/year)**
55A-40C-5R-5%-20Hz	0.0592
55A-40C-5R-5%-1000Hz	0.0304
45A-50C-5R-2%-1000Hz	0.0322
45A-50C-5R-2%-1000Hz	0.0807

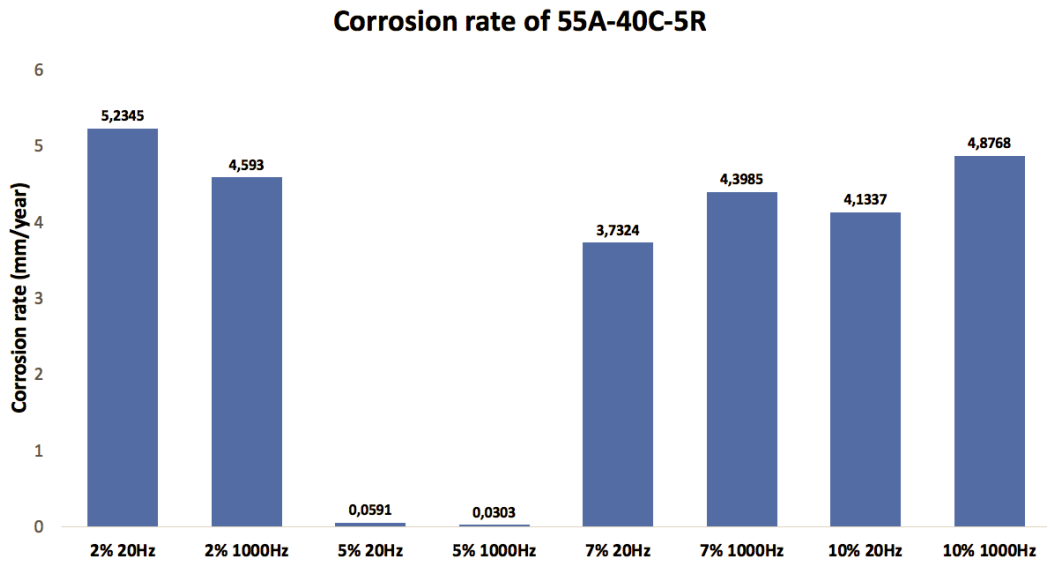

Figure 5.28: Corrosion rate of 55A-40C-5R samples in H_2SO_4 10% in volume

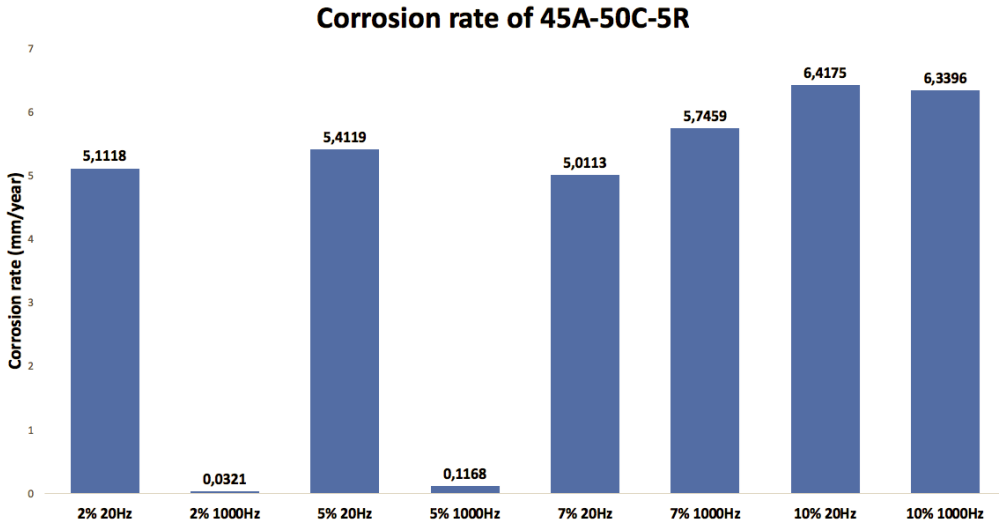

Figure 5.29: Corrosion rate of 45A-50C-5R samples in H_2SO_4 10% in volume

5.3 Cathodic Polarization

The main reactions involved during the cathodic scan in sulphuric acid are:

- Reduction of oxygen: ($O_2 + 4H^+ + 4e^- \rightarrow H_2O$), with a reduction potential equal to 1.21 V SHE at che considered pH value (i.e. about 1 V SSC)

- Evolution of hydrogen ($2H^+ + 2e^- \rightarrow H_2$, with a reduction potential equal, by definition, to 0 V SHE to the considered pH value (i.e. about -0.2 V SSC)

All the four samples analyzed (figure 5.30) show a similar trend in the different regions corresponding to different processes described in detail in the chapter 3.2.2.

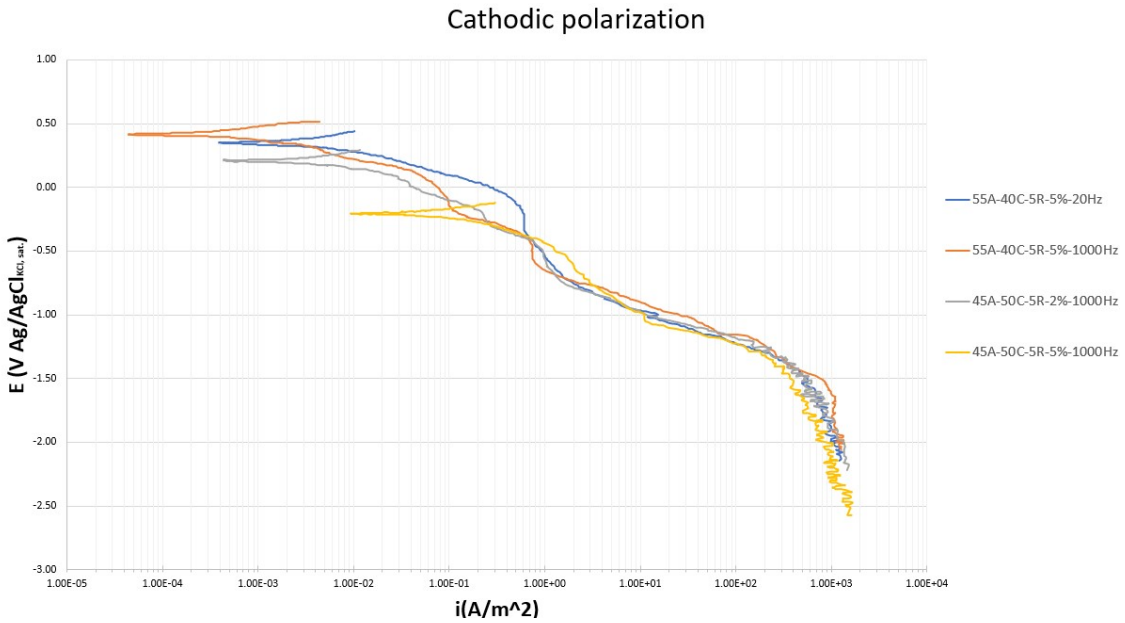

Figure 5.30: Cathodic polarization curves

In the table 5.2 it is possible to see the different values of OCP (V), oxygen limiting current, and hydrogen limiting current of the different samples. The H limiting current was found by plotting the tangent and intersecting it with the potential at -3 V.
The sample 55A-40C-5R-5%-20 Hz has the lowest value of oxygen and hydrogen limiting current indicating a positive contribution of the coating in limiting diffusion of reactants towards the substrate at low potential values while the sample 55A-40C-5R-5%-1000 Hz has the highest OCP.

Table 5.2: Values of OCP (V), Oxygen limiting current (A/m^2), H limiting current (A/m^2).

Samples	OCP (V)	Oxygen limiting current (A/m^2)	H limiting current (A/m^2)
55A-40C-5R-5%-20 Hz	0.35	0.6	1500
55A-40C-5R-5%-1000 Hz	0.43	1	3000
45A-50C-5R-2%-1000 Hz	0.2	3	2000
45A-50C-5R-5%-1000 Hz	-0.2	2	2500

5.4 Anodic Polarization

The only sample subjected to this test is the 55A-40C-5R-5%-1000 Hz (figure 5.31), which has the lowest corrosion rate in the immersion test. While the anodic scan was in progress, four EIS, at OCP, 2, 4 and 6 volt, were performed in order to understand the corrosion of the oxide during the test. During the EIS the potential was kept constant for 30 min in order to provide stabilization to the system to ensure linearity for the subsequent EIS test.
Following this procedure EIS tests were performed starting from the OCP value of the system. Then, previous anodic scan EIS were evaluated every 2 V, for a total of 4 tests.

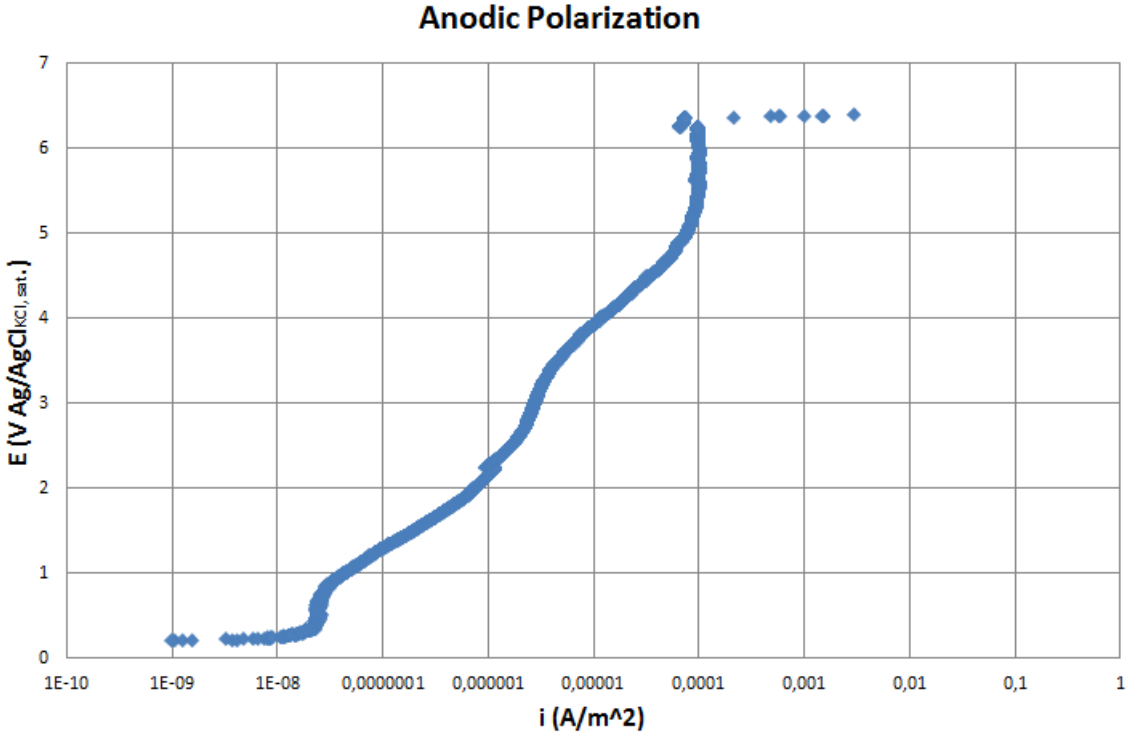

Figure 5.31: Anodic polarization of sample 55A-40C-5R-5%-1000 Hz.

Tests were performed in NaBr 0.5 M solution at 50 °C.
This sample has a pitting potential of 6.4 V so the coating has a good pitting resistance. This is probably due to a high thickness of the coating and to the fact that the oxide generated in the micro-discharges has occupied the surrounding pores creating a more compact and less porous layer. Even if the pitting potential has a high value, it is lower than that of the specimens analyzed in previous research [102][44]. This is probably due to the fact that the sample has been kept at 2, 4 and 6 volt for 30 minutes each time when an EIS was performed. During this time the dissolution of the coating proceeded decreasing its thickness and reducing the final pitting potential.

The Nyquist plot, Bode Modulus, and Bode Phase are reported in figures 5.32, 5.33, and 5.34.

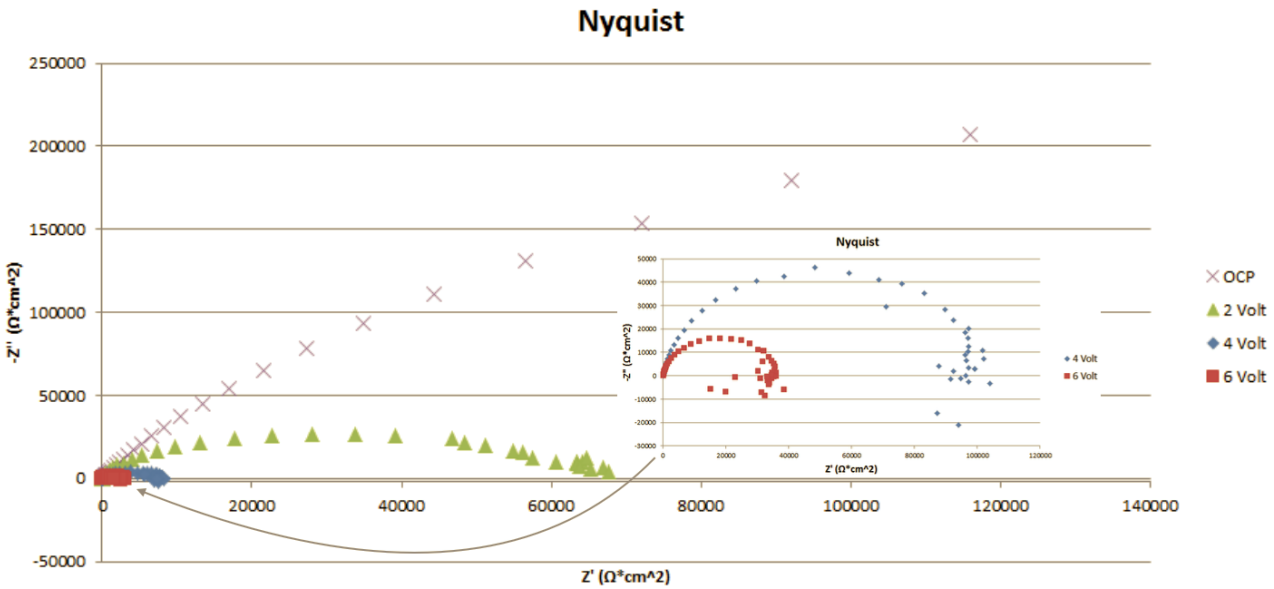

Figure 5.32: Nyquist diagram of the sample 55A-40C-5R-5%-1000 Hz during anodic polarization test.

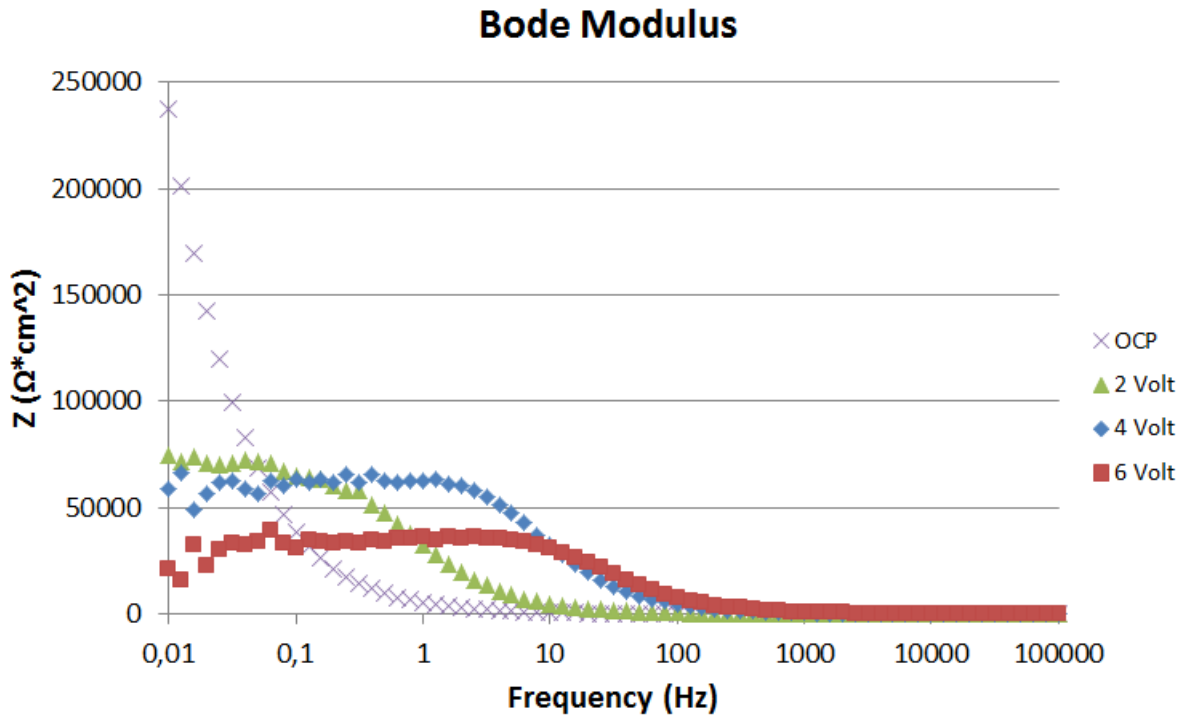

Figure 5.33: Bode Modulus of the sample 55A-40C-5R-5%-1000 Hz during anodic polarization test.

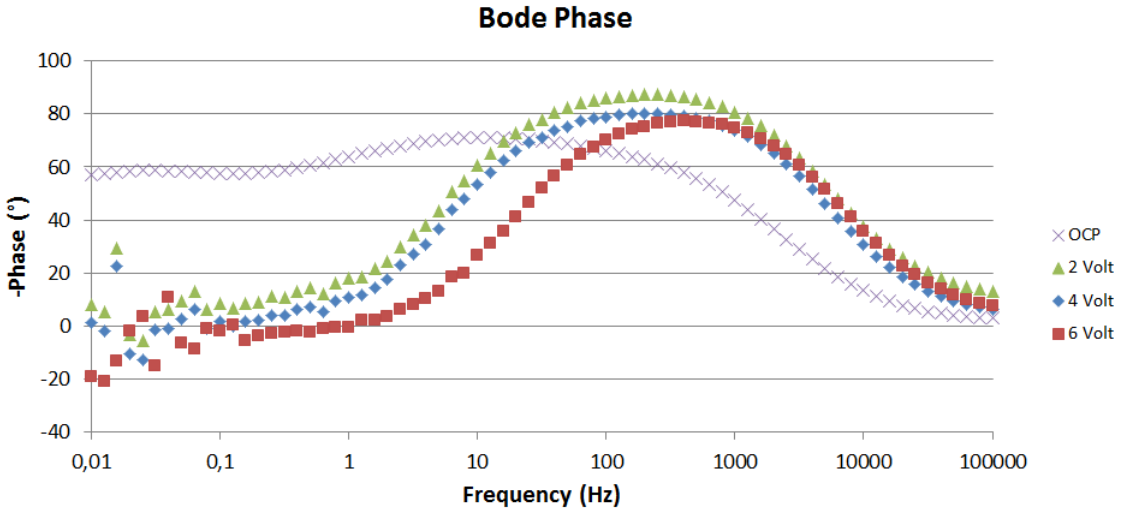

Figure 5.34: Bode Phase of the sample 55A-40C-5R-5%-1000 Hz during anodic polarization test.

Fitting, with the circuit, has not been performed since the noise at low frequencies is very high. However, it is possible to notice from the lower radius in the Nyquist graph that as the voltage increases, during the anodic polarization, the resistance of the coating decreases. For what concern the Bode plot, it is evident a decreasing impedance modulus as the anodic potential was progressively raised. In particular even at 2 V the Bode shows at low frequency a resistive plateau which was not present for the system at the OCP. This result comes from the lower resistance attributed to the coating and so also the decrease of the phase angle at low frequency belongs to this phenomenology. More interesting but less clear is the increase of the impedance modulus at middle frequency as the voltage is raised. Looking at the phase angle it is quite clear to assign a prevalently capacitive nature to the improved impedance, as the phase angle reaches values higher than -80°. Based on that it is possible to speculate the formation of corrosion products probably constituted by TiBr4, however, further analysis exploiting AES or XPS techniques are required to fully demonstrate the last sentence.

5.5 SEM and XRD

It was decided to investigate the morphology and the structure with SEM and XRD of the four samples that had shown the lowest corrosion rates during the immersion test and the sample 45A-50C-5R-10%-20 Hz which has the highest corrosion rates (6,42 mm/year) in order to see the differences between their oxide coatings.
From figures 5.35, 5.38, 5.41, and 5.44 it is possible to observe that the morphology of the oxide layer, of the samples 55A-40C-5R-5%-20 Hz 55A-40C-5R-5%-1000 Hz, is very complex with respect to the morphology of the samples 45A-50C-5R-2%-1000 Hz and 45A-50C-5R-5%-1000 Hz, which is more homogeneous and typical of anodizing in sulphuric acid. The morphology of the samples 55A-40C-5R-5%-20 Hz 55A-40C-5R-5%-1000 Hz shows strips of loose oxide that closes the surrounding pores. As has been shown from previous studies, mentioned in chapter 2, discharges predominantly occur during the anodic cycle. Noting also the fact that the structure of the 55A-40C-5R-5%-20 Hz specimen has more molten oxide than the same cycle at 1000Hz it is, therefore, possible to hypothesize that, as the anodic polarization holding time increases, the temperature and pressure of the molten oxide in the channels also increases. Then, thanks to the use of hybrid cycle allowing a rest time between anodic and cathodic polarization, the oxide has time to solidify forming complex structures that occupy nearby pores. Looking at the XRD analysis (figures 5.37, 5.40, 5.43, and 5.46) it is possible to see that: the first sample has the more thick coating due to low amount of pure titanium (substrate) detected, and it is mainly composed by rutile, the second sample has a composition of the coating quite different due to an higher amount of anatase and a thinner oxide layer with respect to the first, the third and the fourth coating have a similar phase content between them and lower oxide thickness due to an higher amount of pure titanium detected.
The sample 45A-50C-5R-5%-1000 Hz shows a structure with a slight increase in closed pores compared to the anodized sample with the same cycle with a cathodic peak of 2%. This is probably due to higher cathodic currents which keep the coating temperature high, thus promoting, during the anodic polarization, the expulsion of molten oxide from the pores which will subsequently solidify.
The sample 45A-50C-5R-10%-20 Hz shows a oxide with very small pores probably related to a reduced spark intensity, as evidenced by the low level of crystallinity achieved by the two XRD peaks of anatase and rutile.

5.5.1 55A-40C-5R-5%-20 Hz

The first sample analyzed by SEM and XRD is the 55A-40C-5R-5%-20 Hz.
In the figures 5.35 and 5.36 we can see its surface at 5000X and 25000X, respectively. This sample shows a very complex oxide structure with nodular block of melted matter randomly deposited over the layer.
From XRD analysis (figure 5.37) we can observe that the coating is composed mainly of rutile with a small quantity of anatase.

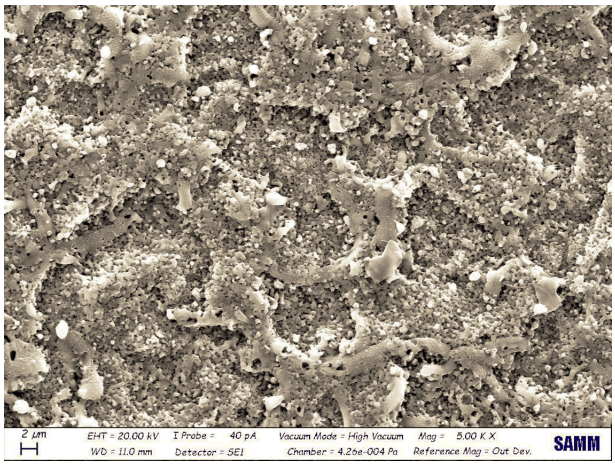

Figure 5.35: SEM image at 5000X

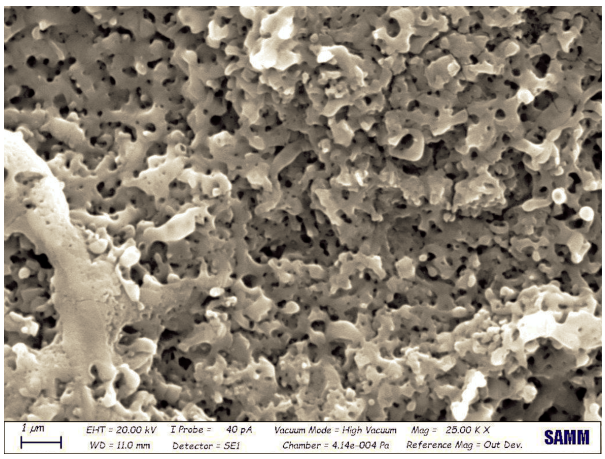

Figure 5.36: SEM image at 25000 X

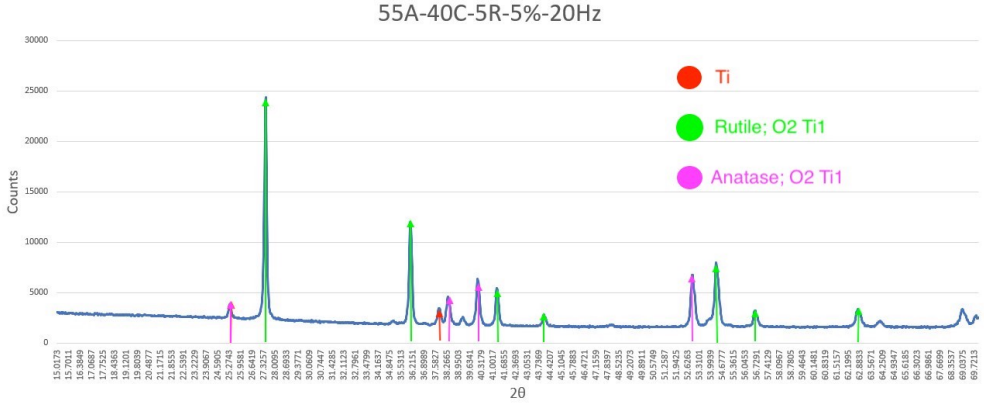

Figure 5.37: XRD

5.5.2 55A-40C-5R-5%-1000 Hz

The second sample analyzed by SEM and XRD is the 55A-40C-5R-5%-1000 Hz. In the figures 5.38 and 5.39 we can see its surface at 5000X and 25000X, respectively. This sample shows a complex oxide structure, but less complex and apparently with a lower roughness than the sample 55A-40C-5R-5%-20 Hz.
From XRD analysis (figure 5.40) we can observe that the coating is composed mainly of rutile. However, a higher amount of pure titanium and anatase was found with respect to the same sample anodized at 20Hz.

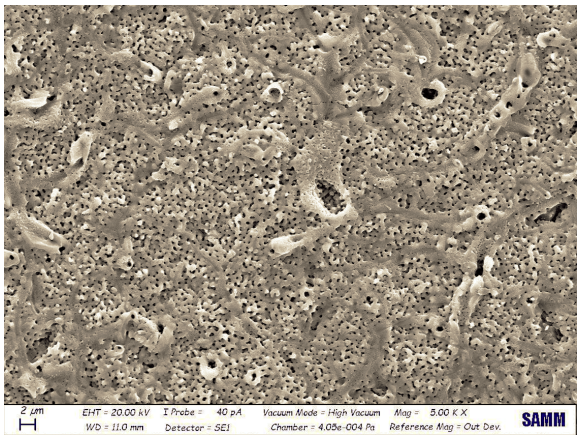

Figure 5.38: SEM image at 5000X

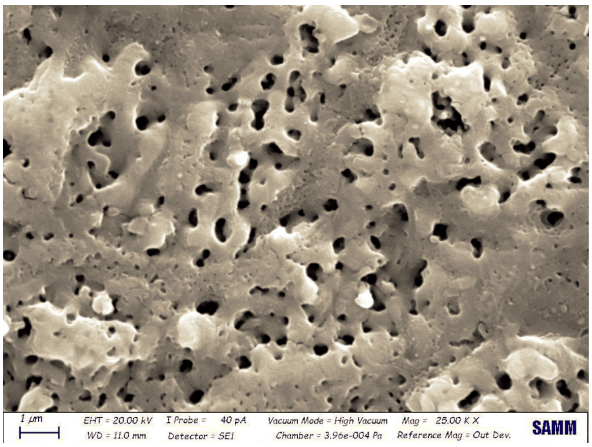

Figure 5.39: SEM image at 25000 X

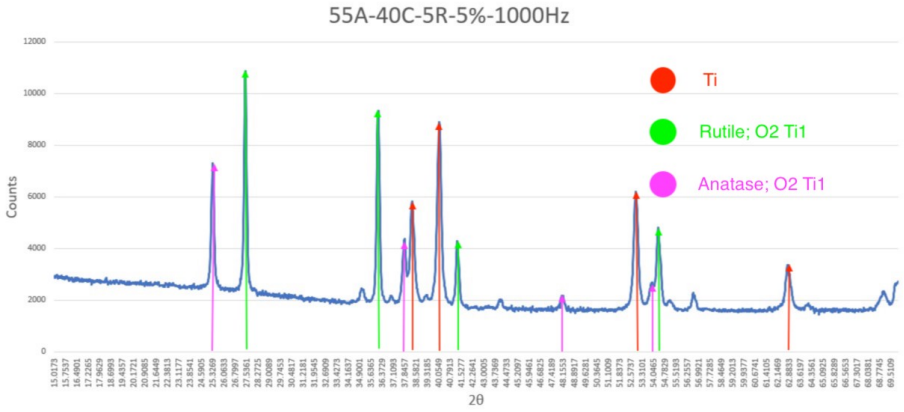

Figure 5.40: XRD

5.5.3 45A-50C-5R-2%-1000 Hz

The third sample analyzed by SEM and XRD is the 45A-50C-5R-2%-1000 Hz.
In the figures 5.41 and 5.42 we can see its surface at 5000X and 25000X, respectively.
This sample shows a homogeneous oxide structure.
From XRD analysis (figure 5.43) we can observe that the coating is composed mainly of rutile with a small quantity of anatase. A high amount of pure titanium has been found. This is the common porous morphology encountered during titanium anodizing in sulphuric acid.

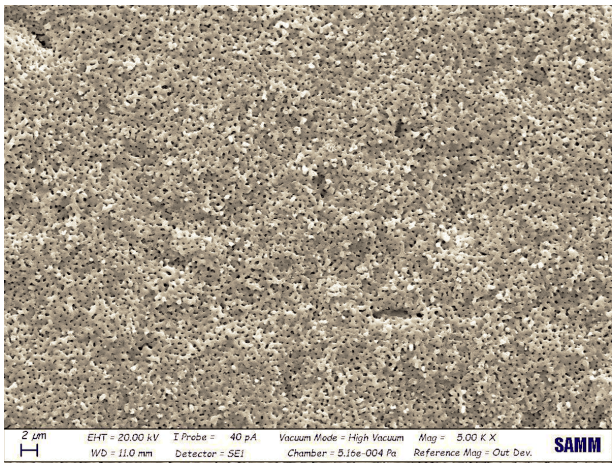

Figure 5.41: SEM image at 5000X

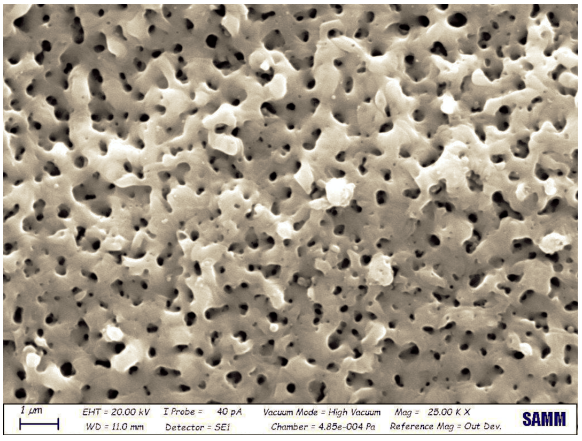

Figure 5.42: SEM image at 25000 X

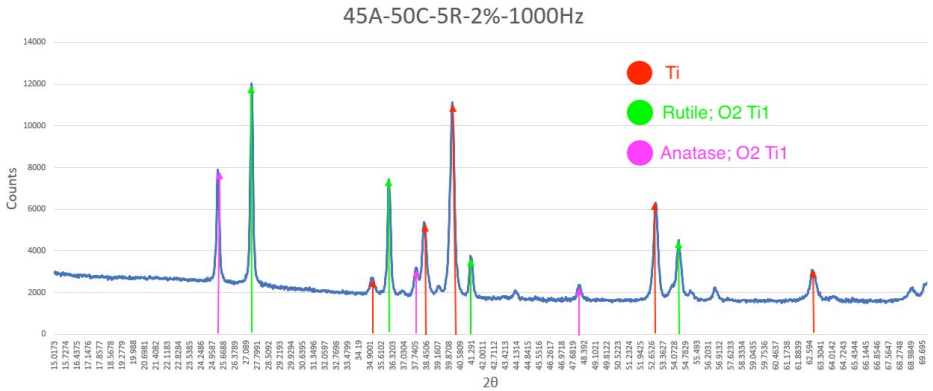

Figure 5.43: XRD

5.5.4 45A-50C-5R-5%-1000 Hz

The fourth sample analyzed by SEM and XRD is the 45A-50C-5R-5%-1000 Hz.
In the figures 5.44 and 5.45 we can see its surface at 5000X and 25000X, respectively.
This sample shows the same morphology, with a slight increase in closed pores, than the sample 45A-50C-5R-2%-1000 Hz.
From XRD analysis (figure 5.46) we can observe that the same amount of rutile was found (with respect to the same sample anodized with 2% of cathodic peak), but a higher amount of anatase and a small amount of pure titanium has been detected.

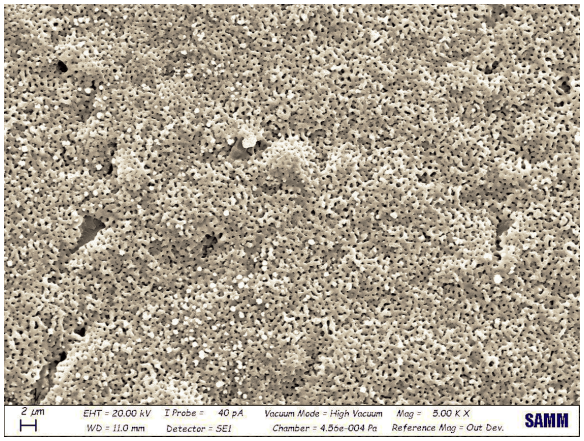

Figure 5.44: SEM image at 5000X

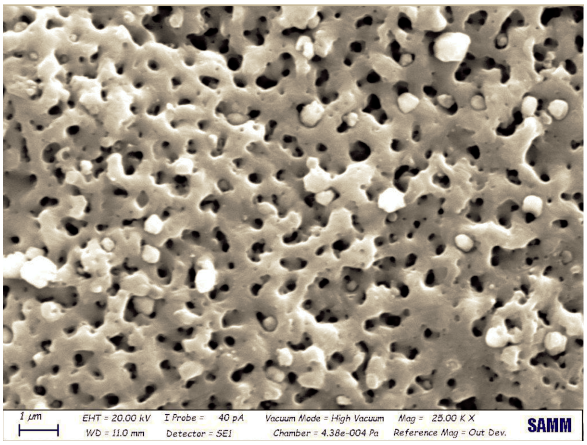

Figure 5.45: SEM image at 25000X

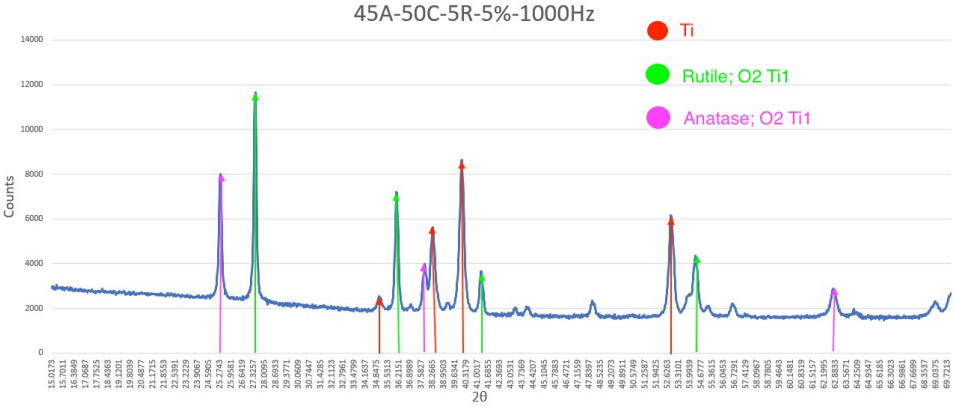

Figure 5.46: XRD

5.5.5 45A-50C-5R-10%-20 Hz

The last sample analyzed by SEM and XRD is the 45A-50C-5R-10%-20 Hz which showed a very high value of corrosion rate during immersion test.
The differences with the previous coatings are evident: the porous oxide layer has a very small pores (figures 5.47 and 5.48) probably related to a reduced spark intensity, as evidenced by the low level of crystallinity achieved by the two XRD peaks of anatase and rutile, as can be seen from figure 5.49. The high amount of pure titanium detected suggest a low oxide thickness.

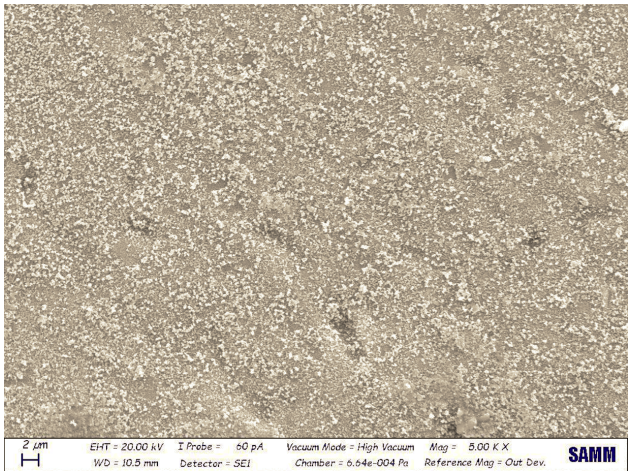

Figure 5.47: SEM image at 5000X

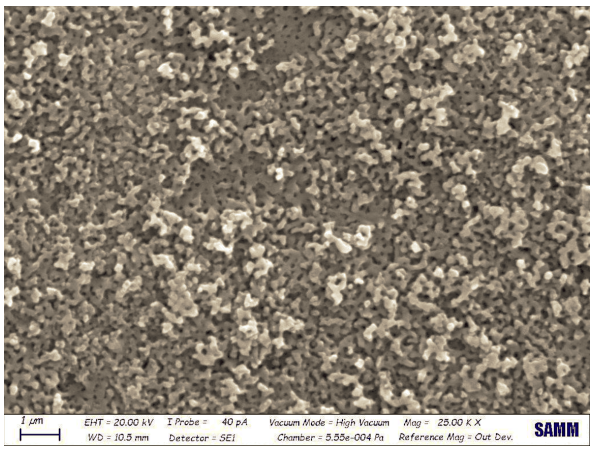

Figure 5.48: SEM image at 25000X

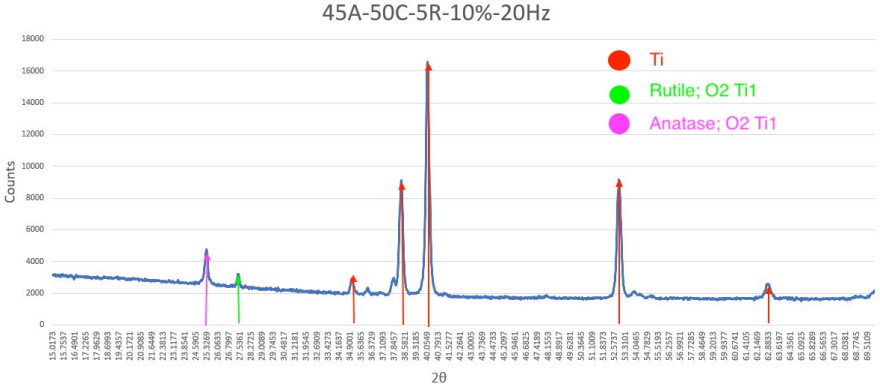

Figure 5.49: XRD

5.6 Porosity

To better understand the quality of the coating, the porosity has been analyzed, starting from SEM images at 25000X, using the program ImageJ.
For each sample the average dimension of pores (figure 5.50) and the density of pores (figure 5.51) have been found. In the figures 5.52, 5.53, 5.54, and 5.55 the images after the binary transformation (left) and the original SEM images (right) are showed.
As shown in other studies, as the temperature increases, the pore size increases. The cathodic current generally contributes to the increase in temperature and therefore to an increase in the size of the pores; in fact, the sample 45A-50C-5R-5%-1000 Hz shows the highest average pore diameter, which is higher than 45A-50C-5R-2%-1000 Hz, which is, in turn, higher than the average pore diameter of 55A-40C-5R-5%-20 Hz and 55A-40C-5R-5%-1000 Hz samples.
As the frequency increases, the pore size does not change significantly.
However, an increase in frequency seems to give rise to a lower pore density in the samples 55A-40C-5R-5% even if it is difficult to evaluate this effect from a single image: it would be necessary to perform the analysis on multiple images at 25000X magnification to have a repeatability of results. In this case probably the magnification at 25000X of the sample 55A-40C-5R-5%-1000 Hz was done where there was the molten oxide expelled from the pores.
The difference in pore density, between samples 45A-50C-5R-2%-1000 Hz and 45A-50C-5R-5%-1000 Hz, can be justified by the fact that in the second sample the pores are partially closed and therefore not analyzed by the process.

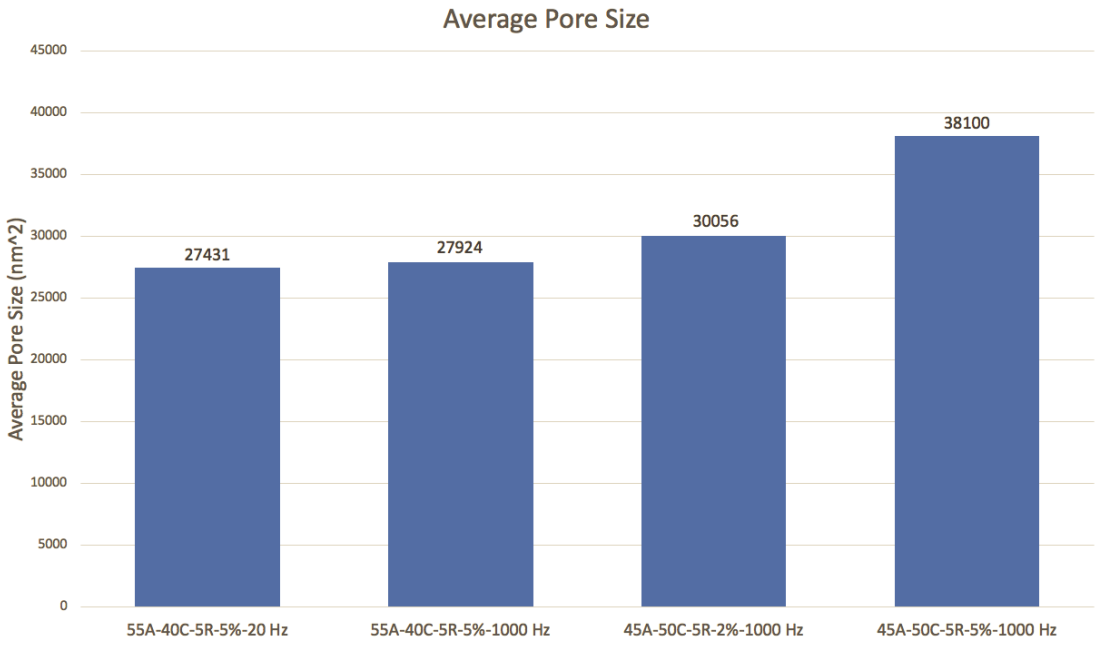

Figure 5.50: Average dimension of pores

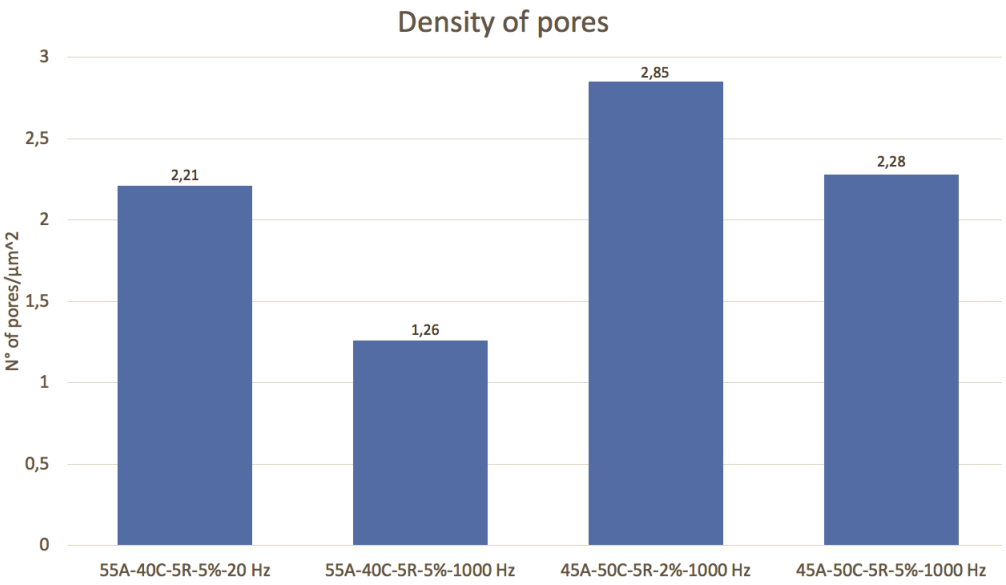

Figure 5.51: Density of pores

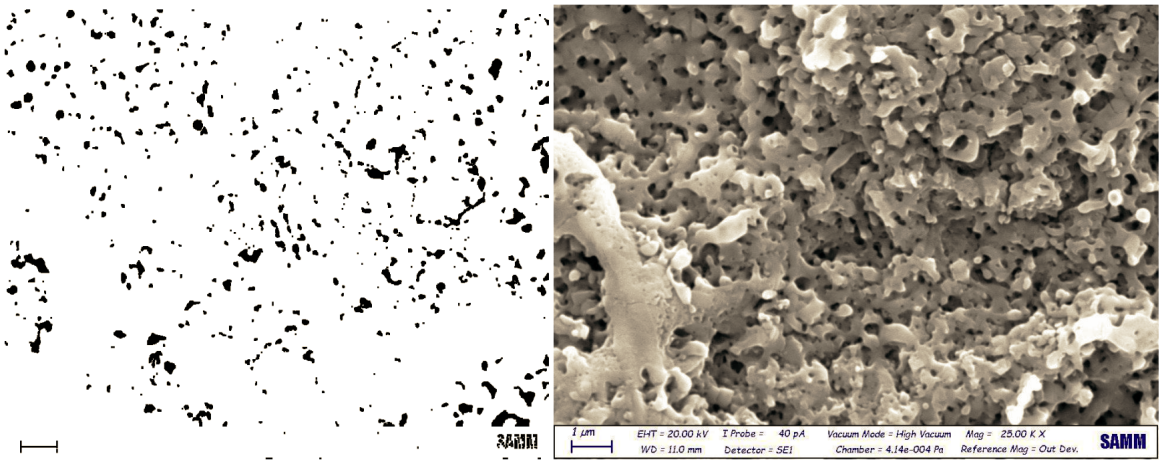

Figure 5.52: ImageJ analysis of sample 55A-40C-5R-5%-20 Hz

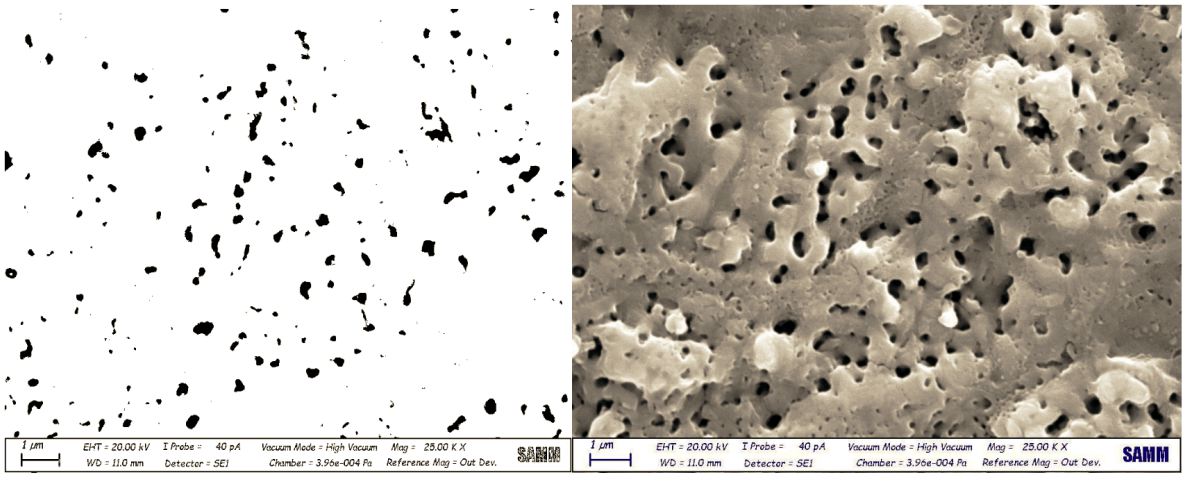

Figure 5.53: ImageJ analysis of sample 55A-40C-5R-5%-1000 Hz

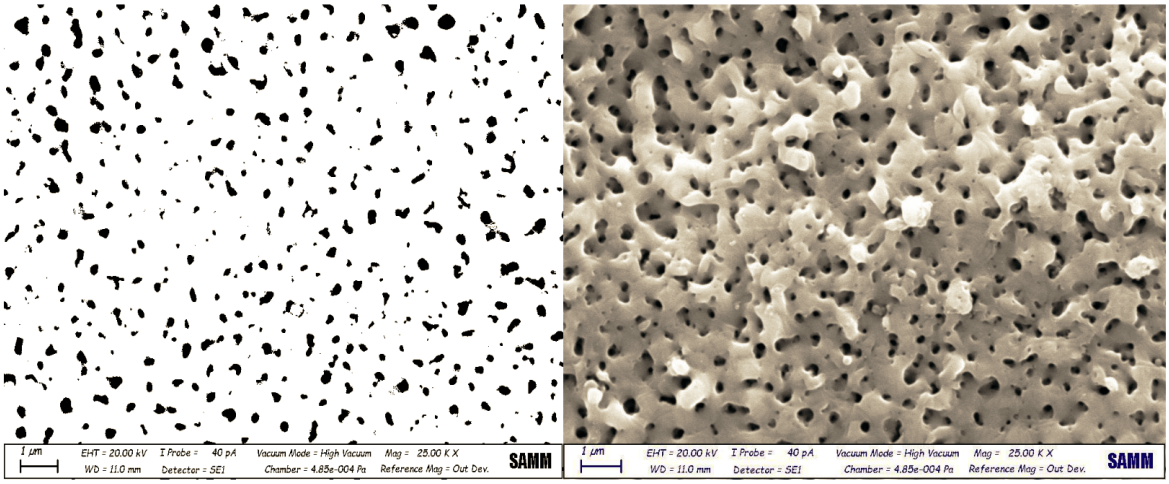

Figure 5.54: ImageJ analysis of sample 45A-50C-5R-2%-1000 Hz

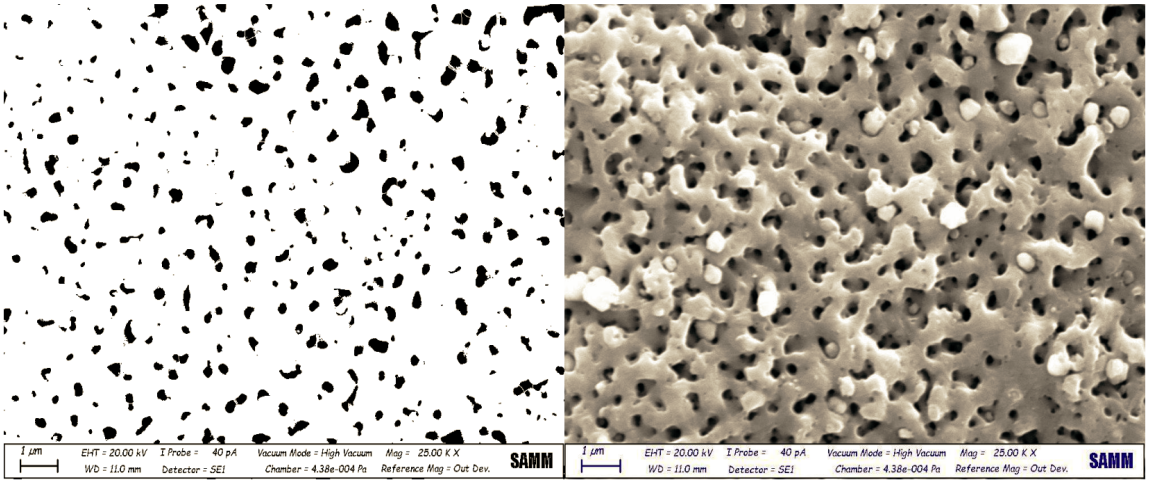

Figure 5.55: ImageJ analysis of sample 45A-50C-5R-5%-1000 Hz

5.7 EIS

Electrochemical impedance spectroscopy was performed in H_2SO_4 0.5 M solution. It was decided to analyze the titanium grade 2 non-anodized and the sample that showed the best corrosion resistance during immersion test (55A-40C-5R-5%-1000Hz) in H_2SO_4 0.5 M solution.
In the circuits proposed , constant phase element (CPE) were employed to represent capacitance elements instead of pure capacitors to take into account any deviation from ideality that could be observed in the capacitive response of the systems. The non-anodized titanium grade 2 has been polished with silicon carbide paper grade 100 and 320 to expose pure titanium to the solution. For the titanium grade 2 non-anodized, the circuit showed in figure 5.56 has been used, in which the R_s is the uncompensated resistance which contains the values of the resistances of the cables, of the contacts and of the electrolyte, $R_{barrierlayer}$ and $CPE_{barrierlayer}$ are the resistance and the constant phase element of the barrier layer naturally formed on top of the metal. $R_{barrierlayer}$ contains the contribution of $R_{chargetransfer}$ while $CPE_{barrierlayer}$ contains the contribution of $CPE_{doublelayer}$.

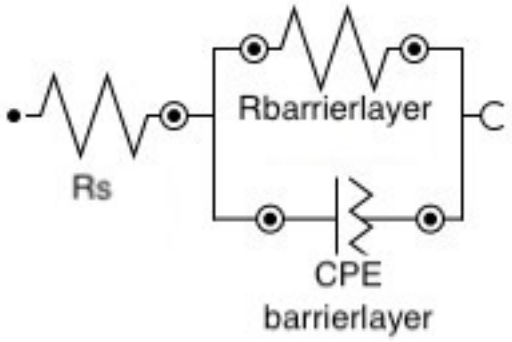

Figure 5.56: Circuit used for the titanium grade 2 non-anodized

EIS were performed at different immersion times (2, 5, 7, 48 hours) and the impedance tests were performed at the value of the ocp of the system (figure 5.57).

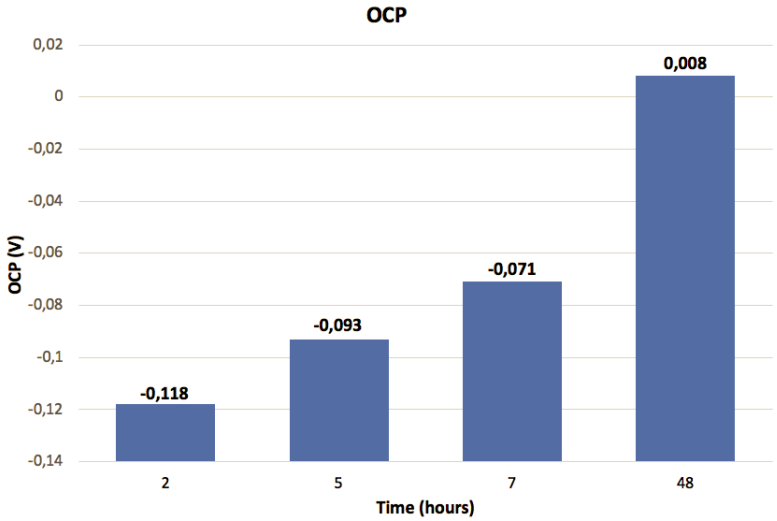

Figure 5.57: OCP trend of titanium grade 2 non-anodized.

The Nyquist plot, Bode Modulus, and Bode Phase are reported in figures 5.58, 5.59, 5.60

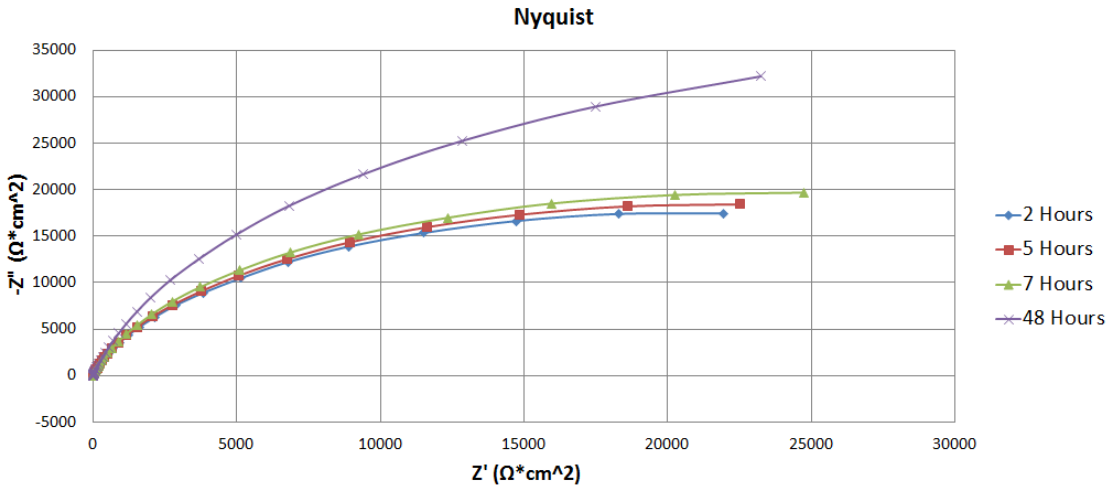

Figure 5.58: Nyquist diagram of titanium grade 2 non-anodized.

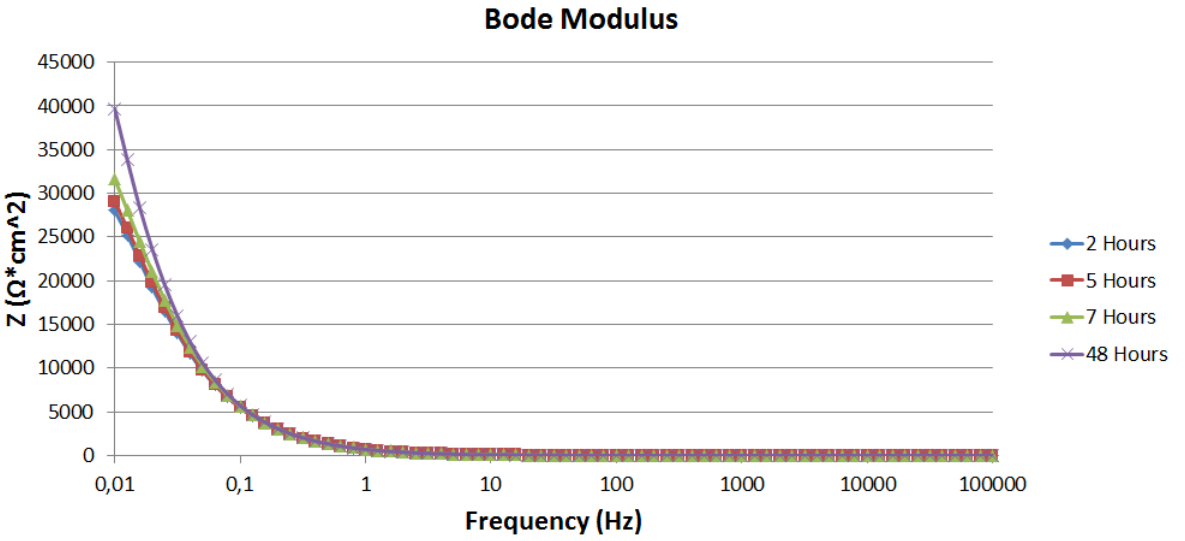

Figure 5.59: Bode Modulus of titanium grade 2 non-anodized.

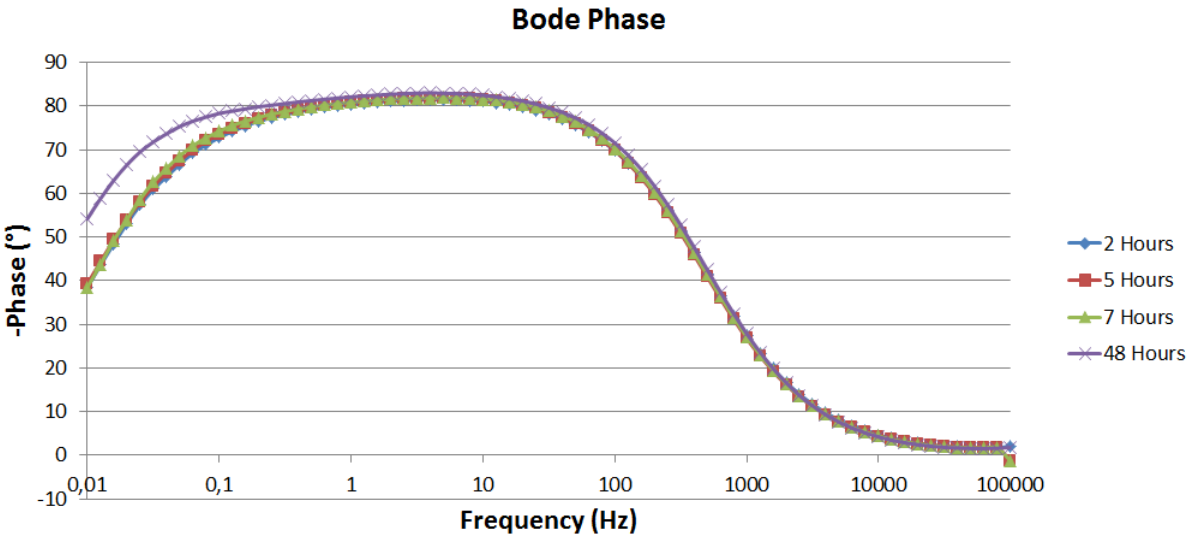

Figure 5.60: Bode Phase of titanium grade 2 non-anodized.

As the immersion time passes, the phase angle increases and the impedance values increase; this means that the coating improves but still does not behave like an ideal coating (angle = -90 °). The values of Y0 and N of the $CPE_{barrierlayer}$ are reported in table 5.3

Table 5.3: Values of Y0 and N of the $CPE_{barrierlayer}$

Time	Y0 (μMho*s^N)	N
2 hours	76.167	0.90836
5 hours	76.31	0.91366
7 hours	73.654	0.91651
48 hours	74.246	0.92306

From the fitting of the circuit, the values of resistance and capacitance of the barrier layer have been found and reported in figures 5.61 and 5.62. The capacity was

obtained using the parameters of the CPE (Y0 and N) through the Brug formula:

$$C = Y0(R_s^{(1-N)})^{\frac{1}{N}} \tag{5.1}$$

The increase of the electrical resistance and of the OCP over time and the decrease of the capacitance is probably related to the oxide growth.
Therefore, by immersing the pristine titanium grade two non-anodized in a solution containing 0.5 M H_2SO_4, the metal oxidizes and a "stable" oxide is formed.

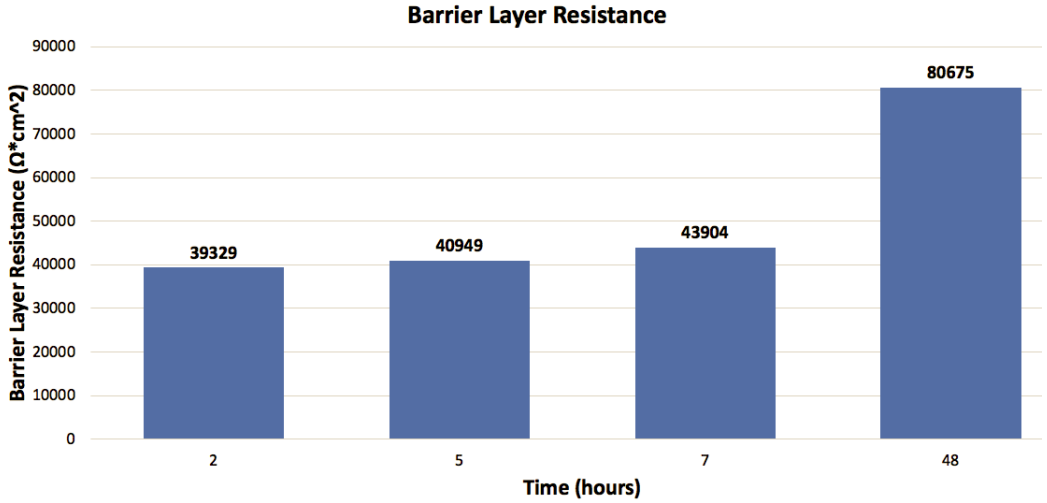

Figure 5.61: Resistance of the barrier layer of titanium grade 2 non-anodized

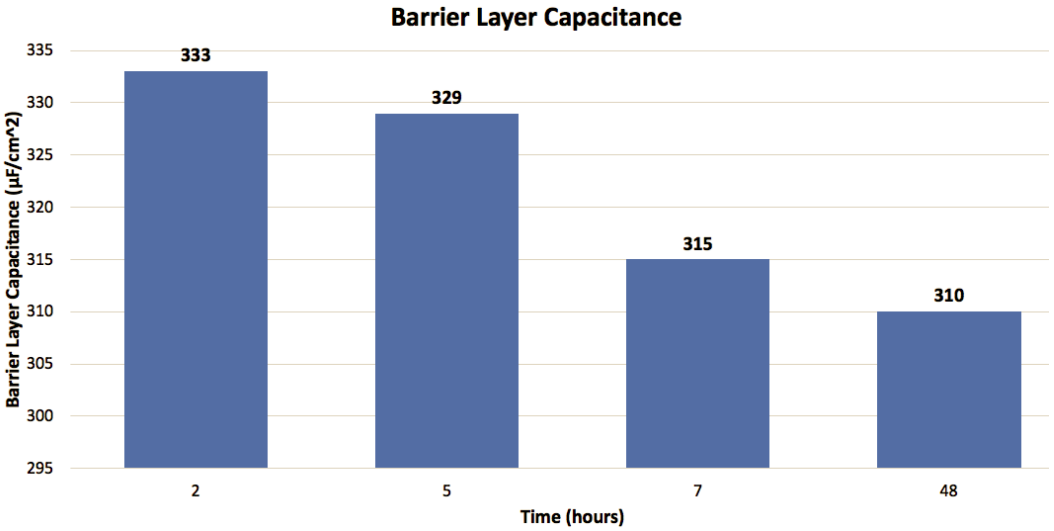

Figure 5.62: Capacitance of the barrier layer of titanium grade 2 non-anodized

For the sample 55A-40C-5R-5%-1000 HZ the circuit (Randle circuit) showed in figure 5.63 has been used, in which the R_s is the resistance of the system, $R_{barrierlayer}$ and $CPE_{barrierlayer}$ are the resistance and the constant phase element of the barrier layer, the $R_{porouslayer}$ and $CPE_{porouslayer}$ are the resistance and the constant phase element of the porous layer (typical of anodized titanium).

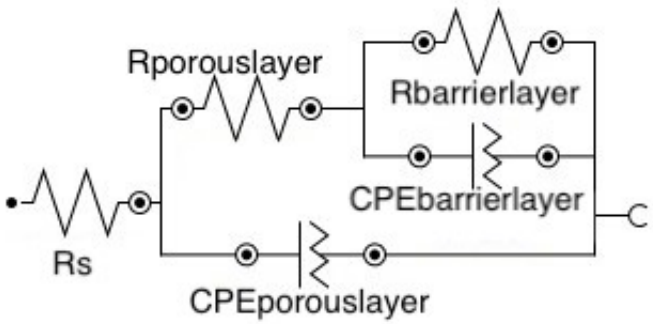

Figure 5.63: Circuit used for the sample 55A-40C-5R-5%-1000 HZ.

EIS were performed at different times (1, 4, 19, 24 hours) and the impedance tests were performed at the value of the ocp of the system (figure 5.64).

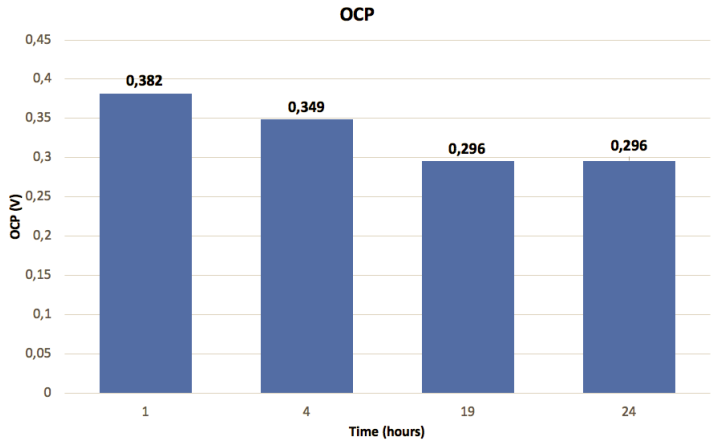

Figure 5.64: OCP trend of the sample 55A-40C-5R-5%-1000 HZ.

The Nyquist plot, Bode Modulus, and Bode Phase are reported in figures 5.65, 5.66, and 5.67.

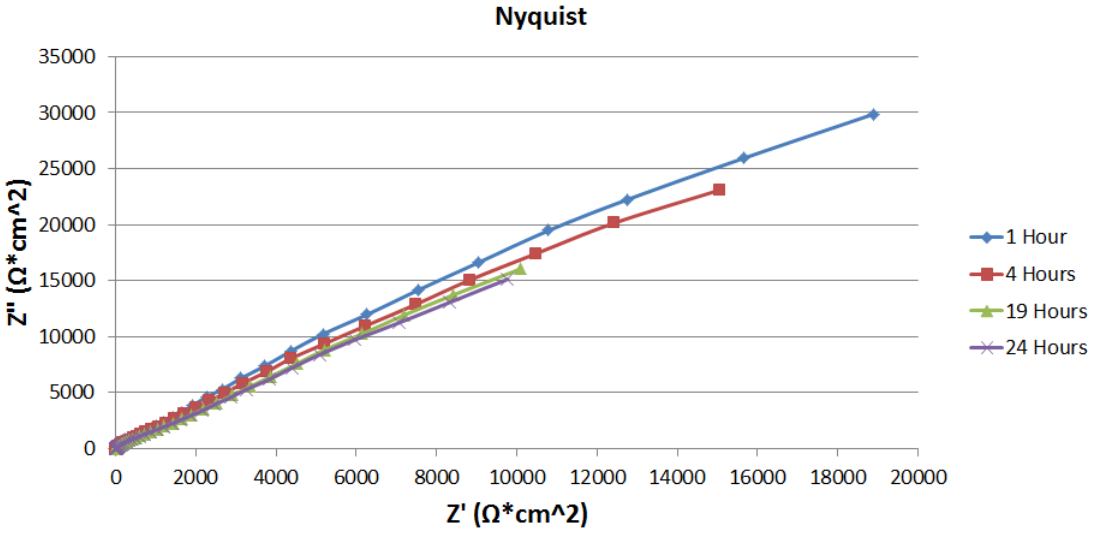

Figure 5.65: Nyquist diagram of the sample 55A-40C-5R-5%-1000 HZ.

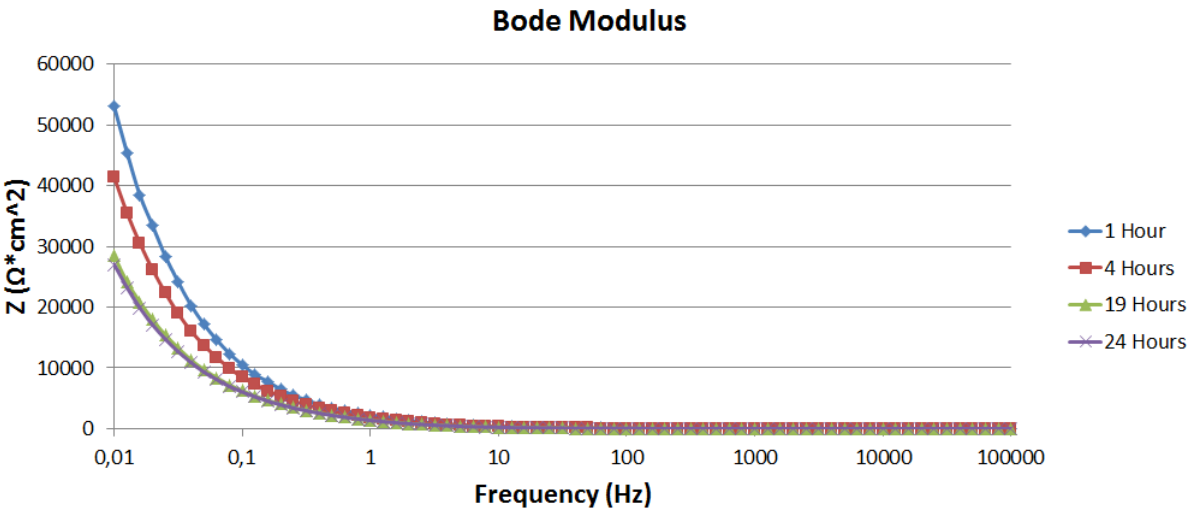

Figure 5.66: Bode Modulus of the sample 55A-40C-5R-5%-1000 HZ.

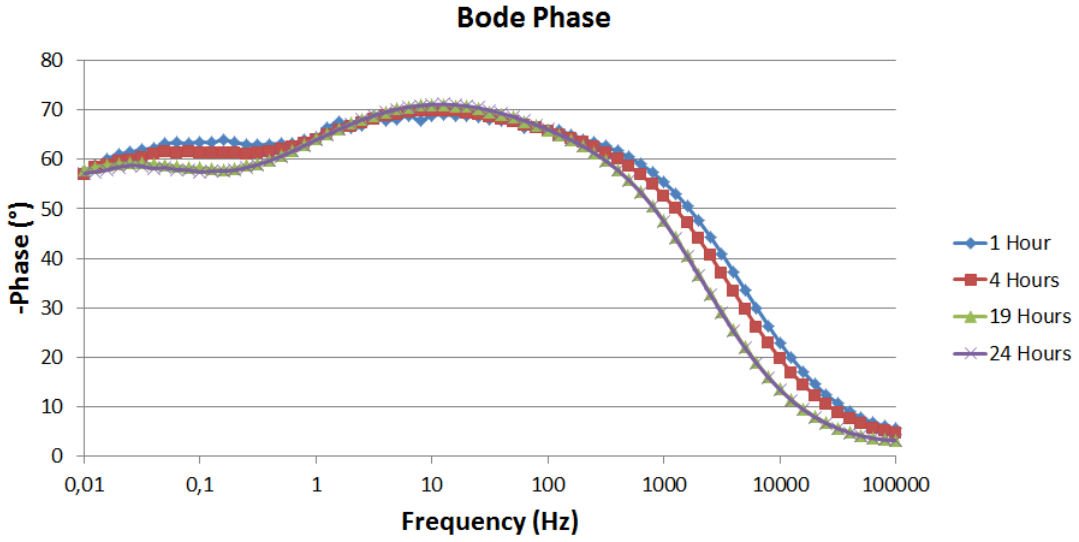

Figure 5.67: Bode Phase of the sample 55A-40C-5R-5%-1000 HZ.

As increasing immersion time, the phase angle decreases and the impedance values decrease; this means that the coating worsens. The values of Y0 and N of the $CPE_{barrierlayer}$ and $CPE_{porouslayer}$ are reported in table 5.4. It can be seen that the N values are lower (more distant from 1) than non-anodized sample because the oxide originated from PEO treatment is more porous.

Table 5.4: Values of Y0 and N of the $CPE_{barrierlayer}$ and $CPE_{porouslayer}$

Time	Y0 porous (μMho*s^N)	N porous	Y0 barrier (μMho*s^N)	N barrier
1 hour	44.187	0.77891	19.466	0.76389
4 hours	53.488	0.78058	30.002	0.76961
19 hours	65.026	0.8011	60.549	0.73853
24 hours	66.185	0.80235	64.757	0.7327

From the fitting of the circuit, the values of resistance and capacitance of the barrier layer and the porous layer have been found and reported in figures 5.68, 5.70,

5.69, and 5.71, respectively.
The resistance of the oxide (and the ocp) decreases over time because the penetration through the pores of the electrolyte increases, thus increasing the conductivity. The oxide capacity increases because new surfaces are created due to corrosion; moreover, with the penetration of the electrolyte, the dielectric constant of the oxide-electrolyte system increases, thus increasing the capacity.

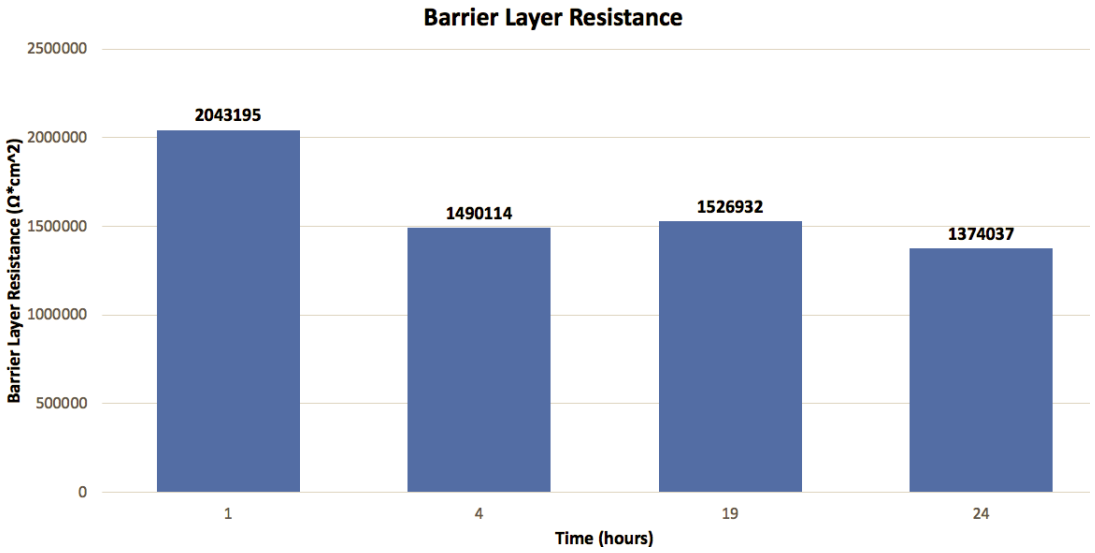

Figure 5.68: Resistance of the barrier layer of the sample 55A-40C-5R-5%-1000 HZ.

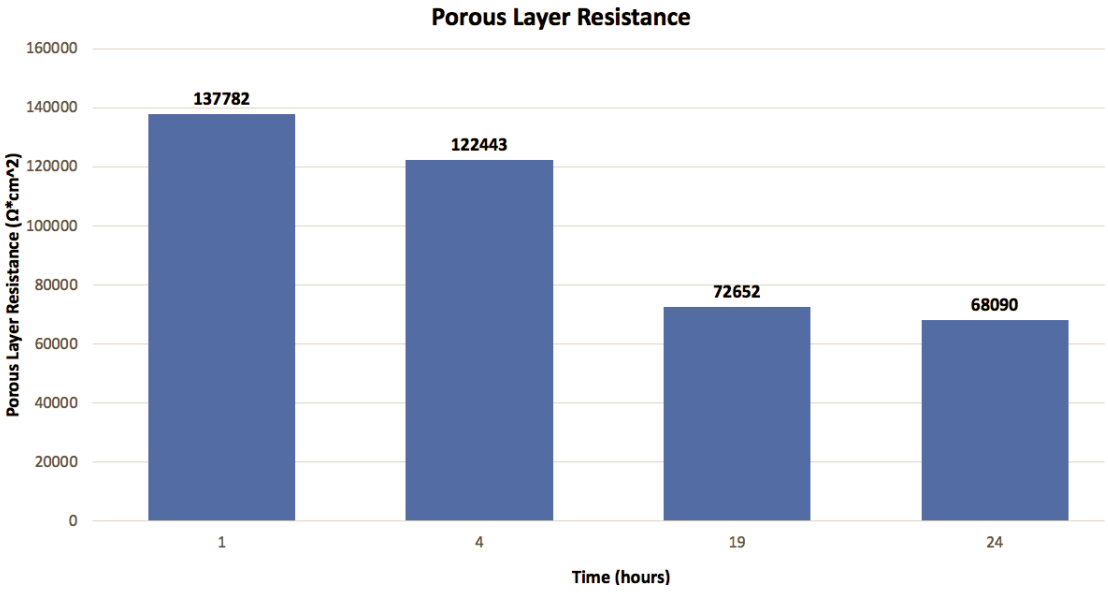

Figure 5.69: Resistance of the porous layer of the sample 55A-40C-5R-5%-1000 HZ.

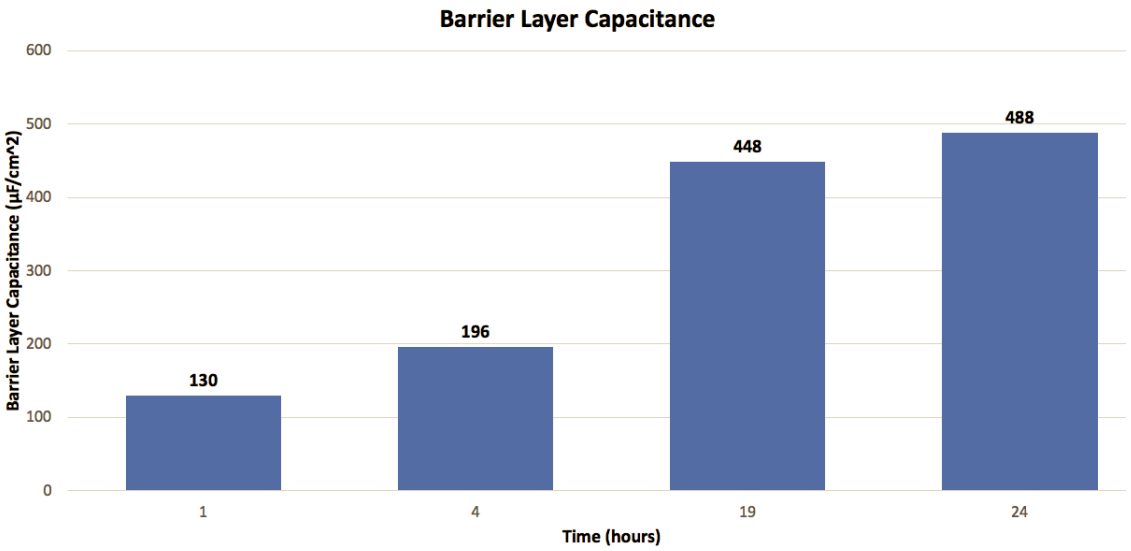

Figure 5.70: Capacitance of the barrier layer of the sample 55A-40C-5R-5%-1000 HZ.

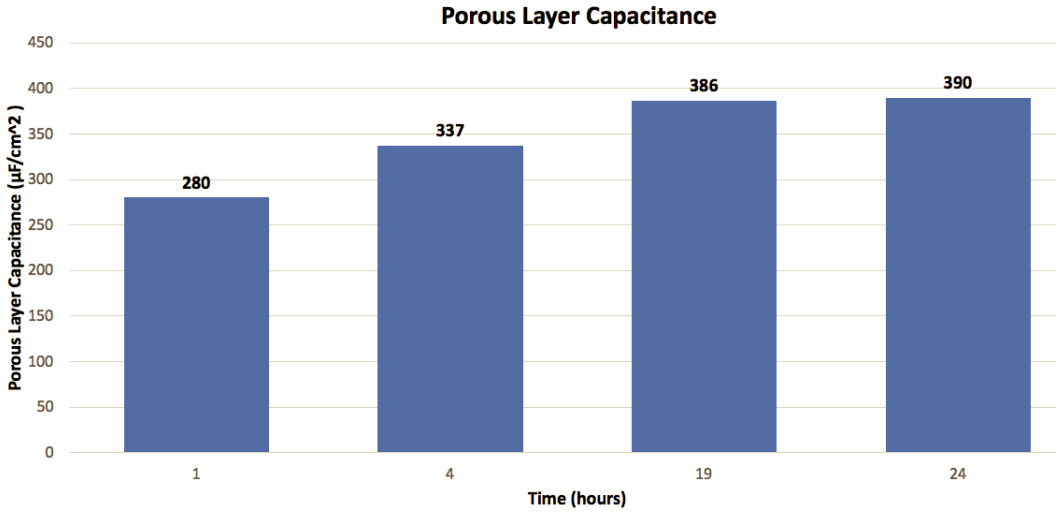

Figure 5.71: Capacitance of the porous layer of the sample 55A-40C-5R-5%-1000 HZ.

Chapter 6

Conclusion

The main object of this research is the application of a Plasma Electrolytic Oxidation (PEO) process on titanium grade 2, to understand the influence of the hybrid duty cycle on the structural, chemical, and morphological characteristics of its oxide. The goal was to achieve an improvement in corrosion resistance of titanium grade 2 through the anodizing process.

The anodization tests were carried out in a 0.5 M solution of sulfuric acid at room temperature with the following parameters: 160 V as forming voltage, with a slope of 0.5 V/s, two frequencies (20 Hz and 1000 Hz) and a cathodic peaks at 2%, 5%, 7%, 10%. The selected cycles were 55A-40C-5R and 45A-50C-5R: they were chosen because, after the treatment, they showed an opaque oxide (index of high thickness).
The voltage trend suggest that probably a "soft spark" condition is reached in samples 55A-40C-5R-5%-1000 Hz and 45A-50C-5R-5%-1000 Hz.

The corrosion behavior of the samples was evaluated by immersion test and by anodic and cathodic potentiodynamic tests. The immersion test was performed in a solution containing H_2SO_4 10% in volume at 60 °C. Four duty cycles (55A-40C-5R-5%-20 Hz, 55A-40C-5R-5%-1000 Hz, 45A-50C-5R-2%-1000 Hz, and 45A-50C-5R-5%-1000 Hz) showed a very low corrosion rate, less than 0.1 mm/year.
The cathodic polarization tests have been carried out on these samples. The one that shows the higher OCP (V) is the 55A-40C-5R-5%-1000 Hz, while the one with the lowest oxygen and hydrogen limiting currents is the 55A-40C-5R-5%-20 Hz.
The anodic polarization was carried out only on the sample 55A-40C-5R-5%-1000 Hz, which exhibits the lower corrosion rate in the immersion test. During the anodic polarization 4 EIS were carried out at OCP, 2, 4 and 6 volt. The pitting potential was 6.4 V.
SEM analysis shows that anodizing with high anodic polarization holding time (samples 55A-40C-5R-5%-20 Hz and 55A-40C-5R-5%-1000 Hz) generates a more complex structure due to the fact that the discharges predominantly occur during the anodic cycle. The molten oxide reaches high temperature and high pressure inside the channels and after solidifies, especially in the rest time, forming complex structures that occupy nearby pores. Instead the samples 45A-50C-5R-2%-1000 Hz and 45A-50C-5R-5%-1000 Hz have a microstructure typical of classical anodizing with higher porosity.
The crystal structure was analyzed with XRD. This analysis shows that specimens

55A-40C-5R-5%-20 Hz and 55A-40C-5R-5%-1000 Hz have probably grater thickness than specimens 45A-50C-5R-2%-1000 Hz and 45A-50C-5R-5%-1000 Hz ,even if, further more specialized analysis are required to demonstrate this sentence. More rutile is present in the first two samples.
EIS analysis was performed on titanium grade 2 non-anodized and on sample 55A-40C-5R-5%-1000 Hz. EIS on titanium grade 2 non-anodized shows that an oxide layer (monolayer) is forming with time in a solution containing H_2SO_4 0.5 M. EIS on sample 55A-40C-5R-5%-1000 Hz shows that the oxide formed with PEO technique has a double layer structure (barrier layer + porous layer) and during time the oxide undergoes electrolyte absorption due to the porous morphology typical of PEO coatings. The double layer structure was also confirmed by EIS analysis carried out during anodic polarization test. During the test the coating resistance decreases with the increasing of pitting potential (and with increasing of the immersion time). The phase angle demonstrates the decreased protectiveness of the coating as the voltage is raised but also the formation of a layer probably composed by corrosion products, allowing for an increased impedance at middle frequencies.

Bibliography

[1] Christoph Leyens and Manfred Peters. *Titanium and titanium alloys: fundamentals and applications*. John Wiley & Sons, 2003.

[2] Encyclopædia Britannica. "Titanium". In: (2019).

[3] Rebecca Janisch, Priya Gopal, and Nicola A Spaldin. "Transition metal-doped TiO2 and ZnO—present status of the field". In: *Journal of Physics: Condensed Matter* 17.27 (2005), R657.

[4] Ulrike Diebold. "The surface science of titanium dioxide". In: *Surface science reports* 48.5-8 (2003), pp. 53–229.

[5] Steven Dutch. "Rutile structure". In: *Natural and Applied Science* ().

[6] Linus Pauling and James H Sturdivant. "XV. The crystal structure of brookite". In: *Zeitschrift für Kristallographie-Crystalline Materials* 68.1-6 (1928), pp. 239–256.

[7] Pietro Pedeferri. *Corrosion science and engineering*. Springer, 2018.

[8] *General Attacck Corrosion*. `https://www.nace.org/General-Attack-Corrosion/`.

[9] Davide Prando et al. "Corrosion of titanium: Part 1: Aggressive environments and main forms of degradation". In: *Journal of applied biomaterials & functional materials* 15.4 (2017), e291–e302.

[10] Khalid SE Al-Malahy and T Hodgkiess. "Comparative studies of the seawater corrosion behaviour of a range of materials". In: *Desalination* 158.1-3 (2003), pp. 35–42.

[11] HB Bomberger, PJ Cambourelis, and GE Hutchinson. "Corrosion properties of titanium in marine environments". In: *Journal of the Electrochemical Society* 101.9 (1954), pp. 442–447.

[12] Julia van Drunen, Baodong Zhao, and Gregory Jerkiewicz. "Corrosion behavior of surface-modified titanium in a simulated body fluid". In: *Journal of materials science* 46.18 (2011), pp. 5931–5939.

[13] Rahul Bhola et al. "Corrosion in titanium dental implants/prostheses–a review". In: *Trends Biomater Artif Organs* 25.1 (2011), pp. 34–46.

[14] Roberto Chiesa et al. "In vitro and in vivo performance of a novel surface treatment to enhance osseointegration of endosseous implants". In: *Oral Surgery, Oral Medicine, Oral Pathology, Oral Radiology, and Endodontology* 103.6 (2007), pp. 745–756.

[15] DW Shoesmith, JJ Noël, and VE Annamalai. "Corrosion of titanium and its alloys". In: (2016).

[16] Masaharu Nakagawa et al. "Effect of fluoride concentration and pH on corrosion behavior of titanium for dental use". In: *Journal of dental research* 78.9 (1999), pp. 1568–1572.

[17] Britta Lindholm-Sethson and BI Ardlin. "Effects of pH and fluoride concentration on the corrosion of titanium". In: *Journal of Biomedical Materials Research Part A: An Official Journal of The Society for Biomaterials, The Japanese Society for Biomaterials, and The Australian Society for Biomaterials and the Korean Society for Biomaterials* 86.1 (2008), pp. 149–159.

[18] Stanisław Lalik, Janusz Cebulski, and Rafał Michalik. "Corrosion resistance of titanium in water solution of hydrochloric acid". In: *Archives of Materials Science and Engineering* 28.6 (2007), pp. 349–352.

[19] Kazuhiro Toba, Koji Kawano, Jun'ichi Sakai, et al. "Corrosion of Carbon Steel and Alloys in Ammonium Chloride Salt". In: *CORROSION 2014*. NACE International. 2014.

[20] F El-Taib Heakal and Kh A Awad. "Electrochemical corrosion and passivation behavior of titanium and its Ti-6Al-4V alloy in low and highly concentrated HBr solutions". In: *Int. J. Electrochem. Sci* 6 (2011), p. 6483.

[21] Bruce D Craig, David S Anderson, et al. *Handbook of corrosion data*. ASM international, 1994.

[22] AZoM. "Titanium - Corrosion by Acids". In: (2002).

[23] Marie Koike and Hiroyuki Fujii. "The corrosion resistance of pure titanium in organic acids". In: *Biomaterials* 22.21 (2001), pp. 2931–2936.

[24] Jing Liu, Akram Alfantazi, and Edouard Asselin. "Effects of Temperature and sulfate on the pitting corrosion of titanium in high-temperature chloride solutions". In: *Journal of The Electrochemical Society* 162.4 (2015), pp. C189–C196.

[25] Donald M Brunette et al. *Titanium in medicine: material science, surface science, engineering, biological responses and medical applications*. Springer Science & Business Media, 2012.

[26] Gerd Lütjering and James C Williams. *Titanium*. Springer Science & Business Media, 2007.

[27] Davide Prando. *Development of surface treatment for increasing corrosion resistance of commercially pure titanium*. 2018.

[28] GS Frankel. "Pitting corrosion of metals a review of the critical factors". In: *Journal of the Electrochemical Society* 145.6 (1998), pp. 2186–2198.

[29] James J Noel. "The electrochemistry of titanium corrosion". In: (1999).

[30] JJ Noël, N Ebrahimi, and DW Shoesmith. "Corrosion of titanium and titanium alloys". In: (2018).

[31] TR Beck. *STRESS CORROSION CRACKING OF TITANIUM ALLOYS PRELIMINARY REPORT ON TI: 8AL-1MO-1V ALLOY AND PROPOSED ELECTROCHEMICAL MECHANISM*. Tech. rep. BOEING SCIENTIFIC RESEARCH LABS SEATTLE WA, 1966.

[32] NG Feige and T Murphy. “Fracture Behavior of Titanium Alloys in Aqueous Environment”. In: (1966).

[33] Benjamin Floyd Brown. *Stress-corrosion cracking in high strength steels and in titanium and aluminum alloys*. Naval Research Laboratory, 1972.

[34] CL Briant, ZF Wang, and N Chollocoop. “Hydrogen embrittlement of commercial purity titanium”. In: *Corrosion Science* 44.8 (2002), pp. 1875–1888.

[35] E Tal-Gutelmacher and D Eliezer. “Hydrogen cracking in titanium-based alloys”. In: *Journal of alloys and compounds* 404 (2005), pp. 621–625.

[36] H-J Christ et al. “Effect of hydrogen on mechanical properties of β-titanium alloys”. In: *Sadhana* 28.3-4 (2003), pp. 453–465.

[37] Fred Hua et al. “Modeling the hydrogen-induced cracking of titanium alloys in nuclear waste repository environments”. In: *JOM* 57.1 (2005), pp. 20–26.

[38] M Jamesh, Satendra Kumar, and TSN Sankara Narayanan. “Effect of thermal oxidation on corrosion resistance of commercially pure titanium in acid medium”. In: *Journal of materials engineering and performance* 21.6 (2012), pp. 900–906.

[39] Hasan Güleryüz and Hüseyin Çimenoğlu. “Effect of thermal oxidation on corrosion and corrosion–wear behaviour of a Ti–6Al–4V alloy”. In: *Biomaterials* 25.16 (2004), pp. 3325–3333.

[40] Satendra Kumar et al. “Surface modification of CP-Ti to improve the fretting-corrosion resistance: Thermal oxidation vs. anodizing”. In: *Materials Science and Engineering: C* 30.6 (2010), pp. 921–927.

[41] Azadeh Ashrafizadeh and Fakhreddin Ashrafizadeh. “Structural features and corrosion analysis of thermally oxidized titanium”. In: *Journal of Alloys and Compounds* 480.2 (2009), pp. 849–852.

[42] Esra Arslan et al. “Influence of surface roughness on corrosion and tribological behavior of CP-Ti after thermal oxidation treatment”. In: *Journal of Materials Engineering and Performance* 19.3 (2010), pp. 428–433.

[43] Satendra Kumar et al. “Thermal oxidation of CP-Ti: Evaluation of characteristics and corrosion resistance as a function of treatment time”. In: *Materials Science and Engineering: C* 29.6 (2009), pp. 1942–1949.

[44] Martina Bruno. *Discontinuous Anodizing Treatment to Increase Commercially Pure Titanium Corrosion Resistance*. 2018.

[45] MARIA VITTORIA Diamanti and MP Pedeferri. “Effect of anodic oxidation parameters on the titanium oxides formation”. In: *Corrosion Science* 49.2 (2007), pp. 939–948.

[46] IA Ammar and I Kamal. “Kinetics of anodic oxide-film growth on titanium—I. Acid media”. In: *Electrochimica Acta* 16.9 (1971), pp. 1539–1553.

[47] Jianhua Liu et al. “Effect of electrolyte concentration on morphology, microstructure and electrochemical impedance of anodic oxide film on titanium alloy Ti-10V–2Fe–3Al”. In: *Journal of Applied Electrochemistry* 40.8 (2010), pp. 1545–1553.

[48] Young-Taeg Sul et al. “The electrochemical oxide growth behaviour on titanium in acid and alkaline electrolytes”. In: *Medical engineering & physics* 23.5 (2001), pp. 329–346.

[49] MARIA VITTORIA Diamanti and Mariapia Pedeferri. “Production and Characterization of Thick Titanium Oxide Films by Anodic Oxidation”. In: (2012).

[50] Tatsuya Kikuchi et al. “Porous aluminum oxide formed by anodizing in various electrolyte species”. In: *Current nanoscience* 11.5 (2015), pp. 560–571.

[51] Il Song Park et al. “Surface characteristics of titanium anodized in the four different types of electrolyte”. In: *Electrochimica Acta* 53.2 (2007), pp. 863–870.

[52] SK Lazarouk et al. “Effect of the electrolyte temperature on the formation and structure of porous anodic titania film”. In: *Thin Solid Films* 526 (2012), pp. 41–46.

[53] Karolina Syrek et al. “Effect of electrolyte agitation on anodic titanium dioxide (ATO) growth and its photoelectrochemical properties”. In: *Electrochimica Acta* 180 (2015), pp. 801–810.

[54] MV Diamanti and MP Pedeferri. “The Anodic Oxidation of Titanium and Its Alloys”. In: (2018).

[55] MARIA VITTORIA Diamanti et al. “Anodic coloring of titanium and its alloy for jewels production”. In: *Color Research & Application* 37.5 (2012), pp. 384–390.

[56] Dah-Shyang Tsai and Chen-Chia Chou. “Review of the soft sparking issues in plasma electrolytic oxidation”. In: *Metals* 8.2 (2018), p. 105.

[57] A Afshar and MR Vaezi. “Evaluation of electrical breakdown of anodic films on titanium in phosphate-base solutions”. In: *Surface and coatings technology* 186.3 (2004), pp. 398–404.

[58] KC Kalra, KC Singh, and Mohinder Singh. “Electrical breakdown of anodic films on titanium in aqueous electrolytes”. In: *Journal of Electroanalytical Chemistry* 371.1-2 (1994), pp. 73–78.

[59] AL Yerokhin et al. “Characterisation of oxide films produced by plasma electrolytic oxidation of a Ti–6Al–4V alloy”. In: *Surface and Coatings Technology* 130.2-3 (2000), pp. 195–206.

[60] Long-Hao Li et al. “Improved biological performance of Ti implants due to surface modification by micro-arc oxidation”. In: *Biomaterials* 25.14 (2004), pp. 2867–2875.

[61] S Gowtham, T Arunnellaiappan, and N Rameshbabu. “An investigation on pulsed DC plasma electrolytic oxidation of cp-Ti and its corrosion behaviour in simulated body fluid”. In: *Surface and Coatings Technology* 301 (2016), pp. 63–73.

[62] Trevor William Clyne and Samuel Christopher Troughton. “A review of recent work on discharge characteristics during plasma electrolytic oxidation of various metals”. In: *International materials reviews* 64.3 (2019), pp. 127–162.

[63] V Srinivasan et al. “Review on Plasma Electrolytic Oxidation of Titanium Coatings”. In: *International Journal of Advanced Research in Biology, Engineering, Science and Technology* 2.1 (2016), pp. 29–34.

[64] Alexandre Nomine et al. “High speed video evidence for localised discharge cascades during plasma electrolytic oxidation”. In: *Surface and Coatings Technology* 269 (2015), pp. 125–130.

[65] SC Troughton et al. “Effect of individual discharge cascades on the microstructure of plasma electrolytic oxidation coatings”. In: *Applied Surface Science* 389 (2016), pp. 260–269.

[66] Ki Ryong Shin, Young Gun Ko, and Dong Hyuk Shin. “Effect of electrolyte on surface properties of pure titanium coated by plasma electrolytic oxidation”. In: *Journal of Alloys and Compounds* 509 (2011), S478–S481.

[67] Flemming Jensen. “High Frequency Pulse Anodising of Aluminium for Decorative Applications”. In: (2019).

[68] E Matykina et al. “Recent advances in energy efficient PEO processing of aluminium alloys”. In: *Transactions of Nonferrous Metals Society of China* 27.7 (2017), pp. 1439–1454.

[69] Qingbiao Li et al. “Effects of cathodic voltages on structure and wear resistance of plasma electrolytic oxidation coatings formed on aluminium alloy”. In: *Applied surface science* 297 (2014), pp. 176–181.

[70] Jun-Hua Wang et al. “Effects of the ratio of anodic and cathodic currents on the characteristics of micro-arc oxidation ceramic coatings on Al alloys”. In: *Applied surface science* 292 (2014), pp. 658–664.

[71] V Jafarniya Kharanagh, MA Faghihi Sani, and E Rafizadeh. “Effect of current frequency on coating properties formed on aluminised steel by plasma electrolytic oxidation”. In: *Surface engineering* 30.3 (2014), pp. 224–228.

[72] Hong-Yuan Wang et al. “PREPARATION AND MECHANISM OF CONTROLLABLE MICROPORES ON BIOCERAMIC TiO 2 COATINGS BY PLASMA ELECTROLYTIC OXIDATION”. In: *Surface Review and Letters* 20.05 (2013), p. 1350051.

[73] ZOU Bin et al. “Effect of current frequency on properties of coating formed by microarc oxidation on AZ91D magnesium alloy”. In: *Transactions of Nonferrous Metals Society of China* 25.5 (2015), pp. 1500–1505.

[74] Julien Martin et al. “Effects of electrical parameters on plasma electrolytic oxidation of aluminium”. In: *Surface and Coatings Technology* 221 (2013), pp. 70–76.

[75] AL Yerokhin et al. “Oxide ceramic coatings on aluminium alloys produced by a pulsed bipolar plasma electrolytic oxidation process”. In: *Surface and Coatings Technology* 199.2-3 (2005), pp. 150–157.

[76] A Yerokhin, EV Parfenov, and A Matthews. “In situ impedance spectroscopy of the plasma electrolytic oxidation process for deposition of Ca-and P-containing coatings on Ti”. In: *Surface and Coatings Technology* 301 (2016), pp. 54–62.

[77] F Jaspard-Mécuson et al. “Tailored aluminium oxide layers by bipolar current adjustment in the Plasma Electrolytic Oxidation (PEO) process”. In: *Surface and Coatings Technology* 201.21 (2007), pp. 8677–8682.

[78] Dawei Gong et al. “Titanium oxide nanotube arrays prepared by anodic oxidation”. In: *Journal of Materials Research* 16.12 (2001), pp. 3331–3334.

[79] JM Macak et al. “Influence of different fluoride containing electrolytes on the formation of self-organized titania nanotubes by Ti anodization”. In: *Journal of electroceramics* 16.1 (2006), pp. 29–34.

[80] Karthik Shankar et al. “Highly-ordered TiO2 nanotube arrays up to 220 μm in length: use in water photoelectrolysis and dye-sensitized solar cells”. In: *Nanotechnology* 18.6 (2007), p. 065707.

[81] Sergiu P Albu et al. “250 μm long anodic TiO2 nanotubes with hexagonal self-ordering”. In: *physica status solidi (RRL)–Rapid Research Letters* 1.2 (2007), R65–R67.

[82] Domenico Regonini et al. “Anodised TiO2 nano-tubes: voltage ramp influence on the nano-structured oxide and investigation of phase changes promoted by thermal treatments”. In: *physica status solidi (a)* 204.6 (2007), pp. 1814–1819.

[83] D Regonini et al. “Anodised titania nanotubes prepared in a glycerol/NaF electrolyte”. In: *Journal of nanoscience and nanotechnology* 9.7 (2009), pp. 4410–4416.

[84] Domenico Regonini et al. “A review of growth mechanism, structure and crystallinity of anodized TiO2 nanotubes”. In: *Materials Science and Engineering: R: Reports* 74.12 (2013), pp. 377–406.

[85] “Immersion test”. In: *Corrosionpedia* (2108).

[86] “anodic polarization”. In: *corrosionpedia* (2020).

[87] DG Enos and LL Scribner. “The Potentiodynamic Polarisation Scan–Technical Report 33”. In: *Solartron Instruments* (1997).

[88] Mark E Orazem and Bernard Tribollet. *Electrochemical impedance spectroscopy*. John Wiley & Sons, 2017.

[89] VF Lvovich. *Impedance Spectroscopy: Applications to Electrochemical and Dielectric Phenomena. 2012*.

[90] MEP Souza, M Ballester, and CMA Freire. “EIS characterisation of Ti anodic oxide porous films formed using modulated potential”. In: *Surface and Coatings Technology* 201.18 (2007), pp. 7775–7780.

[91] MARIA VITTORIA Diamanti et al. “Characterisation of titanium oxide films by potentiodynamic polarisation and electrochemical impedance spectroscopy”. In: *Corrosion engineering, science and technology* 45.6 (2010), pp. 428–434.

[92] Maan Aziz-Kerrzo et al. “Electrochemical studies on the stability and corrosion resistance of titanium-based implant materials”. In: *Biomaterials* 22.12 (2001), pp. 1531–1539.

[93] MJ Esplandiu, EM Patrito, and VA Macagno. "Characterization of hafnium anodic oxide films: an AC impedance investigation". In: *Electrochimica acta* 40.7 (1995), pp. 809–815.

[94] L Gawel et al. "Impedance monitoring of corrosion degradation of plasma electrolytic oxidation coatings (PEO) on magnesium alloy". In: *Journal of Alloys and Compounds* 722 (2017), pp. 406–413.

[95] S Tamilselvi, V Raman, and N Rajendran. "Corrosion behaviour of Ti–6Al–7Nb and Ti–6Al–4V ELI alloys in the simulated body fluid solution by electrochemical impedance spectroscopy". In: *Electrochimica Acta* 52.3 (2006), pp. 839–846.

[96] Brigitte Grosgogeat et al. "Electrochemical studies of the corrosion behaviour of titanium and the Ti–6Al–4V alloy using electrochemical impedance spectroscopy". In: *Bio-medical materials and engineering* 14.3 (2004), pp. 323–331.

[97] AC Alves et al. "Corrosion mechanisms in titanium oxide-based films produced by anodic treatment". In: *Electrochimica Acta* 234 (2017), pp. 16–27.

[98] H Fakhr Nabavi and M Aliofkhazraei. "Morphology, composition and electrochemical properties of bioactive-TiO2/HA on CP-Ti and Ti6Al4V substrates fabricated by alkali treatment of hybrid plasma electrolytic oxidation process (estimation of porosity from EIS results)". In: *Surface and Coatings Technology* 375 (2019), pp. 266–291.

[99] M Shokouhfar et al. "Preparation of ceramic coating on Ti substrate by plasma electrolytic oxidation in different electrolytes and evaluation of its corrosion resistance: Part II". In: *Applied Surface Science* 258.7 (2012), pp. 2416–2423.

[100] RS Williamson et al. "Effect of duty cycle on the crystallinity, pore size, surface roughness and corrosion resistance of the anodized surface on titanium". In: *Surface and Coatings Technology* 277 (2015), pp. 278–288.

[101] Masoud Roknian et al. "Study of the effect of ZnO nanoparticles addition to PEO coatings on pure titanium substrate: microstructural analysis, antibacterial effect and corrosion behavior of coatings in Ringer's physiological solution". In: *Journal of Alloys and Compounds* 740 (2018), pp. 330–345.

[102] Marcello La Padula. *Bipolar plasma electrolytic oxidation to enhance the localized and uniform corrosion resistance of titanium*. 2019.